Novel Substrate Integrated Waveguide Filters and Circuits

Liwen Huang

Submitted in accordance with the requirements for the degree of
Doctor of Philosophy

The University of Leeds
School of Electrical and Electronic Engineering

July 2013

The candidate confirms that the work submitted is her own and that appropriate credit has been given where reference has been made to the work of others.

The candidate confirms that the work submitted is her own, except where work which has formed part of jointly-authored publications has been included. The contribution of the candidate and the other authors to this work has been explicitly indicated below. The candidate confirms that appropriate credit has been given within the thesis where reference has been made to the work of others.

Acknowledgements

Firstly, I gratefully acknowledge the invaluable help of my supervisors Prof. Ian D Robertson and Prof. Ian Hunter throughout this research work. Without your encouragement, patience and expert advices, this thesis would not have reached its present form.

I would like to thank Prof. Naichang Yuan, Mrs Weiwei Wu and Mr Xiangan Hu for their help with the fabrication and verification of experimental filters. I would also like to express my gratitude to my colleague, Mr Lukui Jin and Miss Meng Meng, for the very helpful discussions.

A special acknowledge goes to the University of Leeds and China Scholarship Council. The financial support received is gratefully acknowledged.

Finally, I am very grateful to my parents for their support, encouragement and great confidence in me all through these years. Also I am thankful to my friends for their understanding and continuous support.

To all of you, thank you very much!

Liwen

Abstract

The main work in this thesis is to explore novel microwave filters with more compact size and improved performance by taking advantage of new substrate integrated waveguide (SIW) structures, such as the ridge substrate integrated waveguide, half mode substrate integrated waveguide (HMSIW) and SIW with complementary split ring resonators (CSRRs). This thesis therefore presents the following topics:

1. Development of a design strategy to convert from a conventional ridge waveguide configuration with solid walls to the SIW counterpart, and the design of a bandpass filter based on the ridge SIW with the proposed design method.

2. Development of a ridged HMSIW to reduce the physical size of the HMSIW by loading the HMSIW with a ridge, and application of the ridged HMSIW to the design of compact bandpass filters.

3. Development of a broadside-coupled complementary split ring resonator and a capacitively-loaded complementary single split ring resonator to reduce the size of SIW with conventional CSRRs, and application of the proposed modified structures in the design of SIW and HMSIW filters with improved compactness and performance.

4. Investigation of the application of the complementary electric-LC (CELC) resonator in SIW filters with improved stopband performance, and development of a cascaded CELC resonator to further enhance the out-of-band performance.

Table of Contents

List of Principal Symbols and Abbreviations

ω	Angular velocity
ε_0	Permittivity of free space
μ_0	Permeability of free space
f	Operation frequency
f_c	Cutoff frequency
k_0	Free space wavenumber
k_c	Cutoff wavenumber
β	Propagation constant (phase)
γ	Propagation constant
λ	Wavelength
λ_g	Guided Wavelength
dB	Decibel
GHz	Gigahertz
TE	Transverse Electric
TM	Transverse Magnetic
SIW	Substrate Integrated Waveguide
HMSIW	Half-Mode Substrate Integrated Waveguide
RHMSIW	Ridge Half-Mode Substrate Integrated Waveguide
SRR	Split Ring Resonator
CSRR	Complementary Split Ring Resonator
BC-CSRR	Broadside-Coupled Complementary Split Ring Resonator

List of Figures

List of Tables

Chapter 1
Introduction

1.1 Background

A microwave filter is typically a device that is used for frequency selectivity over the frequency range of 300MHz-300GHz by permitting good transmission of signals within the passband of the filter, while rejecting signals in the stopband of the filter [1-5]. It is widely used in wireless communication systems such as cellular radio systems, satellite systems and radar. With the recent rapid development of communication systems, especially wireless communication systems such as personal communication systems, wireless local area networks, direct broadcast satellite television and global positioning satellite systems, there has been an increasing demand for high-performance filters with a high level of miniaturization and integration. Waveguide [5] is an excellent choice for the implementation of filters with low loss, high Q factor and high power handling. However, it is relatively bulky and difficult for fabrication and integration with other electronic circuits. Planar microwave structures such as the microstrip line and coplanar microstrip line, are easy to fabricate and integrate with other electronic systems, but these planar filters are more lossy in comparison to waveguide filters, especially at a relatively high frequency [5]. Therefore, to better meet the more stringent requirements posed by modern communication systems, it is essential to develop advanced filter configurations that can be easily fabricated and integrated with other devices, while keeping low loss, excellent stopband performance, high selectivity and high power compatibility.

One of the most promising candidates to satisfy these demanding requirements is the substrate integrated waveguide (SIW) technology. The SIW is a waveguide-like structure implemented by employing arrays of metallic vias embedded in a dielectric substrate that electrically connect two parallel metal plates [6]. It combines both the merits of the conventional waveguide structure and the planar circuit such as low loss, low cost, easy fabrication and high integration. The configuration of SIW was initially introduced as a type of embedded laminated waveguide [7, 8], which could be fabricated with the common printed circuit board (PCB) fabrication method conveniently. Later, due to its favourable properties, it was

developed to be a compact, flexible, low-loss and cost effective platform to design and integrate passive components, active circuits and radiating elements in a dielectric substrate. Since the invention, various microwave and millimeter-wave components have been developed in SIW technology, such as antennas [9-11], power dividers [12-14], couplers [15, 16], filters [17-19] and diplexers [18, 20].

Microwave filters are one of the most favourable components that have been researched in the area of SIW. A variety of filters with different topologies have been developed based upon SIWs [19, 21, 22]. In [23], a direct-coupled SIW filter with irises operating at 60 GHz was designed and fabricated. In [24, 25], cross-coupled filters based on rectangular and circular SIW cavities were developed. SIW elliptic filters with high selectivity were proposed in [17] by using a two-layer substrate to realise the elliptic response with four cavities; compact and super-wideband SIW bandpass filters employing electromagnetic band-gap (EBG) structures were designed and experimentally verified in [26]. These filters are found to have lower losses than the corresponding microstrip filters, especially in the millimetre-wave frequency range. Moreover, they also exhibit a substantial size reduction in comparison to their counterparts that are implemented with conventional waveguide structures [27].

To further reduce the size of SIW filters and improve their performance, several modified waveguide configurations have been proposed, such as the ridge SIW [28, 29], half-mode SIW (HMSIW) [30] and SIW with complementary split ring resonators (CSRRs) [31, 32]. The ridge SIW was proposed based on the configuration of the ridge waveguide [33] with the vertical walls of the ridge realised with periodic metallic vias. It has a smaller physical size, a wider single mode bandwidth and a better spurious performance compared to the conventional SIW. Compact bandpass filters with the ridge SIW implemented on the low temperature cofired ceramic (LTCC) have been illustrated in [34] and [35, 36]. The HMSIW was proposed by approximating the vertical cut of the SIW as a virtual magnetic wall [30]. The HMSIW shows nearly half the size of the conventional SIW while keeping the main advantages of the SIW. In [37, 38], directional HMSIW filters have been designed and fabricated, which exhibit more compact size and wider stopband in comparison to the conventional SIW filters. Recently, some special electromagnetic structures have been applied in the SIW to enhance filter compactness and performance, namely, the split ring resonator (SRR) [39], the electric-LC (ELC) resonator [40], the

complementary split ring resonator (CSRR) [41] and the complementary electric-LC (CELC) resonator [42]. These resonators are found to be capable of producing the passband below the cutoff frequency of waveguide or stopband above the cutoff frequency due to their special band-gap properties [43-45]. Making use of these properties, several SIW filters with miniaturized size and improved performance have been developed. In [31, 32], SIW bandpass filters loaded by CSRRs operating below the cutoff frequency of the SIW were proposed; in [46], evanescent-mode SIW filters with cross-coupled CSRRs were designed and experimentally verified; in [47], by combining the high-pass band of the SIW and the stopband of the CSRR, a compact bandpass filter with wide out-of-band rejection was proposed.

While the development of these modified waveguide topologies, such as ridge SIW, HMSIW and CSRR-loaded SIW, has significantly improved the compactness and performance of filters, the physical size of these SIWs is still too large, especially for those operating at relatively low frequencies. This could lead to a certain degree of bulkiness and inflexibility in filter design, especially taking into account the growing demand for cheap, compact and mass-producible devices in modern communication systems (e.g. personal communication systems and commercial radio-frequency/millimetre-wave broadband systems). Furthermore, the performance of filters also needs to improve. Taking the SIW bandpass filter with CSRRs presented in [48] as an example, this type of filter is realised by using the stopband of the CSRR and the high-pass response of the SIW. However, due to the narrow bandwidth of the CSRR, the spurious-free bandwidth of these filters is relatively narrow, and the out-of-band rejection may be insufficient for some applications (such as cellular systems). Since miniaturized filters with high performance are critical for the development of advanced wireless communication systems with low cost, mass producible, high yield and high performance, it is therefore of great importance to continue to explore novel SIW configurations with smaller sizes and better performance, in order to reduce the dimensions of filters, improve the performance of filters, and further promote the development of modern communication systems.

The research in this thesis is therefore concerned with the investigation of the design and implementation of novel SIW filters with compact size and enhanced performance. As a starting point, a design strategy to convert from a conventional waveguide filter configuration with solid walls to the SIW

counterpart is investigated, and an evanescent-mode coupled bandpass filter based on the ridge SIW is realised with the proposed method. Inspired by the configuration of the ridge SIW, a novel ridge half-mode substrate integrated waveguide (RHMSIW) is proposed by loading the HMSIW with a ridge, and a compact wideband bandpass filter, which exhibits a smaller physical size compared to its conventional HMSIW counterpart, is designed and experimentally verified. Furthermore, SIW filters based on the CSRRs with miniaturized size and improved performance are also investigated. Two types of modified CSRR structures with improved compactness (the broadside-coupled CSRR and capacitively-loaded CSRR) are proposed to reduce the physical size of filters. A novel cascaded CELC (CCELC) resonator with enhanced out-of-band rejection is introduced to improve the stopband performance of filters. Based on these modified resonator structures, several miniaturized SIW and HMSIW filters, which exhibit a significant size reduction as well as performance improvement in comparison to those with conventional CSRRs, are designed, fabricated and tested.

1.2 Aims and Objectives

The overarching aim of this work is to investigate possible solutions for realisation of microwave filters with miniaturized size and improved performance by using the substrate integrated waveguide technology. Based on the configuration of the SIW and several modified SIWs such as the ridge SIW and half-mode SIW, novel SIW topologies with further size reduction are investigated in order to realise filters with more compact size. Moreover, since several band-gap structures such as the CSRR and the complementary electric–LC (CELC) resonator have small sizes and high quality factors, the research also focuses on the design and implementation of SIW filters with improved compactness and performance by taking advantage of these special electromagnetic structures. To achieve the overarching aim, the objectives are defined bellow:

1. Develop a design method to convert from a conventional metallic ridge waveguide configuration to the SIW counterpart and design an evanescent-mode coupled ridge SIW filter with this method.

2. Develop modified HMSIW configuration with smaller physical size and realise compact wideband filters with the modified structure.

3. Investigate the design and implementation of SIW filters with CSRRs and develop modified CSRRs to further reduce the size of filters and improve their performance.

4. Explore the application of CELC resonators in the SIW to enhance the stopband performance of filters and develop modified CELC resonators to achieve a further out-of-band improvement.

1.3 Contributions of the Thesis

Microwave filters based on the half-mode substrate integrated waveguide with reduced size in comparison to conventional SIW filters have been proposed in several papers [37, 38]. However, the physical dimensions of these filters may be still too large for some applications, especially for those working in relatively low frequencies. The work described in this thesis develops a novel ridge half-mode substrate integrated waveguide (RHMSIW) to reduce the size of the HMSIW by loading the HMSIW with a ridge. It is shown that the proposed RHMSIW has a lower cutoff frequency and a more compact size in comparison to conventional HMSIW due to the additional capacitance introduced by the ridge. Moreover, since the capacitance between the ridge and the waveguide can be enhanced by increasing the height of the ridge properly, a further size reduction can be achieved conveniently by just choosing a thick substrate for the ridge, as detailed in Chapter 4. A compact wideband bandpass filter based on the RHMSIW is designed, fabricated and tested. The measurement shows that the proposed RHMSIW filter has low loss, excellent selectivity as well as a significant size reduction compared to its HMSIW counterpart.

The combination of SIW with conventional edge-coupled complementary split ring resonators (EC-CSRR) to implement miniaturized filters operating bellow the cutoff frequency of the SIW have been investigated by several researchers [31, 32]. However, since the size reduction of these filters is mainly through the decrease of the spacing between the rings of the EC-CSRR, these filters are limited in compactness as a very small spacing in the EC-CSRR may cause inconvenience in fabrication as well as potential high losses and dielectric break [49]. In the present work, a novel broadside-coupled complementary split ring resonator (BC-CSRR) is proposed to overcome these issues by applying the duality concept to the broadside-coupled split ring resonator [50]. It is shown that, since the capacitance between the broadside-coupled rings of the BC-CSRR can be made

considerably higher than that between the edge-coupled rings (such as using a very thin dielectric substrate), the proposed BC-CSRR is capable of achieving a much smaller physical size in comparison to conventional EC-CSRRs, as detailed in Chapter 5. By adopting the BC-CSRR, novel resonators formed by the SIW with BC-CSRR pairs are proposed and investigated. Four distinct types of resonators are realised by changing the orientations of the top layer rings of BC-CSRRs, and it is found that, for one particular topology, two poles and two transmission zeros can be produced within a single unit cell, giving significant potential in realising compact filters in SIW technology. In addition, by analysing the electromagnetic field distribution of the SIW with a pair of face-to-face oriented BC-CSRRs and altering the resonator configuration properly, a modified form of BC-CSRRs with improved stopband performance is proposed. The modified BC-CSRR pairs exhibit a wider stopband as well as a deeper out-of-band rejection than conventional structures due to the suppression of the spurious passband. Making use of this structure, a miniaturized SIW bandpass filter with enhanced out-of-band performance is designed and fabricated.

The application of the complementary single split ring resonator (CSSRR) to the design of microwave filters has been illustrated in [51]. However, like the conventional EC-CSRR, the compactness of the CSSRR is limited by fabrication techniques as well as potential high losses and dielectric breakdown. In the present work, a novel capacitively-loaded CSSRR is proposed to reduce the physical size of CSSRR by adding an overlap region between the inner metal disk and the ground plane of the CSSRR. The overlap region introduces an additional capacitance. Therefore, the proposed modified CSSRR is capable of achieving a lower resonant frequency and greater miniaturization in comparison to conventional CSSRRs, as detailed in Chapter 5. A miniaturised HMSIW bandpass filter based on the capacitively-loaded CSSRR is designed, fabricated and tested. It is shown that the proposed HMSIW filter with capacitively-loaded CSSRRs exhibits good selectivity, low loss as well as a compact size.

Although bandpass filters utilizing the stopband of CSRRs and the high-pass response of SIWs to obtain a bandpass response have been developed as described in papers [48, 52], these filters are found having a relatively narrow stopband and an insufficient out-of-band rejection due to the narrow bandwidth of the CSRR. In the present work, inspired by the application of the complementary electric-LC (CELC) resonator [42] in microstrip filters to introduce two transmission zeros in the rejection band, a unit cell of SIW

integrated with the CELC resonators is proposed to enhance the stopband performance of SIW filters. It is shown that the unit cell of the SIW with CELC resonators is capable of achieving a better filtering response and an improved out-of-band performance in comparison to that with conventional CSRRs. Moreover, by combing two CELC resonators together to form a new cascaded CELC (CCELC) resonator, a further stopband improvement can be achieved, as detailed in Chapter 6. A SIW bandpass filter with the CCELC resonator is designed by using the stopband of CCELC resonators and the high-pass response of SIWs. It is shown that a broad rejection band as well as a sharp upper transition from the passband to the stopband is achieved for the proposed SIW filter with CCELC resonators.

1.4 Thesis Structure

This thesis is organized into seven chapters. Chapter 2 provides a general overview of the current studies on microwave filters and the substrate integrated waveguide technology. The theory of the design of microwave filters is introduced. The concept, electromagnetic properties and design rules of the SIW are discussed. Several modified SIW configurations, namely, the ridge SIW, half-mode SIW and CSRR-loaded SIW, are reviewed to establish the research background and significance of this study. Additionally, a brief overview of the complementary split ring resonator (CSRR) is given.

Chapter 3 investigates the design and implementation of an evanescent-mode coupled bandpass filter with the ridge SIW. The design methodology, which begins with a conventional ridge waveguide filter configuration and then converts it to the SIW counterpart, is described. A third-order ridge SIW bandpass filter is realised with the proposed method and the simulations as well as measured results are presented.

Chapter 4 develops a ridge half-mode substrate integrated waveguide (RHMSIW) filter with smaller size by integrating a ridge into the half-mode SIW. It is shown that the loaded ridge in the RHMSIW introduces additional capacitance in the waveguide and leads to a lower cutoff frequency as well as a more compact size in comparison to conventional HMSIW. By applying the proposed RHMSIW, a wideband bandpass filter, which exhibits a significant size reduction compared to its HMSIW counterpart, is designed, fabricated and tested.

Chapter 5 introduces two types of modified CSRRs to improve the compactness and performance of SIW filters: the broadside-coupled complementary split ring resonator (BC-CSRR) and the capacitively-loaded complementary single split ring resonator (CSSRR). Firstly, four distinct types of resonators are proposed making use of the BC-CSRR and the effect of the orientation of the BC-CSRR on the frequency response is investigated. Secondly, a modified form of a face-to-face oriented BC-CSRR pair with improved stopband performance is developed by altering the configuration of the BC-CSRR pair, and a SIW filter with a wide rejection band is realised using the proposed modified BC-CSRRs. Finally, a capacitively-loaded CSSRR is proposed to reduce the physical size of CSSRRs by adding an overlap region between the inner metal disk and the ground plane of the CSSRR. A miniaturized HMSIW filters with improved compactness is realised using the proposed capacitively-loaded CSSRR.

Chapter 6 illustrates the application of the complementary electric-LC (CELC) resonator to the design of SIW filters with enhanced stopband performance by using the high-pass response of the SIW and the stopband of the CELC resonator. The concept of the CELC resonator is introduced. The configuration of the SIW with CELC resonators, which exhibits a better filtering response as well as an improved out-of-band rejection in comparison to that with conventional CSRR, is proposed and investigated. By combing two CELC resonators together, a novel cascaded CELC (CCELC) resonator is proposed to further improve the stopband performance. A SIW bandpass filter is designed with the CCELC resonator by using the high-pass response of the SIW and the stopband of the CCELC resonator, and it is shown that a wide stopband as well as a sharp upper transition between the passband and stopband is achieved for the proposed filter.

Finally, the main outcomes of the work are provided along with recommendations of future work on this subject in Chapter 7.

Chapter 2
Microwave Filters and Substrate Integrated Waveguides (SIWs)

2.1 Microwave Filters for Wireless Communications

A microwave filter is typically a device that is used to control the frequency response within the frequency range of 300MHz-300GHz by permitting good transmission of signals at wanted frequencies, i.e. the pass-band, while rejecting signals at unwanted frequencies, i.e. the stop-band [1-4]. Typical frequency responses of the microwave filter include the lowpass, highpass, bandpass, and bandstop characteristics.

Microwave filters are used in a wide variety of communication systems, such as radar, personal communication systems, satellite systems and cellular radio systems. For example, Figure 2.1 shows a simplified block diagram for a payload of a satellite. A communication satellite is typically acting as a repeater which receives microwave signals, amplifies them and resends them to the ends [53]. Considering the effect of noise and non-linearities in power amplifiers, the input signal is divided into narrow band channels firstly and then recombined before outputting the signals. This division and the consequent recombination of channels are conducted by the input and output multiplexers, which are composed of many narrow bandpass filters with a typical fractional bandwidth between 0.2% and 2%. Generally, these satellite microwave bandpass filters are implemented as waveguide structures due to their low loss, high quality factors and high power handling capability. However, waveguide filters are relatively heavy and bulky,

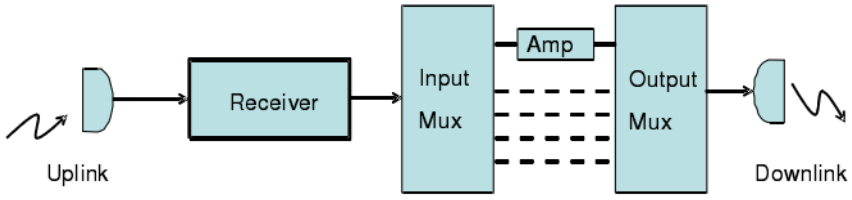

Figure 2.1 Block diagram of a communication payload of the satellite [3]

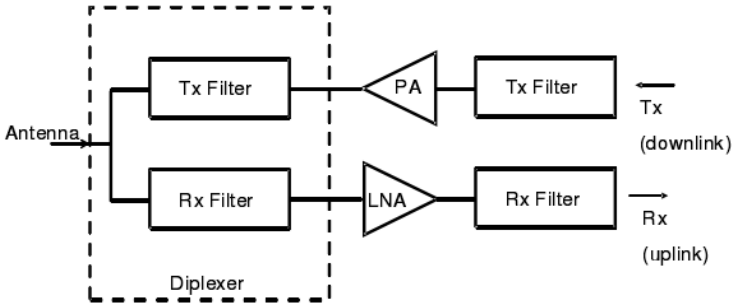

Figure 2.2 Simplified block diagram of RF front end of cellular base station [3]

which may lead to a high cost because of the launch cost package. To address this issue, several advanced filter configurations with reduced size and weight have been developed, such as dual- and triple-mode waveguide filters [54-58], dielectric resonator filters [59-62], high-temperature superconductor filters [63, 64], and a variety of coaxial, finline and microstrip filters [1-4].

Microwave filters are also extensively used in cellular radio systems, where stringent filter specifications are required both in the base station and the mobile handset. As illustrated in Figure 2.2, the cellular base station combines the functions of a microwave repeater and a switching network. Consequently, filtering requirements and constraints are quite similar to those encountered in a satellite repeater [3]. Transmit and receive filters must be quite selective, with very low insertion loss in the passband to satisfy power amplifier linearity and efficiency requirements, and very high rejection at frequencies close to the passband to prevent out-of-band inter-modulation and adjacent channel interference. A typical transmit filter has an insertion loss below 0.8 dB and return loss above 20 dB. For filters required for handsets, although the filter specifications are less stringent due to lower power handling (33 dBm maximum transmit power), the requirements of compact size and low cost means that they are still extremely challenging to realise.

The stringent requirements posed by various wireless communication systems have driven the evolution of filter design techniques. In the early stage of the development of microwave filters, most filter designs were accomplished with the *image parameter method* [5]. This method uses a cascaded two-port filter sections to provide the required cutoff frequency and attenuation characteristics, but not allowing a specified frequency response

over the complete operating range. Therefore, even though the design procedure is relatively simple, such designs require many iterations and empirical adjustments to achieve the desired results and there is no methodical way to improve the design. Later, with the development of network synthesis techniques, a new method, termed the *insertion loss method*, was developed to provide a systematic way for synthesizing the required filtering performance [5]. Filter design procedures with the insertion loss method begin with a low-pass filter prototype that is normalized in terms of impedance and frequency. The prototype is then converted to the desired filter by using the frequency and impedance transformations. Compared to the image parameter method, the insertion loss method allows the design of filters with a completely specified frequency response and it has a higher degree of control over the passband and stopband characteristics. Today, with the advances in computer-aided design (CAD) technologies, synthesis techniques coupled with accurate electromagnetic simulations as well as sophisticated optimization software algorithms have allowed the design of filters to go from drawing boards almost immediately to the final product, without the need for empirical adjustments or manual tuning. This not only cuts dramatically the time required for product development cycle, but also provides more opportunity for the implementation of more efficient communication systems.

In the meantime, significant efforts have also been devoted to the research and development of advanced microwave structures for the implementation of microwave filters. There are mainly three categories of structures commonly used in the physical realisation of filters: the lumped-element *LC* structure, the planar microwave structure, and the three-dimensional cavity structure [4]. Lumped-element *LC* structures [1] are typically composed of chip inductors and capacitors. This type of structures is generally employed in the implementation of filters operating at low frequencies, with a small size but relatively low Q-factor. Microstrip and stripline filters [2] are constructed out of sections of transmission lines terminated in a short or open circuit with various shapes, for example, hairpin [65], ring [66] and patched [67] configuration. These planar microwave filters have the advantages of compact sizes, low cost, easy fabrication and integration with other circuits, but they are relatively lossy (Q factors between 50 and 300 at 1 GHz [4]) and have limited power capability. In contrast, cavity filters such as dielectric [68], waveguide and coaxial [69, 70] filters have quite high Q-factors (up to 30000 [4]) and high power handling levels. However, they are relatively bulky and

difficult to fabricate and integrate with other circuits in comparison to their counterparts implemented with planar structures.

Recently, with the advent of a new structure termed the "*substrate integrated waveguide*" (SIW) [6], it has become possible to combine the main advantages of the waveguide cavity with that of the low cost and high integrated planar circuits. The SIW is a waveguide-like structure which can be fabricated on a planar dielectric substrate by using periodic metallic via holes as side walls. It preserves both the benefits of waveguide cavity structures and printed planar circuits such as low loss, high Q-factor, high power handling capability, compact sizes as well as easy fabrication and integration [6, 71-74]. Hence, the SIW provides a promising platform for the development of microwave filters with high performance and miniaturized size. Furthermore, it also offers a promising platform to develop cost-effective, easy-to-fabricate and high-performance communication systems by integrating filters with other electronic circuits on the same substrate, such as planar circuitry, active components and antennas.

Today, the great advances in novel materials and technologies have further driven the rapid development of filters. Several new materials and structures, such as high-temperature superconductors (HTS) [75], low-temperature cofired ceramic (LTCC) [76-78], photonic bandgap (PBG) [79, 80] and electromagnetic bandgap (EBG) structures [81-84] have been applied in the design of filters to improve the performance and reduce the size. Several advanced techniques such as monolithic microwave integrated circuits (MMIC) [85, 86] and microelectromechanical systems (MEMS) [87-89] have provided more flexibility for the physical realisation of microwave filters. In the meantime, advances in network synthesis techniques and computer-aided design tools have enabled the accurate design and simulation of some advanced filters, namely, the cascaded quadruplet (CQ) filters [90, 91], cascaded trisection (CT) filters [92, 93] and cross-coupled filters [94-97]. With the continuing advances in fabrication techniques as well as synthesis techniques and computer-aided design techniques, it is expected that the investigation of advanced filters with higher performance, lower cost and smaller size continue to be an important research topic.

2.2 Design of Microwave Filters

2.2.1 Approximation of the Transfer Function

The design of a microwave filter usually starts with the determination of a transfer function which approximates the required filter specification. An ideal filter has a zero attenuation in the passband and infinite attenuation in the stopband. Such an ideal transfer function cannot be realised in practice. However, it can be approximated with a filtering function in the domain of the equivalent circuit [1-4]. Generally, there are various functions that can be used for approximation. Here, we will focus on several classic functions, including the Butterworth (maximally flat), Chebyshev and elliptic functions.

2.2.1.1 General Definition

The transfer function for a two-port lossless passive filter network is defined as [2] :

$$\left|S_{21}(j\omega)\right|^2 = \frac{1}{1+\varepsilon^2 F_n^2(\omega)} \tag{2-1}$$

where ε represents a ripple constant; ω is a frequency variable; $F_n(\omega)$ stands for a filtering or characteristic function. For a given transfer function of (2-1), the insertion loss response of the filter can be written as follows:

$$L_A(\omega) = 10\log_{10}\frac{1}{\left|S_{21}(j\omega)\right|^2}\ dB \tag{2-2}$$

For a lossless, passive two-port network, since $\left|S_{11}\right|^2 + \left|S_{21}\right|^2 = 1$, the return loss of the filter can then be computed by:

$$L_R(\omega) = 10\log_{10}\left[1-\left|S_{21}(j\omega)\right|^2\right] dB \tag{2-3}$$

2.2.1.2 Butterworth Function Approximation

The Butterworth approximation provides the simplest approximation to an ideal prototype filter [3]. The Butterworth approximation is defined by:

$$K(\omega) = \omega^n \tag{2-4}$$

where n is the order of the prototype filter, which corresponds to the number of reactive elements required in the lowpass prototype filter. The S-parameters of the filter prototype can be expressed as:

$$\left|S_{21}(j\omega)\right|^2 = \frac{1}{1+\omega^{2n}} \tag{2-5}$$

$$\left|S_{11}(j\omega)\right|^2 = \frac{\omega^{2n}}{1+\omega^{2n}} \tag{2-6}$$

Hence, the insertion loss is given by:

$$L_A(\omega) = 10\log_{10}\left[1+\omega^{2n}\right] \tag{2-7}$$

The Butterworth approximation demonstrates maximal possible flatness of the insertion loss curve. The 3-dB cutoff frequency occurs at ω_c = 1 rad/sec and marks the transition between the passband and stopband. This transition becomes more rapid when the order of the filter is higher. Typical Butterworth prototype responses with various filter order are presented in Figure 2.3.

2.2.1.3 Chebyshev Function Approximation

The Butterworth approximation provides flat response in the passband but it rolls off quite slowly especially for low-order filters. A better approximation can be achieved if ripples exist in the passband but with more rapid roll off in the stopband. A Chebyshev approximation is defined as [3]:

$$K(\omega) = \varepsilon T_n(\omega) \tag{2-8}$$

where ε is the ripple constant that is related to the maximum in-band ripple L_{Ar} in dB by $\varepsilon = 1/\sqrt{10^{L_{Ar}/10}-1}$; $T_n(\omega)$ is a Chebyshev function of the first kind of order n, which can be expressed by $T_n(\omega)=cos(n*cos^{-1}\omega)$.

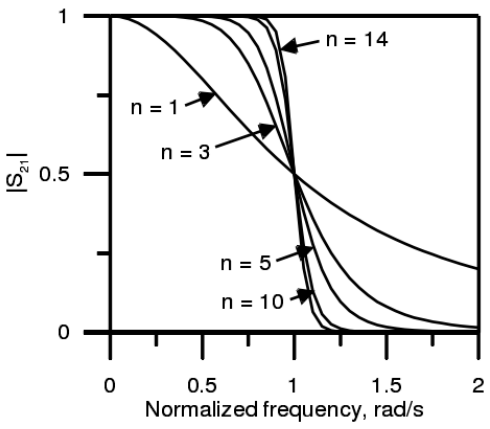

Figure 2.3 Butterworth response for various filter order, *n*

The expressions for *S*-parameters of the filter prototype are given by:

$$\left|S_{21}(\omega)\right|^2 = \frac{1}{1+\varepsilon^2 T_n^2(\omega)} \tag{2-9}$$

$$\left|S_{11}(\omega)\right|^2 = \frac{T_n^2(\omega)}{1+\varepsilon^2 T_n^2(\omega)} \tag{2-10}$$

The insertion loss can thus be expressed as:

$$L_A(\omega) = 10\log_{10}\left[1+\varepsilon^2 T_n^2(\omega)\right] \tag{2-11}$$

The Chebyshev approximation is capable of providing sharper slope for a lower filter order (*n*) compared to the Butterworth approximation, but with equal ripples introduced in the passband. A typical frequency response of the Chebyshev prototype filter is illustrated in Figure 2.4.

2.2.1.4 Elliptic Function Approximation

The Butterworth and Chebyshev approximation are referred to as all-pole approximations as all the transmission zeros are located at infinity [3]. However, placing transmission zeros at finite frequencies are quite important in some applications where a rapid roll off is required. An elliptic function approximation is equiripple in both the passband and the stopband. The elliptic function approximation is capable of producing transmission zeros at finite frequencies and thus exhibits the optimum response in terms of selectivity. Nevertheless, it should be noted that the transmission zeros of the elliptical approximation is prescribed by filter specifications, and hence these transmission zeros are restricted to be at certain frequencies and there is no flexibility in their locations.

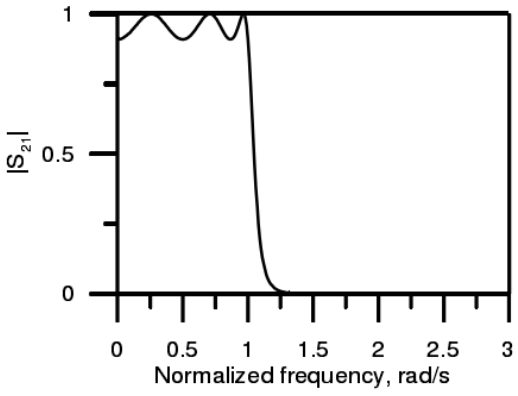

Figure 2.4 Chebyshev response

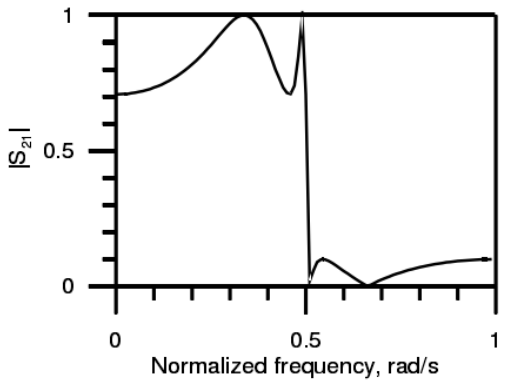

Figure 2.5 Elliptic function response

For a specific prototype with m transmission zeros ω_{z1} …ω_{zm}, and k poles ω_{p1} …ω_{pk}, the transfer function can be expressed in the following form:

$$\left|S_{21}(\omega)\right|^2 = \frac{1}{1+\dfrac{\left(\omega^2-\omega_{P1}^2\right)\cdot\ \cdot\ \cdot\left(\omega^2-\omega_{Pk}^2\right)}{\left(\omega^2-\omega_{Z1}^2\right)\cdot\ \cdot\ \cdot\left(\omega^2-\omega_{Zm}^2\right)}} \tag{2-12}$$

The attenuation is thus given by:

$$L_A(\omega) = 10\,log_{10}\left[1+\frac{\left(\omega^2-\omega_{P1}^2\right)\cdot\ \cdot\ \cdot\left(\omega^2-\omega_{Pk}^2\right)}{\left(\omega^2-\omega_{Z1}^2\right)\cdot\ \cdot\ \cdot\left(\omega^2-\omega_{Zm}^2\right)}\right] \tag{2-13}$$

A typical frequency response of the prototype filter with elliptic function is shown in Figure 2.5.

2.2.2 Lowpass Prototype Networks

The next step of the filter design is the synthesis of the equivalent circuit to reproducing the transfer function characteristics that are derived from the approximation process. This equivalent circuit should model the electrical performance of the real construction that is used for implementation of filters, and acts as an interface between the abstract filtering function and the practical filter structure, so that the physical dimensions of filters could be obtained from the element values of the prototypes. Generally, a normalized lowpass filter prototype is chosen as an equivalent network, with the values of the source resistance or conductance equal to one (denoted by g_0 = 1) and the cutoff angular frequency to be unity (denoted by Ω_c = 1 rad/s). This lowpass filter prototype can be further converted to the desired highpass, bandpass and bandstop filter prototypes by using frequency and element transformations (see the following section 2.2.3) [1, 2].

One of the most commonly used circuits for realisation of rational functions in filter design is the ladder network [1, 2]. The ladder network is composed of alternating series and parallel impedances in ladder configuration. Figure 2.6 presents two typical forms of the ladder network for realising an all-pole filter response. These two forms are dual from each other and hence either form can serve as a prototype for the design of filters with an all-pole response, such as the Butterworth and Chebyshev responses.

2.2.2.1 Butterworth Lowpass Prototype

For the Butterworth lowpass filter prototypes with an insertion loss L_{Ar} = 3 dB at the cutoff frequency Ω_c = 1, the element values for the two-port networks shown in Figure 2.6 can be computed by [2, 3]:

$$\begin{aligned} g_0 &= 1.0 \\ g_i &= 2\sin\left(\frac{(2i-1)\pi}{2n}\right), \quad i = 1,2,\cdots,n \\ g_{n+1} &= 1.0 \end{aligned} \tag{2-14}$$

As can be seen from (2-14), the Butterworth filter prototype considered here has a symmetrical network structure, namely, $g_0 = g_{n+1}$, $g_1 = g_n$ and so on.

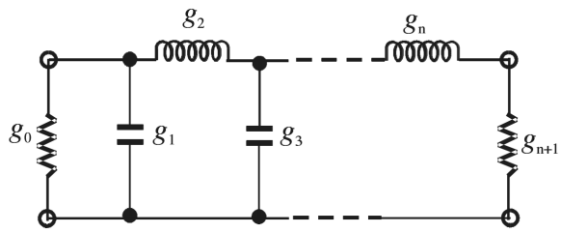

(a)

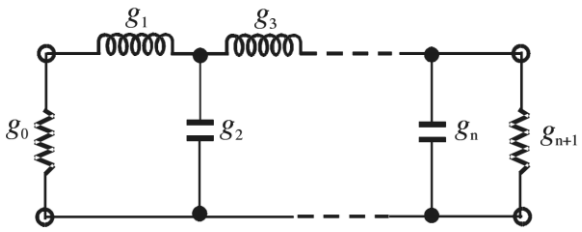

(b)

Figure 2.6 Lowpass prototype filters for all-pole filters with: (a) a ladder network structure, and (b) its dual [2]

For a given filter specification with the minimum return loss L_{Ar} at the frequency $\Omega = \Omega_p$, and the minimum insertion loss L_{AS} at $\Omega = \Omega_s$, the order of the Butterworth lowpass prototype, which will satisfy this specification, can be determined with the following formula [2, 3]:

$$n \geq max\left(\frac{log_{10}\left(10^{0.1L_{AS}} - 1\right)}{2\,log_{10}\,\Omega_s}, \frac{L_{Ar} + L_{AS}}{20\left(log_{10}\left(\Omega_s / \Omega_p\right)\right)} \right) \tag{2-15}$$

2.2.2.2 Chebyshev Lowpass Prototype

For a Chebyshev lowpass prototype filter with a passband ripple L_{Ar} and the cutoff frequency $\Omega_c = 1$, the element values shown in Figure 2.6 can be computed by [2, 3]:

$$\begin{aligned}
g_0 &= 1.0 \\
g_1 &= \frac{2}{\gamma} sin\left(\frac{\pi}{2n}\right) \\
g_i &= \frac{1}{g_{i-1}} \frac{4\,sin\left[\frac{(2i-1)\pi}{2n}\right] \cdot sin\left[\frac{(2i-3)\pi}{2n}\right]}{\gamma^2 + sin^2\left[\frac{(i-1)\pi}{n}\right]}, \qquad i = 2,\ 3,\ 4 \ldots n \\
g_{n+1} &= \begin{cases} 1.0 & for\ n\ odd \\ coth^2\left(\frac{\beta}{4}\right) & for\ n\ even \end{cases}
\end{aligned} \tag{2-16}$$

where $\beta = ln\left[coth\left(\frac{L_{Ar}}{17.37}\right)\right]$, $\gamma = sinh\left(\frac{\beta}{2n}\right)$. Some typical element values for such filters can be found in literature such as [1-3].

The degree of the Chebyshev prototype, with the required passband ripple L_{Ar} and the minimum stopband attenuation L_{AS} dB at $\Omega = \Omega_s$, is given by [2]:

$$n \geq \frac{cosh^{-1}\sqrt{\frac{10^{0.1L_{AS}} - 1}{10^{0.1L_{Ar}} - 1}}}{cosh^{-1}\,\Omega_s} \tag{2-17}$$

2.2.2.3 Elliptic Function Lowpass Prototype

The elliptic function lowpass filter prototype has finite real frequency transmission zeros and hence this prototype cannot be realised with conventional ladder networks shown in Figure 2.6. Figure 2.7 presents two

modified ladder network structures for realisation of elliptic function lowpass prototype filters, where series and parallel resonant circuits are introduced to obtain the transmission zeros. As shown in Figure 2.7(a), series branches of parallel-resonant circuits are used to implement the finite-frequency transmission zeros, as they block the transmission of signals by having infinite series impedance (open-circuit) at resonance. For the dual form illustrated in Figure 2.7(b), the shunt branches of series-resonant circuits are employed to realise transmission zeros, as they are capable of shorting out signal transmission at resonance [2]. Besides the ladder network, an alternative technique of obtaining transmission zeros at finite frequencies is using the cross-coupled network topologies [2]. More details on synthesis of the elliptic function lowpass filter prototype with the ladder network and the cross-coupled network can be found in literatures such as [2, 3].

2.2.3 Frequency and Element Transformations

The lowpass prototype filters discussed above has a cutoff frequency $\Omega_c = 1$ and a normalized source impedance $g_0 = 1$. These restrictions make them unsuitable for practical use. Therefore, it is necessary to apply the frequency and element transformations in order to obtain the frequency responses and element values for practical filters. The frequency transformation, also

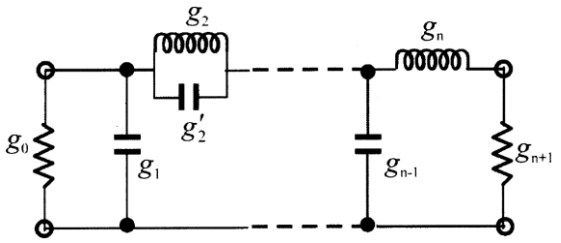

(a)

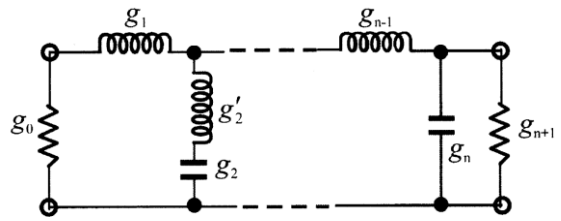

(b)

Figure 2.7 Lowpass prototype filters for elliptic function filters with: (a) series parallel-resonant branches, and (b) its dual with shunt series-resonant branches [2]

known as frequency mapping, is capable of mapping a response in the lowpass prototype frequency domain Ω into the real angular frequency domain ω, where a practical filter response is expressed (such as lowpass, highpass, bandpass and bandstop). It has an effect on all the reactive elements, but with no effect on the resistive elements. For the impedance transformation, it can remove the normalization of the source impedance in the lowpass prototypes (g_0 = 1) and adjust the filter to work for any value of the source impedance, but not affecting the frequency characteristic of filters [2].

2.2.3.1 Lowpass Transformation

To transform a lowpass filter prototype into a practical lowpass filter with a cutoff frequency ω_c in the angular frequency axis ω, the following frequency transformation can be applied [2]:

$$\Omega = \frac{\Omega_c}{\omega_c}\omega \tag{2-18}$$

The element transformation can then be found as:

$$L \to L\frac{\Omega_c}{\omega_c} \tag{2-19}$$

$$C \to C\frac{\Omega_c}{\omega_c} \tag{2-20}$$

Figure 2.8 shows the lowpass element transformation. It can be seen that the lowpass-to-lowpass transformation is a linear scaling and all the frequency dependent elements of the prototype have new values but retaining their configuration. However, it should be noted that the impedance

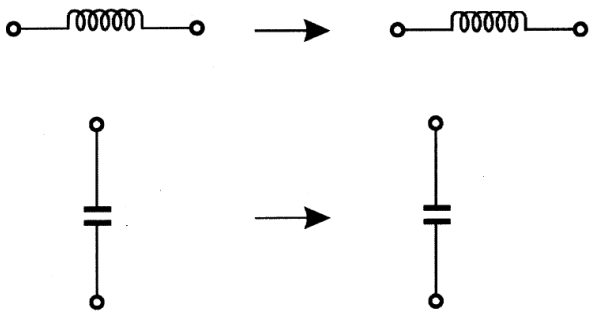

Figure 2.8 Lowpass element transformation [2]

scaling is not taken into account for this transformation, as well as other frequency mapping listed in this chapter (such as the following highpass, bandpass and bandstop transformations). The impedance scaling will be discussed in section 2.2.3.5.

2.2.3.2 Highpass Transformation

For a practical highpass filter with a cutoff frequency ω_c, the frequency transformation is given by [2]:

$$\Omega = -\frac{\Omega_c}{\omega}\omega_c \tag{2-21}$$

Applying this frequency transformation to the reactive element yields the element transformation:

$$L \rightarrow \frac{1}{\Omega_c \omega_c C} \tag{2-22}$$

$$C \rightarrow \frac{1}{\Omega_c \omega_c L} \tag{2-23}$$

This type of transformation is illustrated in Figure 2.9. It can be seen that inductive elements turn into capacitive elements and vice versa through the transformation.

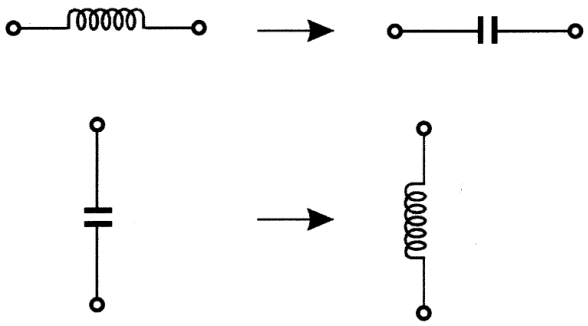

Figure 2.9 Highpass element transformation [2]

2.2.3.3 Bandpass Transformation

To convert the lowpass prototype response into a bandpass response with a passband ω_2 - ω_1, where ω_1 and ω_2 denote the passband-edge angular frequency, the required frequency transformation can be described as [2]:

$$\Omega = \frac{\Omega_c}{FBW}\left(\frac{\omega}{\omega_0} - \frac{\omega_0}{\omega}\right) \tag{2-24}$$

with

$$FBW = \frac{\omega_2 - \omega_1}{\omega_0} \tag{2-25}$$

$$\omega_0 = \sqrt{\omega_1 \omega_2} \tag{2-26}$$

where *FBW* is referred to as the fractional bandwidth; ω_0 is the centre frequency.

When this frequency transformation is applied to a reactive element of the lowpass prototype, the inductors will be converted into a series *LC* resonant tank with the values expressed as:

$$L_s = \frac{\Omega_c L}{FBW\,\omega_0} \tag{2-27}$$

$$C_s = \frac{FBW}{\omega_0 \Omega_C L} \tag{2-28}$$

Similarly, the capacitors are transformed into a parallel *LC* tank, and the parameters of the *LC* resonant circuit can be obtained from:

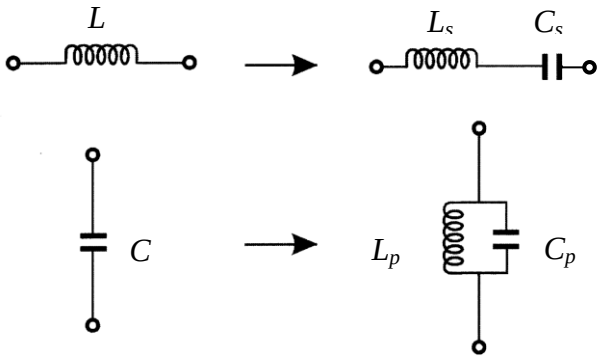

Figure 2.10 Bandpass element transformation [2]

$$C_p = \frac{\Omega_C C}{FBW\omega_0} \tag{2-29}$$

$$L_P = \frac{FBW}{\omega_0 \Omega_C C} \tag{2-30}$$

It should be noted that the resonant frequency of the resonators is coincides with the centre frequency of the filter, namely:

$$\omega_0 = \frac{1}{\sqrt{L_s C_s}} \tag{2-31}$$

$$\omega_0 = \frac{1}{\sqrt{L_p C_p}} \tag{2-32}$$

The bandpass transformation is shown in Figure 2.10.

2.2.3.4 Bandstop Transformation

The frequency transformation from the lowpass prototype to bandstop is defined as:

$$\Omega = \frac{\Omega_c FBW}{\left(\omega_0 / \omega - \omega / \omega_0\right)} \tag{2-33}$$

with

$$FBW = \frac{\omega_2 - \omega_1}{\omega_0} \tag{2-34}$$

$$\omega_0 = \sqrt{\omega_1 \omega_2} \tag{2-35}$$

Where *FBW* is the fractional bandwidth; ω_0 is the centre frequency.

This type of the transformation is opposite to the bandpass transformation. As shown in Figure 2.11, the inductive elements in the lowpass prototype will be converted into a parallel *LC* tank with the values described as follows:

$$C_p = \frac{1}{FBW\omega_0 \Omega_c L} \tag{2-36}$$

$$L_p = \frac{FBW\Omega_C L}{\omega_0} \tag{2-37}$$

For the capacitive elements, they will be transformed into a series *LC* tank with the parameters given by:

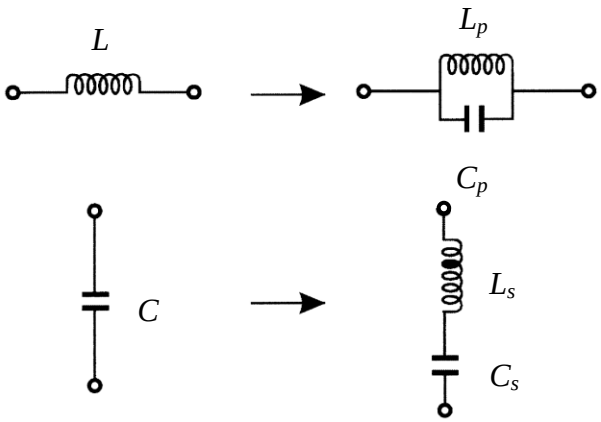

Figure 2.11 Bandstop element transformation [2]

$$L_s = \frac{1}{FBW\,\omega_0 \Omega_C C} \tag{2-38}$$

$$C_s = \frac{FBW\,\Omega_C C}{\omega_0} \tag{2-39}$$

2.2.3.5 Impedance Scaling

The impedance scaling procedure needs to be carried out after the frequency and element transformations in order to adjust the normalized source impedance of the lowpass prototype filter to any required value Z_0. The impedance scaling factor γ_0 is defined as [2]:

$$\gamma_0 = \begin{cases} Z_0 / g_0 & \text{for } g_0 \text{ being the resistance} \\ g_0 / Y_0 & \text{for } g_0 \text{ being the conductantance} \end{cases} \tag{2-40}$$

where $Y_0 = 1/Z_0$ is the source admittance. Consequently, the values of the elements of the filter prototype can be scaled with the following rules:

$$\begin{aligned} L &\rightarrow \gamma_0 L \ldots\ldots\ldots\ldots\ldots \text{for inductance} \\ C &\rightarrow C / \gamma_0 \ldots\ldots\ldots\ldots\ldots \text{for capacitance} \\ R &\rightarrow \gamma_0 R \ldots\ldots\ldots\ldots\ldots \text{for impedance} \\ G &\rightarrow G / \gamma_0 \ldots\ldots\ldots\ldots\ldots \text{for admittance} \end{aligned} \tag{2-41}$$

2.2.4 Filter Prototypes with Immittance Inverters

The ladder network structure shown in Figure 2.6 consists of series resonators alternating with shunt resonators. Such a structure is difficult to implement in a practical microwave filter. As a consequence, it is more practical to convert the prototype to an equivalent form where all of the resonators are of the same type. This can be done with the aid of the impedance inverters. Furthermore, since lumped-circuit elements are difficult to realise when the operating frequency turns higher, e.g. microwaves and millimetre waves, it is also desired to convert the lumped-circuit prototype into an equivalent distributed-circuit form in order to construct the filters more conveniently.

2.2.4.1 Impedance and Admittance Inverters

An idealized *impedance inverter*, also known as the *K*-inverter, operates like a quarter-wavelength line with a characteristic impedance *K* at all frequencies [2]. As shown in Figure 2.12(a), if the impedance inverter is terminated an impedance Z_2 on one end, the impedance Z_1 seen from the other end is [2]:

$$Z_1 = \frac{K^2}{Z_2} \tag{2-42}$$

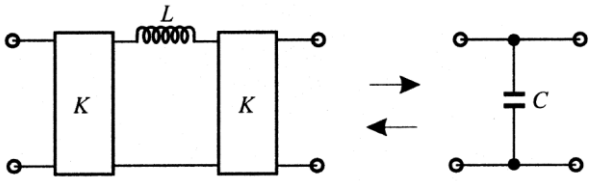

(a)

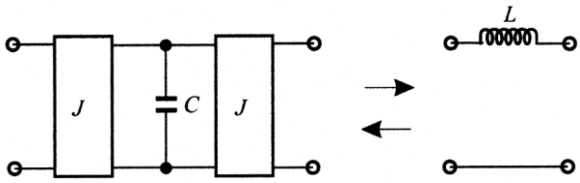

(b)

Figure 2.12 (a) Immittance inverters used to convert a shunt capacitance into an equivalent circuit with series inductance. (b) Immittance inverters used to convert a series inductance into an equivalent circuit with shunt capacitance [2]

An idealized admittance inverter, which performs as a quarter-wavelength line with a characteristic admittance *Y* at all frequencies, is the admittance representation of the same thing. As shown in Figure 2.12(b), if the admittance inverter is loaded with an admittance of Y_2 at one end, the admittance Y_1 seen from the other end is:

$$Y_1 = \frac{J^2}{Y_2} \tag{2-43}$$

It can be seen that the loaded admittance *Y* can be converted to an arbitrary admittance by choosing an appropriate *J* value. Similarly, the loaded impedance *Z* can be converted to an arbitrary impedance by choosing an appropriate *K* value.

The impedance and admittance inverters can be realised with various circuit forms. One of the simplest forms of the immittance inverter is a quarter-wavelength of transmission line [2]. As indicated by equations (2-42)-(2-43), the quarter-wavelength line can be used to implement an impedance inverter with the inverter parameter $K = Z_c$, where Z_c is the characteristic impedance of the line. Also, it can serve as an admittance inverter with the admittance inverter parameter $J = Y_c$, where $Y_c = 1/Z_c$ denotes the characteristic admittance of the transmission line. Nevertheless, it should be noted that this type of inverters is relatively narrow-band, and hence it is best used in the design of narrow-band filters.

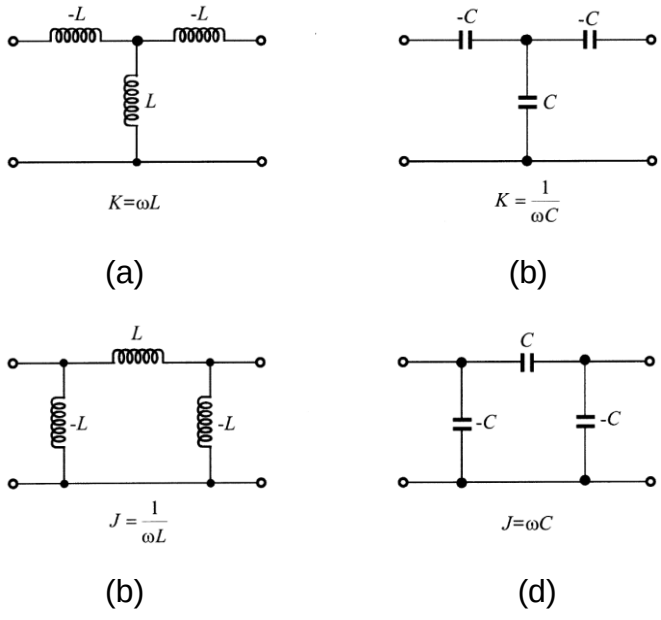

Figure 2.13 Some circuits for the realisation of immittance inverters [2]

Besides the quarter-wavelength line, there are numerous other circuits operating as inverters. Figure 2.13 presents some useful *K*- and *J*- inverters [2]. These inverters show good inverting properties over a much wider bandwidth than a quarter-wavelength line. Though some of the inductors and capacitors have negative values, there is no need to realise such components in real circuits as they will be absorbed by adjacent resonant elements in practical filters.

However, it should be noted that the *J* and *K* values of practical immittance inverters are depended on frequencies, and thus they can only approximate an ideal immittance in a certain frequency range. Considering this limitation, the immittance inverters are best used for the design of narrow-band filters. It is shown in reference [1, 2] that, using such inverters, filters with the bandwidth as great as 20 percent are achievable using half-wavelength resonators, or up to 40 percent by using quarter-wavelength resonators.

2.2.4.2 Filter Prototypes with Immittance Inverters

As described in the previous section, a shunt capacitance with an inverter on each side acts like a series inductance, and similarly, a series inductance with an inverter on each side acts like a shunt capacitance (see equations (2-42)-(2-43)). Making use of these properties enables us to convert a filter circuit to an equivalent form which could be more convenient for implementation with microwave structures. Figure 2.14 illustrates an equivalent-circuit form of the lowpass filter prototypes shown in Figure 2.6

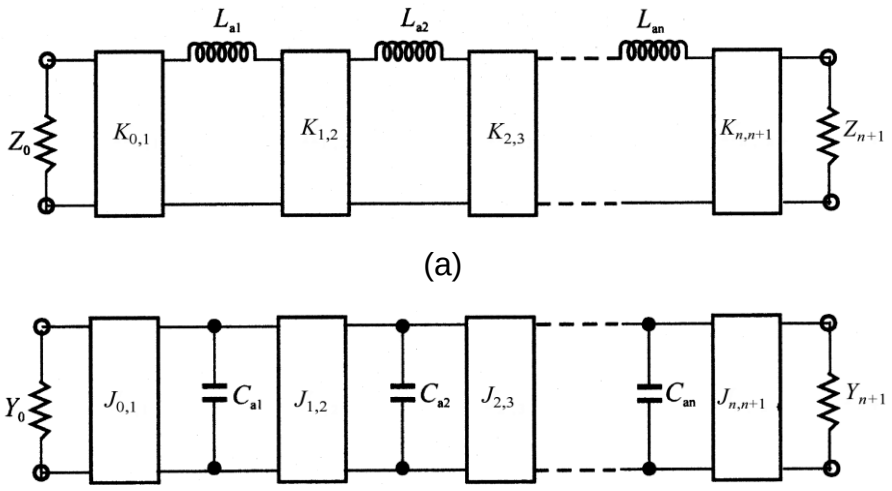

Figure 2.14 Lowpass networks using immittance inverters [2]

using the immittance inverters. It can be seen that the new equivalent circuits are composed of lumped elements of the same type that are connected by *K* or *J* inverters. The new element values, such as Z_0, Z_{n+1}, L_{ai}, Y_0, Y_{n+1} and C_{ai}, can be chosen arbitrarily, and the filter responses will be identical to that of the original prototype if the immittance inverter parameters $K_{i,i+1}$ or $J_{i,i+1}$ meet the following requirements [2]:

$$
\begin{aligned}
K_{01} &= \sqrt{\frac{Z_0 L_{a1}}{g_0 g_1}} \\
K_{j,j+1} &= \left.\sqrt{\frac{L_{ai} L_{a(a+1)}}{g_i g_{i+1}}}\right|_{i=1 \text{ to } n-1} \\
K_{n,n+1} &= \sqrt{\frac{L_{an} Z_{n+1}}{g_n g_{n+1}}}
\end{aligned}
\tag{2-44}
$$

$$
\begin{aligned}
J_{0,1} &= \sqrt{\frac{Y_0 C_{a1}}{g_0 g_1}} \\
J_{i,i+1} &= \left.\sqrt{\frac{C_{ai} C_{a(i+1)}}{g_i g_{i+1}}}\right|_{i=1 \text{ to } n-1} \\
J_{n,n+1} &= \sqrt{\frac{C_{an} Y_{n+1}}{g_n g_{n+1}}}
\end{aligned}
\tag{2-45}
$$

where g_i represents the original prototype element values defined before.

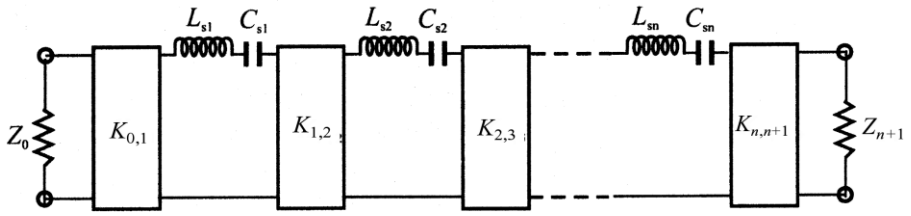

(a)

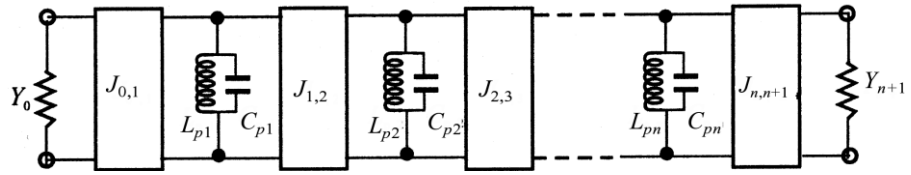

(b)

Figure 2.15 Bandpass networks using immittance inverters [2]

The lowpass prototype network shown in Figure 2.14 can be converted into other types of filters by applying the frequency and element transformations discussed in section 2.2.3. Figure 2.15 illustrates two typical bandpass filter circuits transformed from the lowpass network in Figure 2.14. It can be seen that the new bandpass network is composed of resonators that are of the same type and connected by *K*- or *J*- inverters. The parameters of the filter prototype in Figure 2.15 (a) can be calculated by:

$$
\begin{aligned}
L_{si} &= \left(\frac{1}{FBW\,\omega_0} \right) L_{ai} \Big|_{i=1 \text{ to } n} \\
C_{si} &= \left. \frac{1}{\omega_0^2 L_{si}} \right|_{i=1 \text{ to } n} \\
K_{01} &= \sqrt{\frac{Z_0 FBW\,\omega_0 L_{s1}}{\Omega_c g_0 g_1}} \\
K_{j,j+1} &= \frac{FBW\,\omega_0}{\Omega_c} \left. \sqrt{\frac{L_{si} L_{s(i+1)}}{g_i g_{i+1}}} \right|_{i=1 \text{ to } n-1} \\
K_{n,n+1} &= \sqrt{\frac{FBW\,\omega_0 L_{sn} Z_{n+1}}{\Omega_c g_n g_{n+1}}}
\end{aligned}
\tag{2-46}
$$

where L_{ai} is the value of the lumped elements shown in Figure 2.14(a).

The parameters of the filter prototype in Figure 2.15 (b) can be calculated by:

$$
\begin{aligned}
C_{pi} &= \left(\frac{\Omega_c}{FBW\,\omega_0} \right) C_{ai} \Big|_{i=1 \text{ to } n} \\
L_{pi} &= \left. \frac{1}{\omega_0^2 C_{pi}} \right|_{i=1 \text{ to } n} \\
J_{0,1} &= \sqrt{\frac{Y_0 FBW\,\omega_0 C_{p1}}{\Omega_c g_0 g_1}} \\
J_{i,i+1} &= \frac{FBW\,\omega_0}{\Omega_c} \left. \sqrt{\frac{C_{pi} C_{p(i+1)}}{g_i g_{i+1}}} \right|_{i=1 \text{ to } n-1} \\
J_{n,n+1} &= \sqrt{\frac{FBW\,\omega_0 C_{pn} Y_{n+1}}{\Omega_c g_n g_{n+1}}}
\end{aligned}
\tag{2-47}
$$

where C_{ai} is the value of the lumped elements shown in Figure 2.14(b).

The bandpass filter circuits shown in Figure 2.15 are based on the circuit in the lumped-element form. However, lumped-circuit elements are usually not easy to construct at microwave frequencies. Therefore, it is more practical to

transform the ladder network in Figure 2.15 into an equivalent form formed by distributed elements. Figure 2.16 shows two types of generalized bandpass filter circuits, where the lumped *LC* resonators in Figure 2.15 are replaced by distributed circuits. The distributed circuits can be microwave cavities, microstrip resonators or any other suitable resonant structures. Two quanitities, referred to as the reactance slope parameter and susceptance slope parameter, are introduced to establish the resonance properties of the resonators. The reactance slope parameter for resonators with zero reactance at the centre frequency ω_0 is defined by:

$$x_i = \frac{\omega_0}{2}\frac{dX_i(\omega)}{d\omega}\bigg|_{\omega=\omega_0} \tag{2-48}$$

where $X_i(\omega)$ is the reactance of the distributed resonator.

The susceptance slope parameter for resonators with zero susceptance at the centre frequency ω_0 is defined by:

$$b_i = \frac{\omega_0}{2}\frac{dB_i(\omega)}{d\omega}\bigg|_{\omega=\omega_0} \tag{2-49}$$

where $B_i(\omega)$ is the susceptance of the distributed resonator.

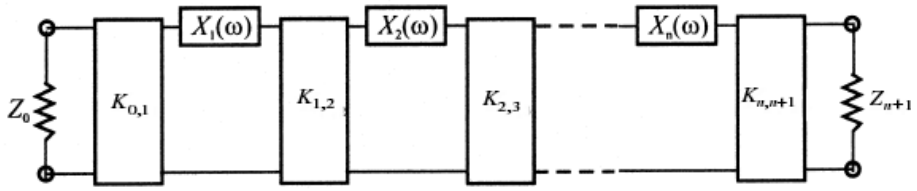

(a)

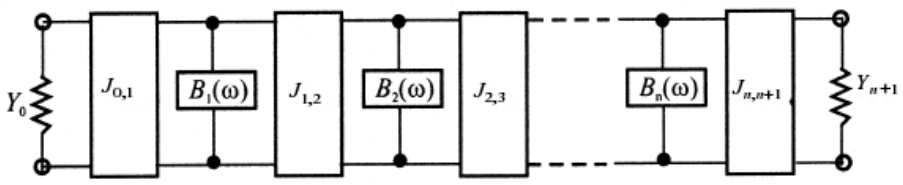

(b)

Figure 2.16 Generalized bandpass filter circuits using immittance inverters [2]

From equations (2-48)-(2-49), it can be seen that the reactance slop parameter of a series *LC* resonator is $\omega_0 L$, and the susceptance slope parameters of a parallel *LC* resonator is $\omega_0 C$. Hence, replacing $\omega_0 L_{si}$ and $\omega_0 C_{pi}$ in equations (2-46)-(2-47) with x_i and b_i, respectively, results in the following equations for the calculation of the values of the *K*- and *J*- inverters in Figure 2.16:

$$\begin{aligned} K_{01} &= \sqrt{\frac{Z_0 FBW x_1}{\Omega_c g_0 g_1}} \\ K_{j,j+1} &= \frac{FBW}{\Omega_c}\sqrt{\frac{x_i x_{i+1}}{g_i g_{i+1}}}\Bigg|_{i=1 \text{ to } n-1} \\ K_{n,n+1} &= \sqrt{\frac{FBW x_n Z_{n+1}}{\Omega_c g_n g_{n+1}}} \end{aligned} \tag{2-50}$$

$$\begin{aligned} J_{0,1} &= \sqrt{\frac{Y_0 FBW b_1}{\Omega_c g_0 g_1}} \\ J_{i,i+1} &= \frac{FBW}{\Omega_c}\sqrt{\frac{b_i b_{i+1}}{g_i g_{i+1}}}\Bigg|_{i=1 \text{ to } n-1} \\ J_{n,n+1} &= \sqrt{\frac{FBW b_n Y_{n+1}}{\Omega_c g_n g_{n+1}}} \end{aligned} \tag{2-51}$$

where $x_i = \frac{\omega_0}{2}\frac{dX_i(\omega)}{d\omega}\Big|_{\omega=\omega_0}$, $b_i = \frac{\omega_0}{2}\frac{dB_i(\omega)}{d\omega}\Big|_{\omega=\omega_0}$.

2.3 Substrate Integrated Waveguide

2.3.1 Rectangular Waveguide

A rectangular waveguide is a type of structure which directs the propagation of the electromagnetic wave by confining the wave energy. It is normally composed of a hollow or dielectric-filled conducting metal pipe with a uniform cross section (see Figure 2.17). The rectangular waveguide was one of the earliest types of transmission lines that was used to transport microwave signals and is still being used today for a lot of applications [5]. A large variety of components such as filters, couplers, detectors and isolators are commercially available for various standard waveguide bands from 1 to 220 GHz. Nevertheless, because of the trend towards miniaturization and integration, most of the microwave circuits are currently fabricated by using planar transmission lines such as microstrip lines and striplines. However,

there is still a need for waveguides in many applications, such as satellite systems, high-power systems and millimetre wave systems.

The possible configuration of the electromagnetic fields that propagates in a rectangular waveguide can be obtained by solving Maxwell's time-invariant field equations under the waveguide boundary condition [3]. It is shown that two types of modes, namely, the transverse electric (*TE*) mode and transverse magnetic (*TM*) mode, can propagate in the waveguide. The *TE* and *TM* modes can be described in the form of TE_{mn} mode and TM_{mn} mode, where *m* and *n* represent the mode numbers. These two types of modes are independent of each other and the electromagnetic field in the waveguide can be expressed as their linear superposition.

For the TE_{mn} mode, the field components can be expressed as:

$$
\begin{aligned}
E_x &= \frac{j\omega\mu}{k_c^2}\frac{n\pi}{b}H_{mn}\cos\left(\frac{m\pi}{a}x\right)\sin\left(\frac{n\pi}{b}y\right)e^{-j\beta z} \\
E_y &= \frac{-j\omega\mu}{k_c^2}\frac{m\pi}{a}H_{mn}\sin\left(\frac{m\pi}{a}x\right)\cos\left(\frac{n\pi}{b}y\right)e^{-j\beta z} \\
H_x &= \frac{j\beta}{k_c^2}\frac{m\pi}{a}H_{mn}\sin\left(\frac{m\pi}{a}x\right)\cos\left(\frac{n\pi}{b}y\right)e^{-j\beta z} \\
H_y &= \frac{j\beta}{k_c^2}\frac{n\pi}{b}H_{mn}\cos\left(\frac{m\pi}{a}x\right)\sin\left(\frac{n\pi}{b}y\right)e^{-j\beta z} \\
H_z &= H_{mn}\cos\left(\frac{m\pi}{a}x\right)\cos\left(\frac{n\pi}{b}y\right)e^{-j\beta z}
\end{aligned}
\qquad (2\text{-}52)
$$

For the TM_{mn} mode, the field distribution can be expressed by:

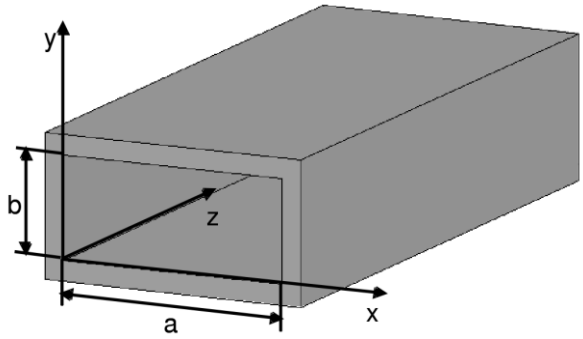

Figure 2.17 Configuration of the rectangular waveguide

$$
\begin{aligned}
E_x &= \frac{-j\beta}{k_c^2}\frac{m\pi}{a}E_{mn}\cos\left(\frac{m\pi}{a}x\right)\sin\left(\frac{n\pi}{b}y\right)e^{-j\beta z} \\
E_y &= \frac{-j\beta}{k_c^2}\frac{n\pi}{b}E_{mn}\sin\left(\frac{m\pi}{a}x\right)\cos\left(\frac{n\pi}{b}y\right)e^{-j\beta z} \\
E_z &= E_{mn}\sin\left(\frac{m\pi}{a}x\right)\sin\left(\frac{n\pi}{b}y\right)e^{-j\beta z} \\
H_x &= \frac{j\omega\varepsilon}{k_c^2}\frac{n\pi}{b}E_{mn}\sin\left(\frac{m\pi}{a}x\right)\cos\left(\frac{n\pi}{b}y\right)e^{-j\beta z} \\
H_y &= \frac{-j\omega\varepsilon}{k_c^2}\frac{m\pi}{a}E_{mn}\cos\left(\frac{m\pi}{a}x\right)\sin\left(\frac{n\pi}{b}y\right)e^{-j\beta z}
\end{aligned}
\tag{2-53}
$$

where E_{mn} and H_{mn} are arbitrary amplitude constant for the TE_{mn} mode and TM_{mn} mode, respectively; a and b are the width and height of waveguide, respectively (see Figure 2.17); k_c is the cutoff wavenumber, which can be expressed in terms of the propagation constant γ as:

$$
k_c^2 = \gamma^2 + k^2 = \left(\frac{m\pi}{a}\right)^2 + \left(\frac{n\pi}{b}\right)^2 \tag{2-54}
$$

β is the phase constant, which is purely imaginary and can be described by:

$$
\beta = -j\gamma = \sqrt{k^2 - k_c^2} = \sqrt{\omega^2\mu\varepsilon - \left(\left(\frac{m\pi}{a}\right)^2 + \left(\frac{n\pi}{b}\right)^2\right)} \tag{2-55}
$$

Though both of the *TE* and *TM* modes can propagate in the waveguide, it should be noted that, regardless of the type of the mode, only the waves at certain frequencies where the propagation constant γ ($\gamma = \alpha + j\beta$) is an imaginary number ($\gamma = j\beta$) can propagate in a lossless waveguide. If, on the contrary, γ is real ($\gamma = \alpha$), the waves decay with an attenuation factor $e^{-\alpha z}$ along the z-direction and the waveguide is characterized by exponentially decaying modes (also referred to as evanescent modes). Therefore, to guarantee that the wave can propagate within the waveguide, the condition $k_c^2 < k^2$ should be satisfied. The lowest possible excitation frequency that allows wave propagation in a waveguide is termed as the cutoff frequency, which can be obtained from (2-55) by setting the propagation constant $\beta = 0$:

$$
f_c = \frac{k_c}{2\pi\sqrt{\mu\varepsilon}} = \frac{1}{2\pi\sqrt{\mu\varepsilon}}\sqrt{\left(\frac{m\pi}{a}\right)^2 + \left(\frac{n\pi}{b}\right)^2} \tag{2-56}
$$

The propagation constant γ can be expressed in terms of the cutoff frequency f_c as follows:

$$\gamma = \begin{cases} j\beta = j2\pi f\sqrt{\mu\varepsilon}\sqrt{1-\left(\frac{f_c}{f}\right)^2} & f > f_c \\ \alpha = 2\pi f_c\sqrt{\mu\varepsilon}\sqrt{1-\left(\frac{f}{f_c}\right)^2} & f < f_c \end{cases} \tag{2-57}$$

Thus for a given operating frequency *f*, above the cutoff frequency ($f > f_c$) modes can propagate (propagation modes) while below the cutoff frequency ($f < f_c$) waves attenuate in the *z* direction (evanescent modes). If the operating frequency is exactly at the cutoff frequency ($f = f_c$), waves are neither propagate nor attenuate. In this case, a standing wave is generated along the transverse coordinates, and this is known as the transverse resonance.

For each propagating mode, the related cutoff wavelength can be described as:

$$\lambda_c = \frac{2}{\sqrt{\left(\frac{m}{a}\right)^2 + \left(\frac{n}{b}\right)^2}} \tag{2-58}$$

The related propagation constant β can be expressed in terms of the cutoff frequency f_c as:

$$\beta = 2\pi f\sqrt{\mu\varepsilon}\sqrt{1-\left(\frac{f_c}{f}\right)^2} \tag{2-59}$$

Assuming *a* > *b* in a rectangular waveguide (see Figure 2.17), the lowest cutoff wave mode, or the main mode, is the TE_{10} mode. The electromagnetic fields for the TE_{10} mode can be expressed as:

$$\begin{aligned} E_y &= \frac{-j\omega\mu a}{\pi} E_{mn} \sin\left(\frac{\pi}{a}x\right) e^{-j\beta z} \\ H_x &= \frac{j\beta a}{\pi} E_{mn} \sin\left(\frac{\pi}{a}x\right) e^{-j\beta z} \\ H_z &= E_{mn} \cos\left(\frac{\pi}{a}x\right) e^{-j\beta z} \\ E_x &= E_z = H_y = 0 \end{aligned} \tag{2-60}$$

The cutoff frequency f_c, cutoff wavelength λ_c and propagation constant β for the TE_{10} mode can be expressed by:

$$f_c = \frac{1}{2a\sqrt{\mu\varepsilon}} \tag{2-61}$$

$$\lambda_c = 2a \tag{2-62}$$

$$\beta = \sqrt{\left(2\pi f\right)^2 \mu\varepsilon - \left(\frac{\pi}{a}\right)^2} \tag{2-63}$$

From equations (2-60) to (2-63), it can be seen that the only parameter involved which affects the field and the propagation of the TE_{10} mode is the width of waveguides (*a*), while the height of waveguides (*b*) has no effect on the field configuration. This indicates that it may be possible to reduce *b* to achieve a smaller waveguide structure but with only limited effect on the TE_{10} mode propagation, i.e. substrate integrated waveguide.

2.3.2 Substrate Integrated Waveguide

The substrate integrated waveguide (SIW) is an integrated waveguide-like structure implemented on planar dielectric substrates with periodic rows of metallic vias connecting the top and bottom ground planes [6]. As shown in Figure 2.18, the top and bottom broadwalls of the SIW are covered with metal ground, and a rectangular guide is created within a substrate by caging the structure with rows of metallic vias on either side. The SIW preserves the main advantages of conventional rectangular waveguides such as low losses, high Q-factor and high power handling. It also has the advantages of planar printed circuits, such as compact size, low cost, easy fabrication and integration with other circuits.

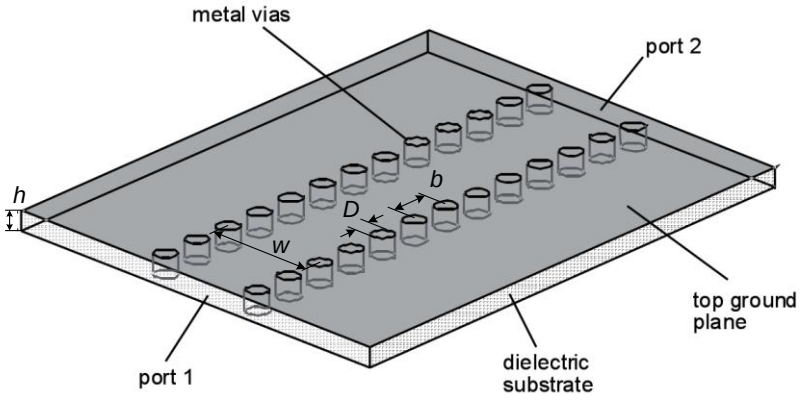

Figure 2.18 Configuration of the substrate integrated waveguide

The electromagnetic properties of the SIW have been studied in several papers [72-74]. It is shown that the guided wave properties of the SIW are similar to that of the corresponding conventional rectangular waveguide with a certain equivalent width. Therefore, the well-developed theory of waveguides can be applied to the design and analysis of SIW structures provided that the equivalent width of the SIW is given. Nonetheless, it should be noted that the differences between the SIW and the rectangular waveguide are also obvious. Since the SIW is a sort of periodic (or discrete) guided-wave structures, the propagation modes in the SIW are slightly different from those in normal waveguides, and there exists a certain type of leakage waves in SIWs due to the periodic gaps [72].

2.3.2.1 Supported Modes in the SIW

F. Xu and Ke Wu [72] have shown that the SIW exhibits similar guided wave properties to the canonical rectangular waveguide. Both of these two structures support the TE_{m0} modes, and the TE_{10} mode is the dominant mode. However, in terms of the TM and TE_{mn} (with $n \neq 0$) modes that exist in a conventional rectangular waveguide, they cannot propagate in the SIW due to the discontinuous structure of the SIW sidewalls [72]. Consequently, only TE_{m0} modes can exist in SIWs.

A clear physical explanation for the modes existing in the SIW has been given in [72] from the perspective of the surface current. As is known, when a mode is established in a guided-wave structure, the surface currents are then established. The SIW can be regarded as a special rectangular waveguide with a series of vertical slots on the sidewalls. When the slots cut along the direction of current flowing, i.e. TE_{n0} modes, only very little radiation will be yielded and thus these modes can be preserved in the waveguide. Figure 2.19 presents the flowing pattern of the TE_{10}-mode

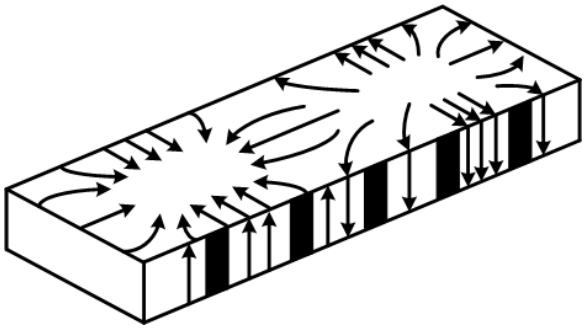

Figure 2.19 The TE_{10}-mode surface current flowing pattern of a rectangular waveguide with slots on its sidewalls [72]

surface current of a rectangular waveguide with slots on its sidewalls. It can be seen that the slots do not cut the surface current, and hence the TE_{10} mode can propagate along the waveguide. Similarly, other TE_{m0} modes can also propagate along the waveguide as they have similar surface currents on the narrow walls. However, when the surface current is longitudinal along the sidewalls of the waveguide, as is the case for *TM* and TE_{mn} (with $n \neq 0$) modes, the vertical slots will cut these currents and bring about a large amount of radiation out of the sidewalls. Consequently, the *TM* and TE_{mn} (with $n \neq 0$) modes cannot propagate along the SIW and only TE_{m0} modes can exist in the SIW.

2.3.2.2 Effective Width of the SIW

The cutoff frequency of the SIW has been investigated in [74]. It is shown that the cutoff frequencies of the TE_{10} and TE_{20} modes in the SIW with respect to the diameter of the metallized vias and the spacing between them can be expressed as follows:

$$f_{c(TE_{10})} = \frac{c_0}{2\sqrt{\varepsilon_r}}\left(w - \frac{D^2}{0.95 \cdot b}\right)^{-1} \tag{2-64}$$

$$f_{c(TE_{20})} = \frac{c_0}{\sqrt{\varepsilon_r}}\left(w - \frac{D^2}{1.1 \cdot b} - \frac{D^3}{6.6 \cdot b}\right)^{-1} \tag{2-65}$$

where c_0 is the speed of light in free space; w is the width of the SIW, D is the via diameter and b is the via spacing (see Figure 2.18). This equation is valid for $D < \lambda_0\sqrt{\varepsilon_r}/2$ and $b < 4 \cdot D$.

As has been described in section 2.3.1, the cutoff frequency of TE_{m0} modes in a conventional rectangular waveguide with the waveguide width a and height b can be described as:

$$f_c = \frac{c_0}{2\sqrt{\varepsilon_r}}\left(\frac{m}{a}\right) \tag{2-66}$$

From equations (2-64)-(2-66), it can be seen that the SIW is equivalent to the conventional rectangular waveguide. Furthermore, in terms of the fundamental propagating mode (TE_{10} mode), the SIW can be analysed as a rectangular waveguide by just using an effective width (w_{eff}) as follows [74]:

$$w_{eff} = w - \frac{D^2}{0.95 \cdot b} \tag{2-67}$$

Equation (2-67) provides a good approximation between a SIW and its equivalent rectangular waveguide. However, this approximation does not include the effect of *D/w*, which may lead to small errors when *D* increases [72]. To approach a better approximation, a more accurate empirical equation to calculate the effective SIW width was proposed in [72], which can be written as:

$$w_{eff} = w - 1.08\frac{D^2}{0.95 \cdot b} + 0.1\frac{D^2}{w} \tag{2-68}$$

This equation is very accurate when the requirements $b / D < 3$ and $D / w < 0.2$ are met.

2.3.2.3 Minimisation of the Losses of the SIW

One of the major issues in the design of SIW components is concerned with the minimisation of losses. There are mainly three mechanisms of losses in the SIW. Due to the finite conductivity of metallic walls and the loss tangent of dielectric substrate, the SIW exhibits conductor losses as well as dielectric losses like the conventional metallic waveguide. In addition, the presence of gaps along the side walls of the SIW can lead to a radiation loss due to a possible leakage through these gaps [98, 99].

The losses of the SIW can be minimized by modifying its geometrical parameters, namely, the substrate thickness *h*, the via diameter *D* and their longitudinal spacing *b* (see Figure 2.18). The thickness *h* of the dielectric substrate plays an important role in the conductor loss in the SIW. Increasing *h* can lead to a significant reduction of the conductor loss. This is due to a lower electric current density flowing on the metal surface with the increase of the thickness of substrate. The diameter of the metal vias *D* and their spacing *b* have great influence on the radiation loss. It is shown that the radiation leakage will become significant when the condition $b / D < 2.5$ is not met [72]. Generally, the following two design rules with respect to the metallic vias can be used to ensure the radiation losses kept at a negligible level [100]:

$$D < \lambda_g / 5 \tag{2-69}$$

$$b < 2 \cdot D \tag{2-70}$$

where λ_g is the guided wavelength in the SIW. In this case, the SIW can be modelled as a conventional rectangular waveguide and the mapping from the SIW to the rectangular waveguide is nearly perfect in all the single mode

bandwidth. More details about the transformation from the substrate integrated waveguide to an equivalent rectangular waveguide can be found in literature such as [72, 73] and [100].

Finally, it is important to note that the dielectric losses of SIW structures depend heavily on their operating frequencies [27, 99]. When the frequency turns higher, i.e. mm-wave frequencies, the dielectric loss is typically the most significant contribution to losses. Therefore, a proper selection of the dielectric material is extremely important to get minimum losses for the SIWs that work in a relatively high frequency, especially for those in the mm-wave frequency range.

2.3.2.4 Substrate Integrated Waveguide Transition

SIW transitions play an important role in integrating SIW components with other electronic devices. The design and implementation of transition structures between traditional rectangular waveguides and planar circuits have been widely studied [101-104]. Many of these structures can be adopted for the transition between SIW structures and planar circuits directly or with little modification, but with lower cost and more reliable fabrication process. Furthermore, since the SIW can be integrated with planar circuits on the same substrate, the whole circuit, including the planar circuit, transition and SIW structures, can be constructed in a dielectric substrate conveniently by just using a standard PCB processing technique [105].

The tapered microstrip transition [6] is one of the most commonly used structure for the transition between the microstrip line (MSL) and SIW. As illustrated in Figure 2.20, a microstrip line is connected directly to the top wall of the SIW through a tapered microstrip section; the vertical components of the electric field in both microstrip line and SIW regions are well matched and therefore the transition can be easily achieved. The tapered microstrip transition is a wideband structure that covers the complete useful bandwidth of the SIW. However, if a thicker substrate is used in SIWs in order to achieve a smaller conductor loss, the radiation loss will increase in the microstrip line as the substrate thickness is increased. Hence, the tapered microstrip transition is not suitable for active component integration, especially for those at mm-wave frequencies [106].

An alternative structure for the transition between planar circuits and SIWs is the coplanar waveguide (CPW). As shown in Figure 2.21, the CPW-SIW

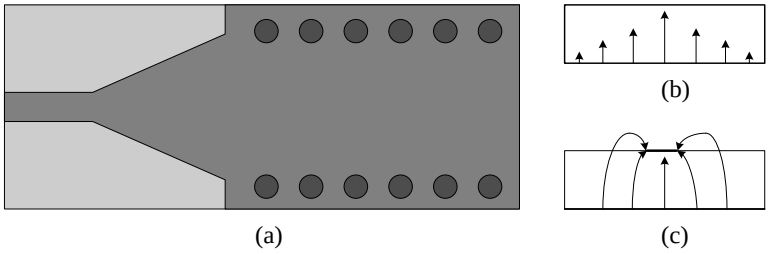

Figure 2.20 MSL to SIW transition with tapered microstrip feeding: (a) transition structure; (b) electric field distribution in SIW cross section, and (c) electric field distribution in MSL cross section

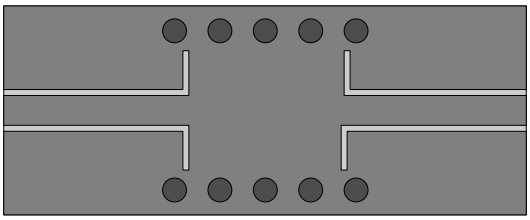

Figure 2.21 Configuration of the CPW-SIW transition

transition [107] makes use of a coplanar waveguide section to excite the SIW, with an inset stub employed to better match the CPW and SIW. Since increasing the height of the dielectric substrate might not have too much influence on the inherent characteristics of CPW, this transition is less sensitive to substrate thickness and hence exhibits a better performance than the microstrip transition in relatively high frequencies, especially in mm-wave frequencies. Nevertheless, it should be noted that the CPW-SIW transition has a narrower bandwidth in comparison to the microstrip counterpart. Several modified structures, such as the elevated CPW-SIW transition [108], have been proposed to enhance the bandwidth performance.

2.3.3 Ridge Substrate Integrated Waveguide

Conventional ridge waveguides are well known for their advantages of low cutoff frequency, compact size, wide bandwidth and concentration of fields in a smaller region in the waveguide [109]. These favourable properties are mainly achieved by the introduction of the ridge in a waveguide. As illustrated in Figure 2.22, the main effect of the inset ridge is to produce a capacitance at the ridge step. This capacitance will lower the cutoff frequency of the TE_{10} mode in the ridge waveguide and leads to a smaller physical size than conventional rectangular waveguides. Furthermore, since the capacitance occurs in a low electric field region and the loading effect is

much less for the TE_{20} mode in this case, the frequency range between the dominant mode and the first high mode is increased, and hence a wider single-mode bandwidth is achieved [110].

Based on the concept of the ridge waveguide, the ridge SIW (RSIW) was proposed in [111] to improve the bandwidth of SIWs by applying a metal ridge to the SIW. As shown in Figure 2.23(a), the RSIW is built on rows of via posts, with the central ridge realised with a row of thin metal posts. The transmission properties of the RSIW have been studied analytically and

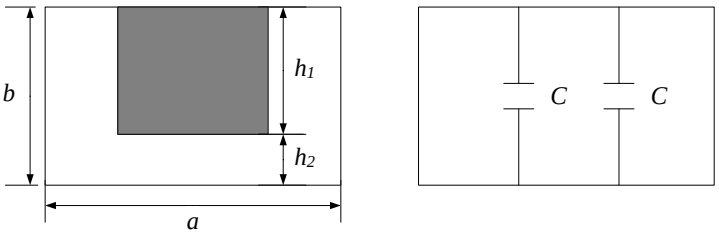

(a) (b)

Figure 2.22 (a) Configuration of the ridge waveguide. (b) Equivalent circuit

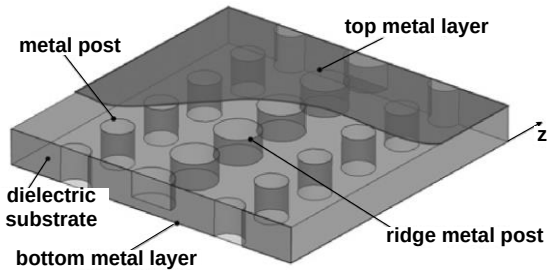

(a)

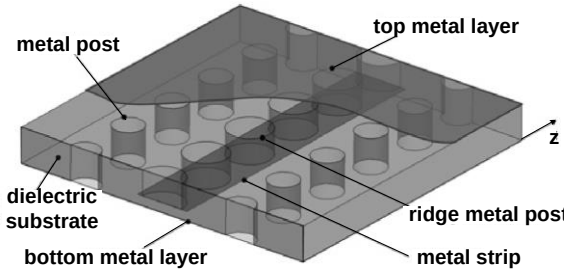

(b)

Figure 2.23 (a) Configuration of the ridged SIW. (b) Configuration of the ridge SIW with a metal strip [113]

experimentally in [112]. It is shown that, similar to the classic ridge waveguide, the insertion of the ridge introduces additional capacitance in the SIW and leads to a lower cutoff frequency as well as an enhancement of the single-mode bandwidth in comparison to conventional SIWs. Nevertheless, due to the periodic loading of the ridge posts, it is found that this structure exhibits a band gap when the ridge posts are thick and long. This phenomenon reduces the useful mono-modal bandwidth of the ridge SIW, and thus limits its utilization in the design of wideband interconnects.

A modified ridge SIW was proposed in [29, 113] to overcome this issue. As shown in Figure 2.23(b), the modified ridge SIW is similar to the conventional structure in Figure 2.23(a), with two side rows of full height metal posts to form the SIW and a central row of partial-height posts to form the ridge. Moreover, there is an additional metal strip, which connects the ridge posts at their bottom. Owing to the presence of the metal strip, the current density flowing in the axial direction does not experience the periodic loading of the ridge posts and hence the band gap phenomenon is avoided. It is shown that the modified RSIW exhibits a three times broader bandwidth than conventional SIWs. Furthermore, the size of the modified ridge SIW is only half of a SIW with the same cutoff frequency, thus giving significant potential to the design of compact wideband microwave components. In the following Chapter 3, the application of the ridge SIW in the design and implementation of microwave filters will be studied in detail.

2.3.4 Half-Mode Substrate Integrated Waveguide (HMSIW)

The configuration of the half-mode substrate integrated waveguide (HMSIW) [30] is shown in Figure 2.24. The structure of the HMSIW is similar to that of the SIW, but with the waveguide width half of conventional SIWs. The HMSIW was proposed based on the approximation of the vertical cut of the waveguide as a virtual magnetic wall [30]. As has been described in section 2.3.2, the electric field of the main mode of a conventional SIW is maximum at the vertical centre plane along the direction of propagation; therefore, this vertical plane can be viewed as an equivalent magnetic wall. Since half of the waveguide will keep the half field distribution unchanged if the cutting plane is a magnetic wall, the SIW can be bisected with this vertical centre plane to achieve a more compact size, but with the main electromagnetic properties of the SIW unchanged. In fact, the open side aperture of the HMSIW is nearly equivalent to a perfect magnetic wall due to the high ratio of the waveguide width and height [30]. Consequently, the HMSIW is capable of achieving a size reduction of nearly 50% in comparison to

conventional SIWs, while keeping the main properties of the SIW.

The propagation properties of the HMSIW have been investigated in [114]. It is shown that only $TE_{p\text{-}0..5,\ 0}$ (p = 1, 2, …) modes can propagate in the HMSIW due to the large width-to-height ratio of the HMSIW and the discrete arrangement of metallic vias. The dominant mode in the HMSIW is the $TE_{0.5,0}$ mode. The electric field distribution of the $TE_{0.5,0}$ mode in the HMSIW is shown in Figure 2.24(c). It can be seen that the electric field distribution is similar to half of the fundamental TE_{10} mode in the conventional SIW. This is also why it is termed the *half-mode* SIW.

The cutoff frequency of the main mode of the HMSIW ($TE_{0.5,0}$ mode) can be calculated by [114]:

$$f_{c(TE_{0.5,0})} = \frac{c_0}{4\sqrt{\varepsilon_r}\, w_{eff\_HMSIW}} \tag{2-71}$$

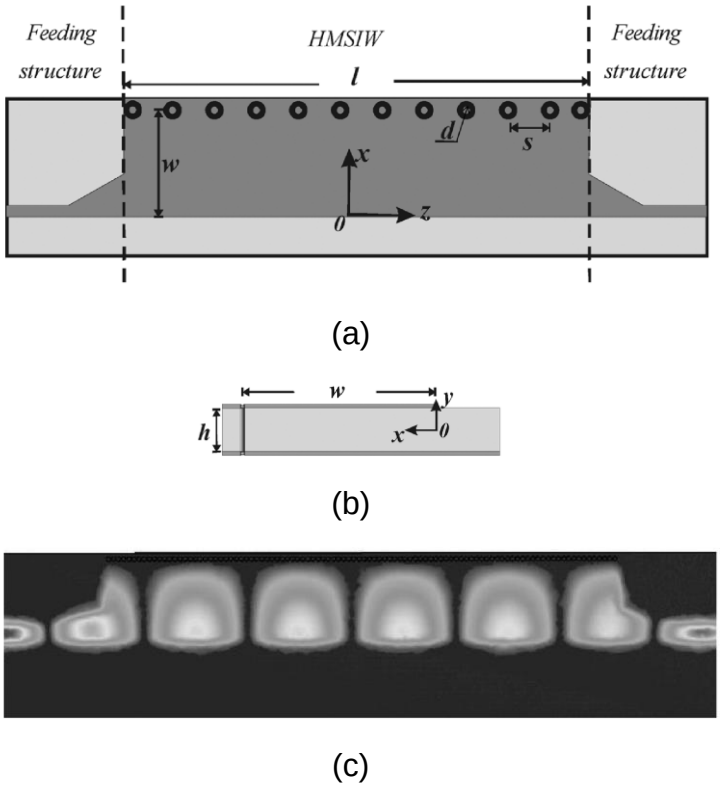

Figure 2.24 (a) Top view of the configuration of the HMSIW. Dark grey shading represents metallization. (b) Side view of the configuration of the HMSIW. (c) Electric field distribution of the $TE_{0.5,0}$ mode in the HMSIW [114]

where w_{eff_HMSIW} represents the equivalent width of the HMSIW, which can be expressed as:

$$
\begin{aligned}
&W_{eff,HMSIW} = W'_{eff,HMSIW} + \Delta W \\
&W'_{eff,HMSIW} = w - 0.54\frac{d^2}{s} + 0.05\frac{d^2}{2w} \\
&\frac{\Delta W}{h} = \left(0.05 + \frac{0.3}{\varepsilon_r}\right) \cdot ln\left(0.79\frac{W'^2_{eff,HMSIW}}{h^3} + \frac{104W'_{eff,HMSIW} - 261}{h^2} + \frac{38}{h} + 2.77\right)
\end{aligned}
\tag{2-72}
$$

where w is the width of the HMSIW, h is the height of the HMSIW, d is the via diameter, and s is the via spacing.

For the first high mode $TE_{1.5,0}$ mode, the cutoff frequency can be approximated as:

$$
f_{c(TE_{1.5,0})} = \frac{3c_0}{4\sqrt{\varepsilon_r}\, w_{eff\_HMSIW}} \tag{2-73}
$$

From equations (2-71)-(2-73), it can be seen that the cutoff frequency of the first higher mode is three times that of the fundamental mode in the HMSIW. Therefore, if not considering the suppression of the high modes, a HMSIW with a width w has a single-mode operation frequency range approximately twice that of a SIW with a width 2w [114].

As described above, the electric field distribution of the main mode of the HMSIW is similar to half of the fundamental TE_{10} mode in conventional SIWs [114]. Since the ridge SIW is capable of achieving a more compact size in comparison to conventional SIWs by loading the SIW with a ridge (see section 2.3.3), it may be possible to load the HMSIW with a ridge like the ridge SIW to achieve a further size reduction, while keeping the main advantages of the HMSIW. This solution to reduce the size of HMSIWs will further be studied in detail in Chapter 4.

2.3.5 SIW with the Complementary Split Ring Resonator (CSRR)

The configuration of the edge-coupled split ring resonator (EC-SRR) was initially proposed by Pendry *et al.* in [39]. As shown in Figure 2.25(a), the EC-SRR is formed by two concentric conducting rings printed on a dielectric substrate. These two split rings are coupled by means of a strong distributed capacitance between the rings. If a time varying magnetic field is applied parallel to the rings axis, current loops will be induced in the rings and these current lines will pass from one ring to the other through the distributed capacitance between the rings. Therefore, the EC-SRR behaves as a parallel *LC* resonant tank that can be excited by external magnetic fields, and its resonant frequency f_{rs} can be expressed as [115]:

$$f_{rs} = \frac{1}{2\pi\sqrt{L_s C_s}} \tag{2-74}$$

where L_s and C_s are the total inductance and capacitance of the EC-SRR, respectively.

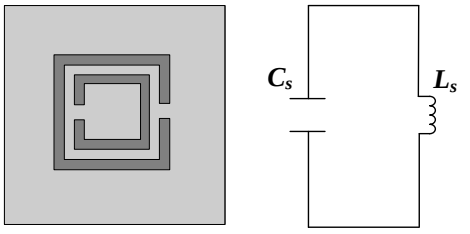

(a)

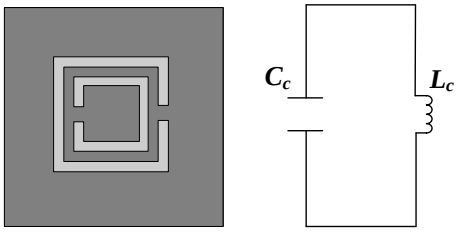

(b)

Figure 2.25 (a) Configuration of the EC-SRR and the equivalent circuit. (b) Configuration of the EC-CSRR and the equivalent circuit. Dark Grey represents metallization

A detailed procedure to calculate the value of L_s and C_s has been given in literature [49, 115]. It is shown that the inductance and capacitance of the EC-SRR are mainly governed by the ring width (c) and the spacing between the rings (d), respectively. The decrease of c / d can result in a larger L_s / C_s and further lead to a lower resonant frequency and a more compact size. However, it should be noted that very intense electric fields could appear at the ring edges for the EC-SRR with very small spacing, which may cause high losses and/or dielectric breakdown. Hence, these effects should be taken into account when the EC-SRR is used to implement microwave components with very small physical size.

From a duality argument, the edge-coupled complementary split ring resonator (EC-CSRR) was proposed by Falcone *et al.* in [41]. As shown in Figure 2.25(b), the EC-CSRR is the negative counterpart of the EC-SRR. It can be modelled as a resonant LC tank driven by external electric fields. The resonant frequency of the EC-CSRR (f_{cr}) is given by [115]:

$$f_{rc} = \frac{1}{2\pi\sqrt{L_c C_c}} \tag{2-75}$$

where L_c and C_c are the total inductance and capacitance of the EC-CSRR, respectively. For relatively thick substrate, f_{rc} can be approximated with the resonant frequency of the corresponding EC-SRR (see (2-74)) from the duality concept [41]. However, more accurate calculation of the value of f_{rc} as well as the related L_c and C_c can be found in the literature [115].

The combination of SRRs/CSRRs and a rectangular waveguide has been investigated in several papers such as [43-45]. It is shown that the SRRs and CSRRs are capable of generating a passband below the cutoff frequency of the waveguide or a sotpband above the cutoff frequency. This property can be interpreted as a result of the negative permeability/permittivity introduced by SRRs/CSRRs in the waveguide [43, 44]. However, from another perspective, it is demonstrated that the passband below the cutoff frequency is caused by the properties of the periodical array of resonator dipoles, and for other electric scatterers that are realised with inductively loaded short wires or strips, they can also be suitable for implementation of miniaturized waveguide in a similar way to the SRRs and CSRRs [116, 117].

Several miniaturized waveguide filters have been developed making use of the special properties of SRRs and CSRRs [31]. Particularly, since the

CSRR can be integrated into the SIW conveniently by just etching CSRRs on the top/bottom broadwalls of the SIW, a great deal of attention has been paid on its application to the design of miniaturized SIW filters. For example, in [31], novel compact SIW bandpass filters loaded by CSRRs were proposed by using the passband below the cutoff frequency of the SIW. In [48, 52], wide-band SIW bandpass filters were proposed by combining the stopband of periodical CSSRs with the high-pass band of the SIW. However, it should be noted that most of these filters were implemented with conventional EC-CSRRs. Since the size reduction of the EC-CSRR is similar to that of the EC-SRR, which is mainly through the decrease of the spacing between the rings of the EC-CSRR, the compactness of these filters is limited by fabrication techniques as well as potential high losses and dielectric break [49]. Furthermore, for the bandpass filters that are realised by combing the high-pass band of SIWs and stopband of EC-CSRRs (such as the filter presented in [48]), since the bandwidth of conventional EC-CSRRs is relatively narrow, this type of filters has a relatively narrow stopband and the out-of-band rejection may be insufficient for some applications. Hence, novel structures are needed to improve the compactness and stopband performance of these filters.

Recently, two new types of resonators that exhibit improved compactness and out-of-band performance in comparison to conventional EC-SRRs and EC-CSRRs have been proposed: the broadside-coupled split ring resonator (BC-SRR) [50] and the complementary electric-LC (CELC) resonator [118]. The configuration of the BC-SRR is shown in Figure 2.26(a). It can be seen that the BC-SRR can be derived from the EC-SRR (see Figure 2.25(a)) by replacing one of the rings by another ring located just at the opposite side of the dielectric substrate, with the slits still placed at opposite sides. The electromagnetic properties of the BC-SRR are similar to that of the EC-SRR. It can be modelled as a resonant *LC* circuit driven by proper magnetic field. However, compared to conventional EC-SRRs, the BC-SRR has a more compact size due to a higher capacitance that can be obtained for the broadside-coupled metallic strips [50]. Making use of this property, it may be possible to develop a new broadside-coupled complementary split ring resonator (BC-CSRR) with smaller size than conventional EC-CSRRs by using the duality concept, and apply the new BC-CSRR resonator for the realisation of miniature SIW filters.

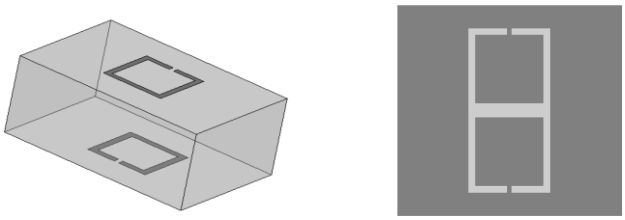

(a) (b)

Figure 2.26 (a) Configuration of the BC-SRR. (b) Configuration of the CELC resonator

The configuration of the CELC resonator is shown in Figure 2.26(b). The CELC resonator is composed of two identical back-to-back complementary single split rings and it can be modelled as a resonant LC tank driven by the in-plane magnetic fields normal to the split. When etched on the ground plane of microstrip lines, it is found that the CELC resonator is capable of generating a broad stopband with two transmission zeros due to its magnetic and electric resonances [42]. Taking advantage of this property, it may be possible to adopt the CELC resonator in SIW filters to achieve improved out-of-band performance. More detailed studies on the application of the BC-SRR and the CELC resonator in SIW filters will be presented in Chapters 5&6.

2.4 Summary

In this chapter, an overview of microwave filters and substrate integrated waveguide has been presented.

Sections 2.1 & 2.2 present an outline of microwave filters and the filter design method, including the approximation of transfer functions, synthesis of the lowpass filter prototypes and frequency and impedance transformations. Filter prototypes with immittance inverters are also discussed.

In section 2.3, an overview of the substrate integrated waveguide has been presented. The basic concepts and design rules of the SIW have been discussed, including the propagating wave, the equivalent waveguide width, and the miniaturized losses of SIWs. The SIW transition has been briefly considered. Several modified SIW configurations such as the ridge SIW, half-mode SIW and SIW with complementary split ring resonators have been presented.

Chapter 3
Ridge Substrate Integrated Waveguide Filters

3.1 Introduction

As described in Chapter 2, the ridged SIW is an integrated waveguide structure which is based on the configuration of the conventional ridged waveguide [33, 109] by using rows of periodic metallised via holes to approximate the vertical solid walls of the waveguide and the ridge [28, 113]. The ridged SIW has a lower cutoff frequency and wider single mode bandwidth in comparison to the conventional SIW. Therefore, it has great potential in the design of filters with compact sizes and wide rejection band. Several compact filters based on the ridged SIW implemented in LTCC technology, where the ridge is realised by printing top and bottom broadwalls, and rows of metal-filled vias for the sidewalls, have been proposed in [35]. However, it should be noted that the ridged SIW filters might be also possible to be realised in multilayer PCB technology, which could lead to the integration of ridge waveguide filters into normal PCB subassemblies and further avoid the time consuming and comparatively high cost manufacturing technique of LTCC.

In this chapter, attention will be paid to the design and implementation of a ridged SIW bandpass filter based on the multilayer PCB technology. An efficient design approach of the ridged SIW bandpass filter is proposed. Initially, the bandpass filter is designed as a conventional ridged waveguide filter configuration with ideal solid walls so that the dimensions of the ridge can be roughly determined to meet a specific frequency response. Then, by using the metallised via-fence wall to emulate the solid walls, the previous filter configuration is transformed to a ridged SIW bandpass filter which can be realised with multilayer PCB technology. A prototype of the ridged SIW bandpass filter was designed according to this proposed design approach and fabricated using the multilayer PCB. The experimental measurement agrees well with the simulation on the frequency response. It is demonstrated that the ridged SIW bandpass filter can be implemented using the multilayer PCB technology with easy fabrication and low cost, while keeping the advantages of compact size and high integration.

3.2 Design of the Ridged SIW Filter

3.2.1 Design of the Ridged SIW Resonator

The configuration of a ridged SIW resonator is shown in Figure 3.1. Two-rows of metallised vias (the bolder vias shown in Figure 3.1) are used to form the sidewalls of the SIW cavity. The ridge is also realised by periodic metallic via holes (the smaller via holes in the central region shown in Figure 3.1) where an additional metallic plane is used to connect the via holes on the bottom. However, these vias of the ridge do not go through the entire dielectric substrate – which is why multilayer technology is required. Inevitably, the multilayer ridged SIW can only be realised with a small number of different ridge height values, and this has to be taken into account in the design and optimization of the structure. A microstrip feed line is used at the input and output of the cavity. As ridged waveguides are often used for waveguide to microstrip transitions, this guarantees that the ridged SIW cavity is properly excited.

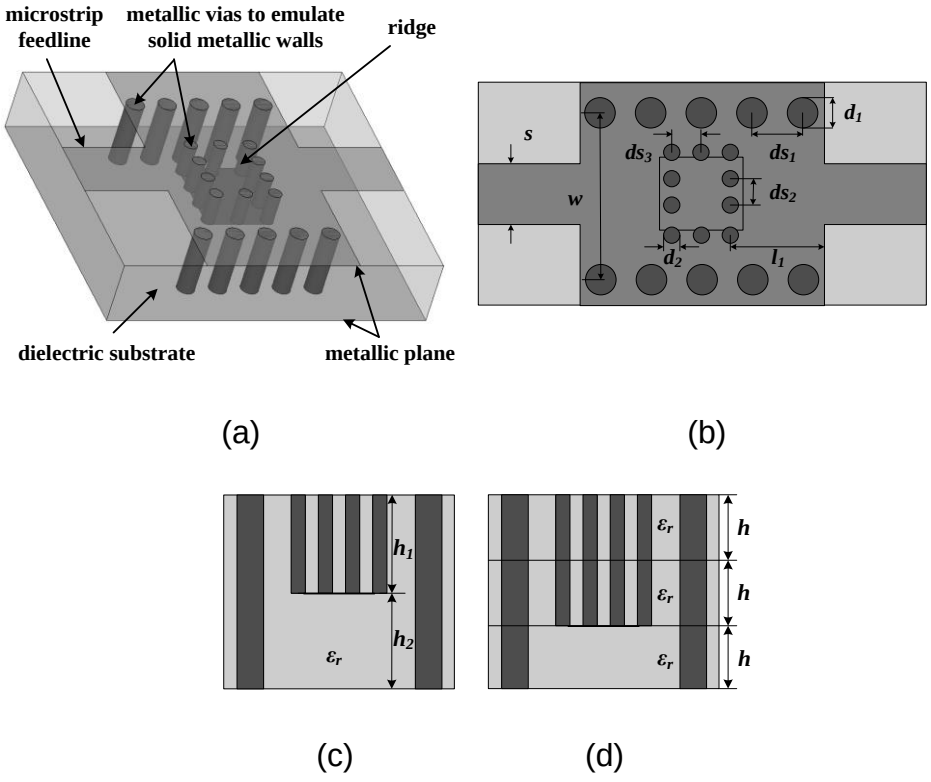

Figure 3.1 Configuration of the ridged SIW resonator: (a) 3-D view; (b) top view; (c) side view for a resonator in a 2-layer board with different substrate height, and (d) side view for a 3-layer board with equal substrate heights

To aid the design of the ridged SIW resonator with specific frequency responses, an initial ridged waveguide resonator configuration with ideal solid metal walls and filled with the same homogeneous dielectric substrate as the ridged SIW resonator was first designed (see Figure 3.2). The design of this configuration can be conveniently conducted in reference to the classic ridged waveguide theory [33]. This ridged waveguide resonator configuration could then be converted to the ridged SIW resonator by using periodic metallised vias to emulate the vertical solid walls (i.e. from Figure 3.2(a) to Figure 3.1(a)). However, it should be noted that the width of the ridged SIW resonator (w) is slightly different from that of the initial ridged waveguide resonator (w_1) due to the introduction of the via-fence wall. The width of the ridged SIW resonator could be approximated with that of the ridged waveguide configuration with ideal solid walls by using the following equation [119]:

$$w = w_1 + \frac{d_1^{\,2}}{0.95 \cdot ds_1} \tag{3-1}$$

where w and w_1 denote the width of the ridged SIW and the ridged waveguide respectively; d_1 and ds_1 represent the via diameter and the via

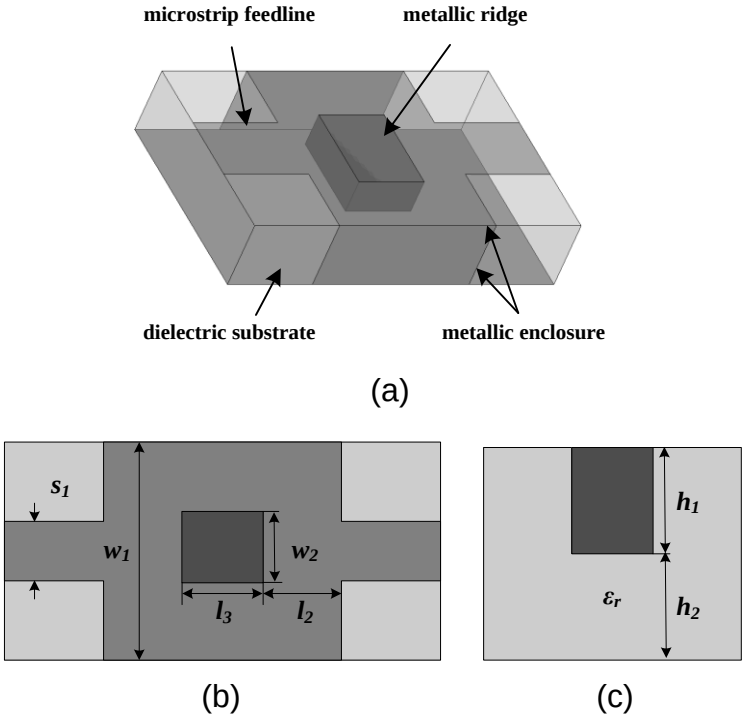

Figure 3.2 Configuration of the ridged waveguide resonator: (a) 3-D view; (b) top view; (c) side view

pitch, respectively (see Figure 3.1(b) and Figure 3.2(b)). Similar to the row of metallised via holes forming the SIW side-walls, the side walls of the SIW ridge are also realised with a row of metallised via holes. To achieve a better approximation to the ideal vertical walls of the ridged waveguide configuration, the distance between two adjacent via centres, i.e. the via hole pitch, is chosen to be [120]:

$$ds_1 \leq 2 \cdot d_1 \tag{3-2}$$

$$ds_2 \leq 2 \cdot d_2 \tag{3-3}$$

$$ds_3 \leq 2 \cdot d_2 \tag{3-4}$$

where d_1 and d_2 denote the diameters of the vias forming the SIW wall and the SIW ridge, respectively; ds_1 represents the via hole pitch of the SIW wall; and ds_2 and ds_3 represent the via hole pitch of the SIW ridge (see Figure 3.1(b)).

By using the ridged waveguide resonator configuration and the design principles described in (3-1)-(3-4), the initial dimensions of the ridged SIW resonator can be obtained. However, since the sidewalls of the SIW ridge are implemented by using a via fence to approximate the vertical solid wall, the effect of this via-fence wall should be taken into consideration and some tuning and optimization need to be carried out in order to get a better equivalent of the required ideal resonator configuration. Figure 3.3(a)-(c) present the HFSS™ simulated results of a single resonator with different via diameters (d_2) and via hole pitches (ds_2, ds_3) of the SIW ridge, respectively. It can be seen that the resonant frequency shifts higher with the increase of d_2 and ds_2 (see Figure 3.4(a)-(b)), and shifts lower with the increase of ds_3 (see Figure 3.4(c)). This change of the resonant frequency is because the change of d_2, ds_2 and ds_3 results in a different equivalent size of the ridge. Moreover, Fig. 4(d) presents the response of the resonator for different values of the height of the ridge h_1. It can be seen that the resonant frequency is significantly reduced when h_1 increases, and higher selectivity is also observed. This is due to the increase of the loading capacitance with the increased height of the ridge, h_1 [121]. This indicates that a more compact size and better performance could be achieved by choosing a large h_1 or the ratio h_1/h_2.

By looking at these simulations with swept parameters, optimal dimensions of the ridged SIW resonator can be determined. Figure 3.4 displays the transmission response of one such design. A ridged waveguide resonator was initially designed to achieve a resonant frequency at 9.26 GHz, with the parameters as follows: $\varepsilon_r = 2.65$, $h_1 = h_2 = 1$ mm, $s_1 = 3$ mm, $w_1 = 9$ mm, $w_2 = 5.3$ mm, $l_2 = 4$ mm, $l_3 = 4.45$ mm. By the design approach discussed above, an equivalent ridged SIW resonator was designed with the parameters as follows: $\varepsilon_r = 2.65$, $h_1 = h_2 = 1$ mm, $s = 3$ mm, $w = 10.05$ mm, $l_1 = 4.75$ mm, $d_1 = 1.6$ mm, $d_2 = 1.2$ mm, $ds_1 = 2.9$ mm, $ds_2 = ds_3 = 2$ mm. From Figure 3.4, it can be seen that excellent agreement is achieved between the frequency response of the ridged SIW resonator and that of the ridged waveguide resonator configuration.

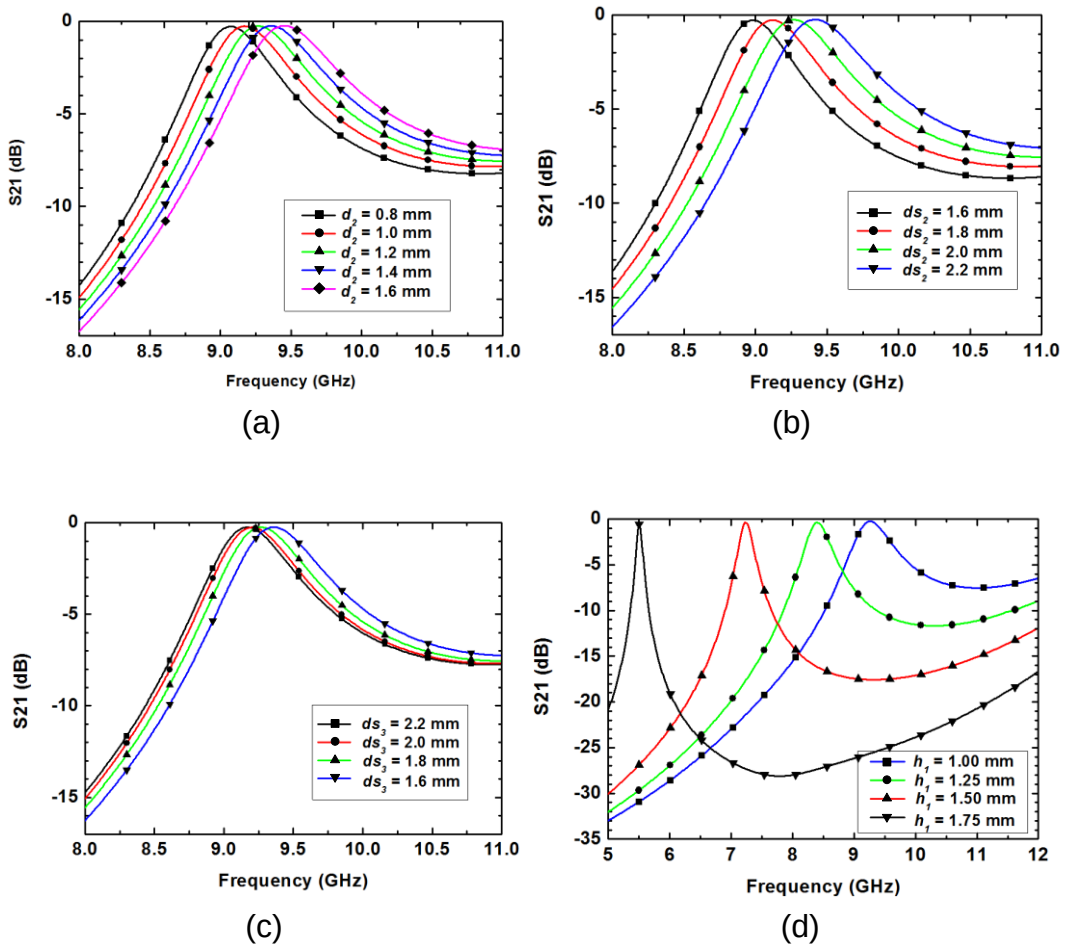

Figure 3.3 Simulated frequency responses of the ridged SIW resonator with: (a) different via diameter d_2 (with $h_1 = 1$ mm); (b) different via hole pitch ds_2 (with $h_1 = 1$ mm); (c) different via hole pitch ds_3 (with $h_1 = 1$ mm); (d) different height of the ridge h_1 (with parameters $\varepsilon_r = 2.65$, $h_1 = h_2 = 1$ mm, $s = 3$ mm, $w = 10.05$ mm, $l_1 = 4.75$ mm, $d_1 = 1.6$ mm, $d_2 = 1.2$ mm, $ds_1 = 2.9$ mm, $ds_2 = 2$ mm, $ds_3 = 2.2$ mm)

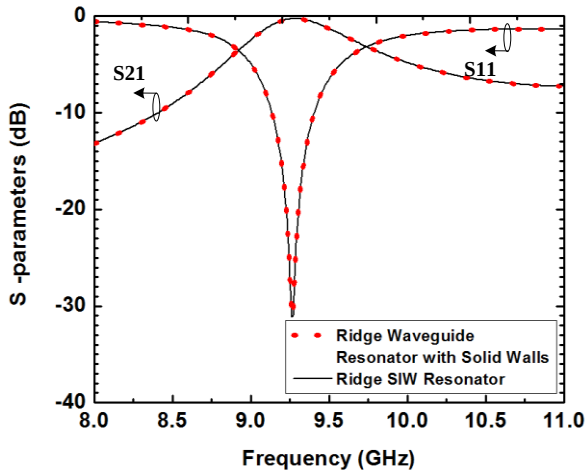

Figure 3.4 Simulated frequency responses of the ridged SIW resonator and the ridged waveguide resonator configuration

To physically realise the ridged SIW resonator, it is feasible to use multilayer PCB technology. For example, in Figure 3.1(c), the ridged SIW resonator can be conveniently constructed out of two-layer dielectric substrate, with the thickness of top substrate h_1 equal to that of ridges, and the thickness of bottom layer h_2 representing the gap between the ridge and bottom ground plane. By properly choosing the thickness of top substrate, h_1, and bottom substrate, h_2, better performance and more compact size can be achieved as discussed before. On the other hand, it is also feasible to build the resonator by using a multilayer substrate with each layer having the same thickness. In this case, the vertical walls of the ridge can be realised with metallised via holes through several layers of the substrate. As shown in Figure 3.1(d), for example, the ridged SIW resonator can be realised in a three-layer dielectric substrate with the thickness of each layer being h; the vertical walls of the ridge are then formed from the metallised vias through the first and second layer, with the third layer forming the gap between the ridge and the bottom ground plane. In terms of this method of physical realization, although the height of the ridge is restricted to a limited set of discrete values, multilayer boards often have 18 or more layers, allowing sufficient design freedom.

From these discussions, it can be seen that there is great flexibility in the design and physical realis ation of the ridged SIW resonator. The design methodology starts with a conventional ridged waveguide resonator configuration with ideal solid walls and then converts it to the ridged SIW counterpart. The implementation of the ridged SIW resonator is convenient

and flexible, which can lead to the easy integration of ridged SIW components with other circuits.

3.2.2 Design of the Ridged SIW Bandpass Filter

A bandpass filter with a bandwidth 0.6 GHz at a center frequency 9.24 GHz was designed based on the ridged SIW resonator. The ridged SIW bandpass filter consists of ridged SIW resonators coupled by evanescent-mode SIW sections. Based on the design strategy mentioned above, an initial ridged waveguide bandpass filter configuration with dielectric constant = 2.65 and the height of each layer 1 mm (h_1 = h_2 = 1 mm), was first designed. As shown in Figure 3.5(a) and Figure 3.5(b), the ridged waveguide bandpass filter configuration employs ridged waveguide resonators with ideal vertical walls which are coupled by sections of the evanescent-mode waveguide. An inset microstrip transition was employed to get a better match between the cavity and the microstrip feed line.

A third order (n = 3) Chebyshev lowpass prototype with a passband ripple of 0.1 dB is chosen for the design of the ridge waveguide filter. The lowpass prototype parameters, given for a normalized lowpass cutoff frequency Ω_c = 1, are g_0 = g_4 = 1, g_1 = g_3 = 1.035, g_2 = 1.147. Having obtained the lowpass parameters, the bandpass design parameters can be calculated by [1]:

$$\begin{aligned} Q_{e1} &= \frac{g_0 g_1}{FBW} \qquad & Q_{e1} &= \frac{g_n g_{n+1}}{FBW} \\ k_{i,i+1} &= FBW / \sqrt{g_i g_{i+1}} \qquad & for\ i &= 1\ to\ n-1 \end{aligned} \tag{3-5}$$

where FBW is the fractional bandwidth, Q_{e1} and Q_{en} are the external quality factors of the resonators at the input and output, and $k_{i,i+1}$ are the coupling coefficients between the adjacent resonators.

For this design example, we have: Q_{e1} = Q_{e3} = 15.4; $K_{1,2}$ = $k_{2,3}$ = 0.1097. Using a parameter-extraction technique described in [2], the relationship between the external factor Q, coupling coefficient k and the physical dimensions can be obtained. The external Q factor can be extracted by using a doubly-loaded resonator and calculated by:

$$Q_e = \frac{2 f_0}{\Delta f_{3dB}} \tag{3-6}$$

where f_0 is the frequency where S_{21} is maximum; Δf_{3dB} denotes the 3-dB bandwidth for which S_{21} is reduced by 3 dB from the maximum value.

The coupling coefficients can be obtained using [2]:

$$k = \frac{f_1^2 - f_2^2}{f_1^2 + f_2^2} \tag{3-7}$$

where f_1 and f_2 represent the resonance frequencies of low and high modes, respectively. Figure 3.5(e) shows the value of coupling coefficient k against the evanescent-mode waveguide coupling length (denoted by l) between two adjacent ridge waveguide resonators. It can be seen that the coupling between resonators increases with the decrease of the evanescent-mode waveguide length.

After getting the initial dimensions of the ridge waveguide filter, the parameters of the filter can be tuned to get a better result. The centre frequency of the filter can be adjusted by tuning the length of the ridge l'_5 and l'_7 (see Figure 3.5(a)). The bandwidth of the filter can be tuned by changing the length of the evanescent-mode SIW sections l'_4 and l'_6. The parameters of the transition, such as s'_2, l'_2 and l'_3, can be tuned to get a better match between the feed line and the ridge waveguide. The dimensions of the ridge waveguide filter are presented in Table 3.1.

After obtaining the initial ridged waveguide filter configuration, this ridged waveguide filter configuration was then converted to the ridged SIW filter by employing periodic via holes. The dimensions of the ridged SIW filter were approximated by using (3-1)-(3-4). To achieve an optimal approximation, parametric analysis and optimization of the filter were carried out with HFSS™. Figure 3.5(c)-(d) shows the layout of the designed ridged SIW filter, with the dimensions of the ridged SIW filter presented in Table 3.2. The simulated responses of the ridged SIW filter and the ridged waveguide filter configuration with ideal solid walls are compared in Figure 3.6. Similarly to the resonator, very good agreement was achieved between the frequency response of the ridged SIW filter and the ridged waveguide filter.

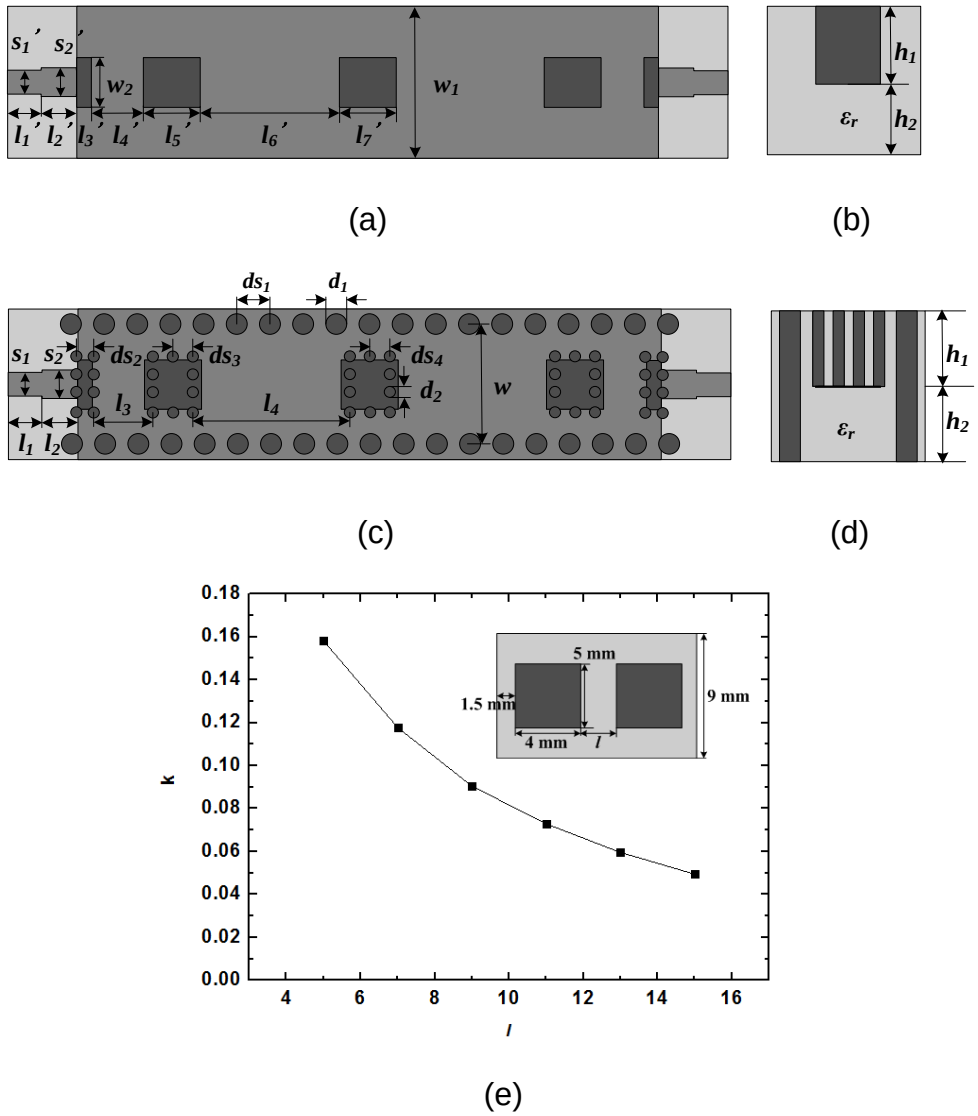

Figure 3.5 (a) Top view and (b) side view of the conventional ridged waveguide filter configuration; (c) top view and (d) side view of the ridged SIW filter; (e) the coupling coefficient k as a function of the length of the evanescent-mode coupling waveguide l (with $h_1 = h_2 = 1$ mm).

Table 3.1 Parameters of the initial ridged waveguide filter configuration (unit: mm)

s_1'	s_2'	w_1	w_2	l_1'	l_2'	l_3'	l_4'	l_5'	l_6'	l_7'
3.5	4.4	9.05	5	5	6.2	2.5	5.2	4	11	4

Table 3.2 Parameters of the ridged SIW filter (unit: mm)

s_1	s_2	w	l_1	l_2	l_3	l_4	d_1	d_2	ds_1	ds_2	ds_3	ds_4
3	4	10.	5	5	5.3	11.	1.6	1.2	2.9	1.9	2	2

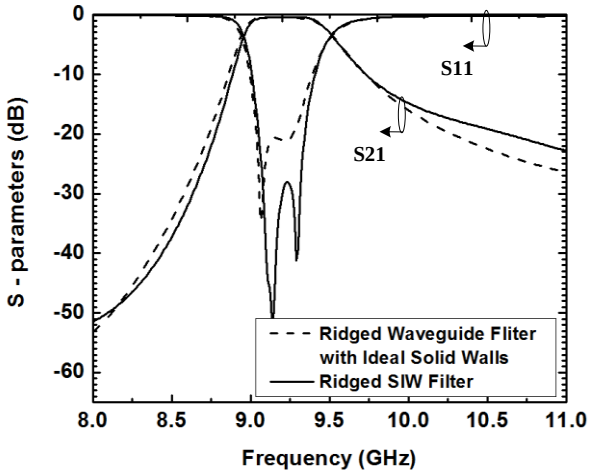

Figure 3.6 Simulated frequency responses of the ridged waveguide filter configuration and the ridged SIW filter

Figure 3.7 Photograph of the ridged SIW filter

3.3 Fabrication and Measurement

To verify the simulated results, the ridged SIW bandpass filter was fabricated on a two-layer F_4B-1/2 dielectric substrate with dielectric constant ε_r = 2.65, loss tangent of the dielectric substrate *tanδ* = 0.001, and the height of each layer being 1 mm. A photograph of the fabricated filter is shown in Figure 3.7. The frequency response of the filter was measured using an Agilent E8363A network analyzer. Figure 3.8 shows the simulated and measured frequency responses of the filter over the 8 to 11 GHz band. The measured centre frequency and 3-dB bandwidth are 9.24 and 0.6 GHz, respectively. The measured in-band return loss is below -13 dB, while the insertion loss is 3.5 dB including the feed lines and SMA connectors.

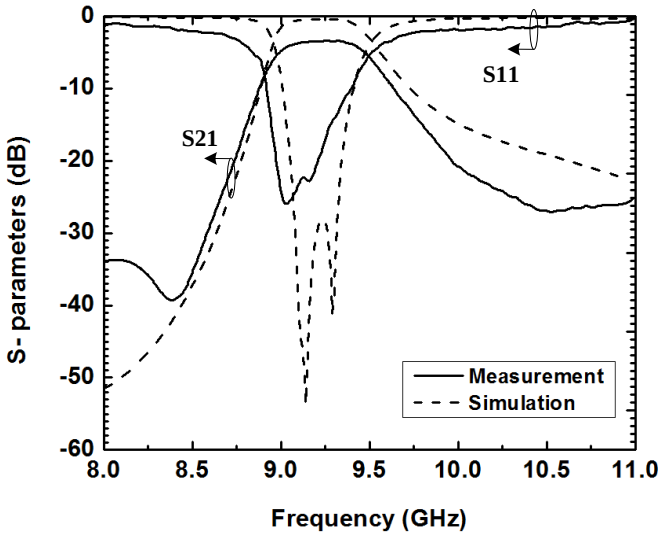

Figure 3.8 Simulated and measured frequency responses of the ridged SIW filter

3.4 Summary

In this chapter, the design and performance of a ridged SIW bandpass filter implemented by multilayer PCB are presented. The design and physical realisation of the ridged SIW resonator is first investigated, and then the ridged SIW bandpass filter is implemented on cascaded resonators coupled by evanescent-mode SIW sections. A methodology is proposed to design the ridged SIW bandpass filter. The design methodology starts from a ridged waveguide filter configuration with solid walls, and then the solid walls are converted to metallic via-fence. One prototype of the ridged SIW bandpass filter is fabricated using multilayer PCB technology and measured. The measured results agree well with the simulations. It is shown that ridged SIW bandpass filter can be efficiently designed with the proposed design methodology and realised with standard multilayer PCB technology which is comparatively convenient and inexpensive. The ridged SIW bandpass filter has the advantages of compact size, low cost and easy integration with other components and circuits, and thereby it has significant potential for use in microwave and millimetre wave systems.

Chapter 4
Compact Ridge Half-Mode SIW Filters

4.1 Introduction

As described in Chapter 2, the half-mode SIW (HMSIW) is a type of modified SIW structure which is realised by approximating the vertical cut of the SIW as a virtual magnetic wall (see Figure 4.1(a)) [37]. The HMSIW is nearly half the size of the conventional SIW but still keeps the main advantages of the SIW. Compact filters based on the HMSIW, which exhibit more compact size and wider stopband in comparison to the conventional SIW filters, have been proposed in [37, 38]. However, the size of these filters may be still too large for some applications, especially for those operating at a relatively low frequency. From the discussion in the previous chapter, we know that the ridge SIW is capable of achieving a more compact size in comparison to conventional SIWs by loading the SIW with a ridge (see Figure 4.1(b)). Since the electromagnetic field distribution of the main mode of the HMSIW is similar to half of the main mode of the SIW [37], it may be feasible to load the HMSIW with a ridge like the ridged SIW to achieve a further size reduction, while keeping the main advantages of the HMSIW.

In this chapter, a ridged half-mode substrate integrated waveguide (RHMSIW) is proposed and investigated by integrating a ridge into the HMSIW. It is shown that the RHMSIW demonstrates a lower cutoff frequency and a more compact size compared to conventional HMSIW as additional capacitance is produced by the ridge. Based on the RHMSIW, a compact wideband bandpass filter with directional coupling is designed and fabricated on multilayer PCB.

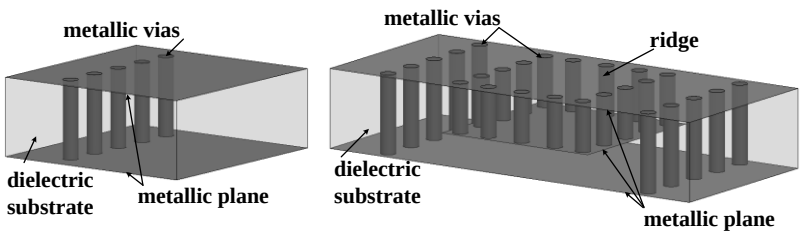

(a) (b)

Figure 4.1 (a) 3-D view of the HMSIW. (b) 3-D view of the ridge SIW

4.2 Ridge Half-Mode Substrate Integrated Waveguide (RHMSIW)

Figure 4.2 shows the proposed configuration of the RHMSIW, where a ridge is integrated into a HMSIW. The vertical solid walls of the ridge are realised with periodic metallic vias. The bottom surface of the ridge is a metal strip which connects these vias, and the top surface of the ridge overlaps with that of the HMSIW. A microstrip feed line is used at the input and output of the cavity, with a transition employed to better match the RHMSIW and the microstrip feed line. As ridge waveguides are often used for waveguide to microstrip transitions, the RHMSIW cavity is properly excited.

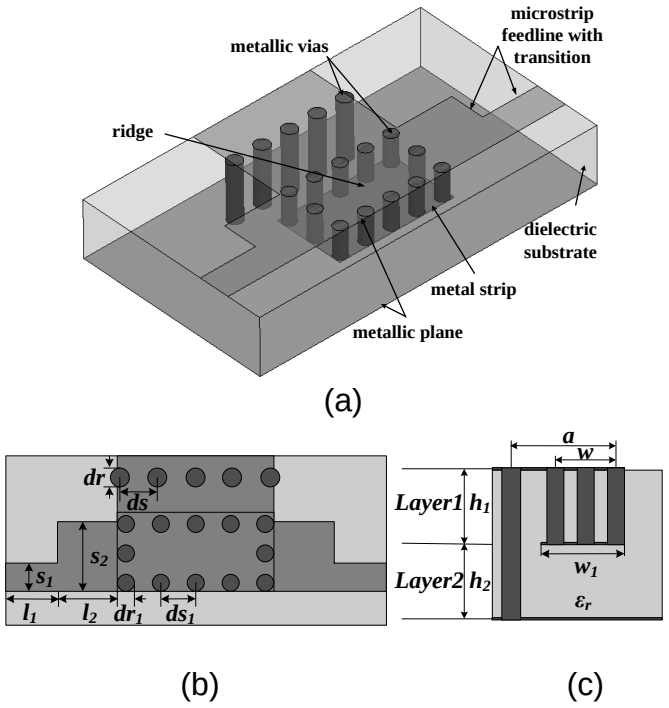

Figure 4.2 Configuration of the RHMISW: (a) 3-D view; (b) top view and (c) side view

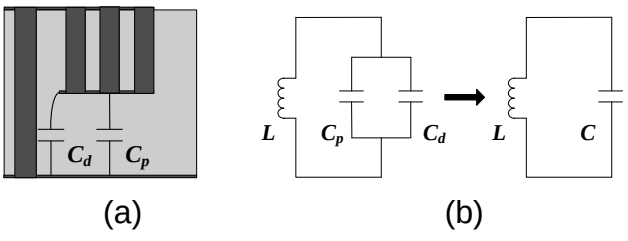

Figure 4.3 (a) The capacitance for a unit length of the RHMSIW at the cutoff frequency of the main mode. (b) Equivalent circuit model for a unit length of the RHMSIW at the cutoff frequency of the main mode

The main effect of the ridge in the RHMSIW is similar to that in the ridged SIW and the conventional ridged waveguide; it introduces additional capacitance and leads to a lower cutoff frequency for a given physical size [109]. As shown in Figure 4.3(a), the capacitance of the RHMSIW is mainly composed of two parts: the electrostatic, parallel-plate capacitance between the ridge and the bottom ground plane (C_p), and the discontinuity capacitance at the bottom corners of the ridge (C_d). Generally, the capacitance introduced by C_p is more significant than C_d. The value of C_p and C_d are dependent on the ratio h_1/h_2 and the width of the ridge, w, thereby the loading capacitance can be tuned by changing these dimensions of the ridge.

Similar to the conventional ridged waveguide [33, 109, 122], the cutoff frequency of the RHMSIW can be approximated by a simplified equivalent circuit. As shown in Figure 4.3(b), in terms of the cutoff frequency of the main mode, the RHMSIW can be modelled as a parallel *LC* tank, where the inductance *L* represents the inductance of the per unit length of the waveguide, which indicates the path that the current flow through; and the capacitor *C* represents the capacitance between the ridge and the waveguide. The cutoff frequency (f_c) of the main mode of the RHMSIW can then be approximated with the resonant frequency of the shunt-connected *LC* tank, namely:

$$f_c = \frac{1}{2\pi\sqrt{LC}} \tag{4-1}$$

where the capacitance *C* can be expressed by:

$$C = C_p + C_d \tag{4-2}$$

From equations (4-1) and (4-2), it can be seen that as a larger parallel-plate capacitance (C_p) and an extra discontinuity capacitance (C_d) is introduced in waveguide by loading a ridge, the RHMSIW exhibits a lower cutoff frequency in comparison to the conventional HMSIW.

An example of the RHMSIW was designed and investigated with the parameters (see Figure 4.2) chosen as follows: ε_r = 2.65, $h_1 = h_2$ = 0.5 mm, s_1 = 2.2 mm, s_2 = 4.6 mm, l_1 = 5.3 mm, l_2 = 6.4 mm, dr = 1.1 mm, ds = 2 mm, dr_1 = 1 mm, ds_1 =1.85 mm, a = 7.85 mm, w = 3.7 mm, w_1 = 5.2 mm. It is important to notice that the distance between two adjacent vias (the via hole pitch, denoted by ds and ds_1 in Figure 4.2) should be less than twice of the diameter of the via (dr and dr_1) to achieve a better approximation to the ideal

vertical walls [123]. The frequency responses of the RHMSIW were simulated by the HFSS^{TM} and the results are presented in Figure 4.4. A good high-pass response with a cutoff frequency of 4 GHz is observed. For comparison, the simulated frequency response of the conventional HMSIW with the waveguide dimensions identical to that of the RHMSIW was also investigated and plotted in Figure 4.4. As expected, the cutoff frequency of the HMSIW, which is at 6.5 GHz, is much higher than that of the RHMSIW (4 GHz). For a conventional HMSIW with the cutoff frequency of the main mode at 4 GHz, the width of the waveguide needs to be 11.8 mm, and this is much wider than that of the RHMSIW (7.85 mm). Therefore, the RHMSIW is more compact compared to the conventional HMSIW. Furthermore, since the loading capacitance between the ridge and the bottom ground plane of the waveguide (C_p) increases with the increase of the height of the ridge (h_1) and the decrease of the height of the gap between the ridge and the bottom ground plane (h_2), a further size reduction could be achieved for the RHMSIW by increasing the ratio h_1/h_2 appropriately.

To better understand the structure of the RHMSIW, the electric field distribution of the main mode in the RHMSIW was also investigated. As depicted in Figure 4.5(a), the electric field of the RHMSIW is similar to that of the HMSIW and the ridge SIW, being basically perpendicular to the bottom ground plane and reaching the maximum near the open aperture. By comparing the E-field distribution of the main mode of the RHMSIW with that

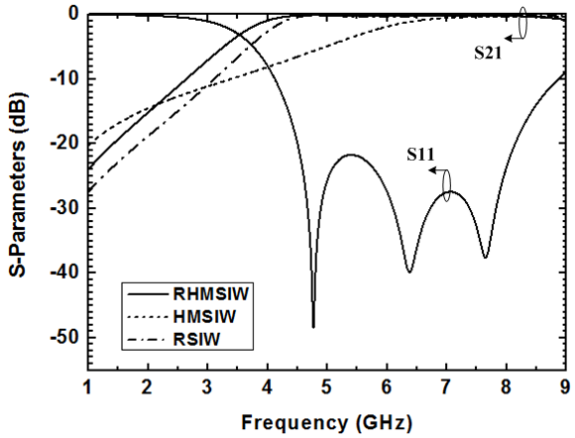

Figure 4.4 Simulated frequency response of the RHMISW, compared with the HMSIW with identical waveguide dimensions, and the ridge SIW with the width of the waveguide and the ridge twice that of the RHMSIW

of the ridged SIW, with the width of the waveguide and the ridge twice that of the RHMSIW (see Figure 4.5(b)), it can be seen the electric field distribution of the RHMSIW is quite similar to half that of the ridged SIW. This is not unexpected. Since the electric field of the main mode of the ridge SIW is basically orthogonal to the bottom broadwall of the waveguide and it is maximum at the vertical centre plane of the bottom layer, this vertical centre plane along the direction of propagation could be approximated as a virtual magnetic wall (see the inset of Figure 4.5(b)). Therefore, the RHMSIW could be viewed as half of the ridged SIW which is bisected with this virtual magnetic wall. Furthermore, due to the large width-to-height ratio, the dominant mode field distribution and propagation characteristics of the RHMSIW are similar to that of the ridge SIW. Figure 4.4 presents the simulated frequency responses of the ridged SIW with the width of the waveguide and the ridge twice that of the RHMSIW. It can be seen that the cutoff frequency of the ridged SIW is at 4.12 GHz, which is quite close to that of the RHMSIW (4 GHz). This also indicates that the proposed RHMSIW works similarly to the ridge SIW but with the physical size reduced to half.

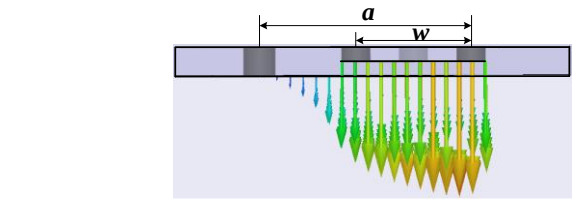

(a)

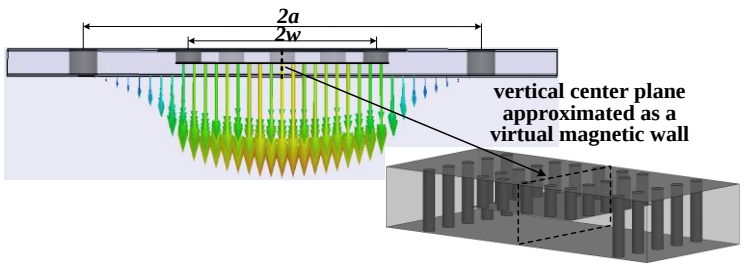

(b)

Figure 4.5 Electric field distribution of the main mode in the: (a) RHMSIW and (b) ridged SIW with the width of the waveguide and the ridge twice that of the RHMSIW

Based on the analysis above, in the design of a practical device with the RHMSIW, the width of a conventional ridged waveguide with vertical solid walls and working in the same frequency could be determined firstly with the classic theory of ridged waveguide [33, 122]. This ridged waveguide can then be converted into a ridged SIW by using periodic via holes to replace the vertical solid walls. The design rules for the via holes shown in [72, 112, 123] could be used to achieve a better approximation to the ideal vertical walls, namely:

$$ds \leq 2 \cdot dr \tag{4-3}$$

$$ds_1 \leq 2 \cdot dr_1 \tag{4-4}$$

where *dr* and *ds* are the diameter of the vias forming the waveguide and the via pitch, respectively; dr_1 and ds_1 are the diameter of the vias forming the ridge and the via pitch, respectively (see Figure 4.2). The width of the RHMSIW is then approximately half that of the ridged SIW, which could be used as initial dimensions for the design of the RHMSIW.

4.3 Compact Wideband Bandpass Filter with the RHMSIW

Based on the configuration of the RHMSIW, a compact wideband RHMSIW bandpass filter with directional coupling was designed and simulated with HFSS^{TM}. The layout of the RHMSIW bandpass filter is shown in Figure 4.6(a)-(b). The filter is directly coupled by the HMSIW sections. A transition was used to better match the RHMSIW and the microstrip feed lines. The initial dimensions of the RHMSIW can be approximated by half of the ridge waveguide working in the same cutoff frequency, as described in section 4.2. The centre frequency of the filter can be adjusted by tuning the parameters dr_1 and ds_1, which are relevant to the equivalent length of the ridge. The coupling between resonators can be tuned by changing the length of the HMSIW sections, l_4 and l_6. The parameters of the filter after tuning are shown in Table 4.1.

A two-layer F_4B-1/2 dielectric substrate was used to fabricate the filter with dielectric constant ε_r = 2.65, the loss tangent of the dielectric substrate $tan\delta$ = 0.001, and the thickness of upper layer and lower layer being 1 mm and 0.5 mm, respectively. Figure 4.6(c) shows a photograph of the fabricated RHMSIW filter. The filter was measured with an Agilent E8363A network analyzer.

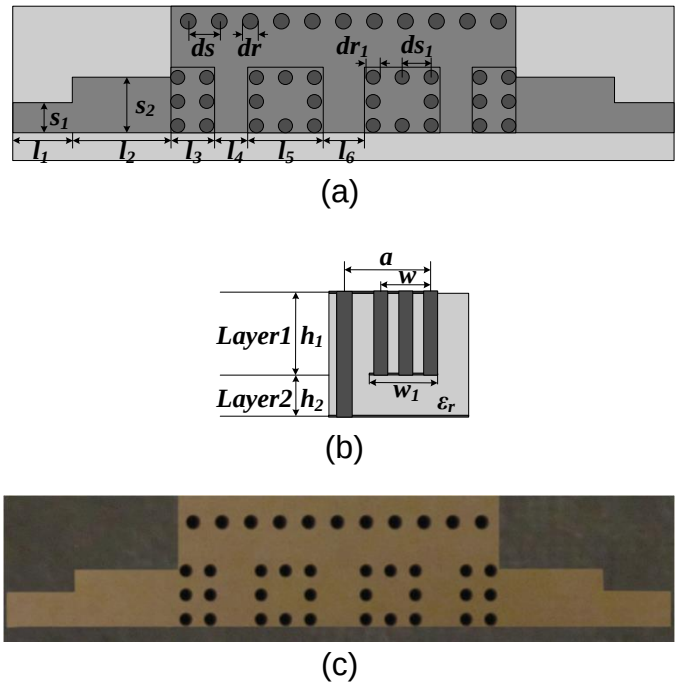

Figure 4.6 (a) Top view showing the layout of the wideband RHMSIW filter. (b) Cross-sectional view of the filter. (c) Photograph of the fabricated filter

Table 4.1 Parameters of the RHMSIW filter (unit: mm)

ε_r	h_1	h_2	s_1	s_2	l_1	l_2	l_3	l_4	l_5	l_6	dr
2.65	1	1	2.5	4.1	5.3	7.6	2.8	3.75	4.8	1.8	1.1
ds	dr_1	ds_1	a	w	w_1						
2.1	1	1.87	7.85	3.6	4.8						

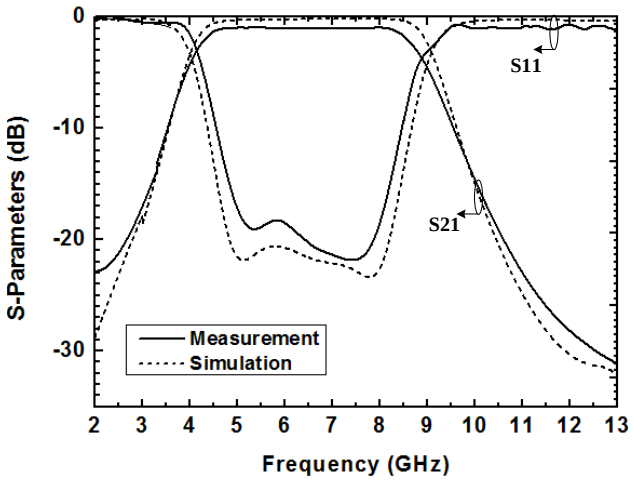

Figure 4.7 Simulated and measured frequency responses of the wideband RHMSIW filter

The measured and simulated frequency responses of the filter are depicted in Figure 4.7. Good agreement is achieved between the measurement and the simulation. The measured centre frequency and 3-dB bandwidth are 6.47 and 4.9 GHz, respectively. The measured in-band return loss is better than 18 dB. The insertion loss is 1 dB including the feed lines and SMA connectors. The size of the filter is only 18.3 mm × 8.4 mm × 1.5 mm without the feed line. Moreover, by using a thicker dielectric substrate for the ridge or a thinner dielectric substrate for the gap between the ridge and the bottom ground plane, the size of the filter could be further reduced.

4.4 Summary

In this chapter, the design and performance of a compact wideband filter based on the RHMSIW (ridged half-mode substrate integrated waveguide) are presented. The proposed RHMSIW shows a lower cutoff frequency and a more compact size compared to the conventional HMSIW due to the additional capacitance introduced by the loaded ridge. Further physical size reduction could be achieved for the RHMSIW by increasing the height of the ridge or decreasing the gap between the ridge and the bottom ground plane appropriately. A compact wideband bandpass filter with the RHMSIW has been designed and fabricated. Good agreement has been achieved between the measurement and the simulation. The proposed filter is compact, low loss, easy to fabricate and integrate with other components and circuits. It has significant potential for use in microwave and millimeter wave systems.

Chapter 5
SIW Filters with Modified Complementary Split Ring Resonators (CSRRs)

5.1 Introduction

Recently, substrate integrated waveguide incorporating electromagnetic bandgap structures such as the split ring resonator (SRR) [39] and complementary split ring resonator (CSRR) [41] has been widely investigated for the design of miniature filters [52, 71]. The SRR is capable of generating a negative value of the effective permeability in the vicinity of resonance, and it can be modelled as a resonant *LC* tank driven by external magnetic fields. The CSRR is the negative image of the SRR. It can produce negative effective permittivity and behaves as a resonant *LC* tank driven by proper electric fields. When the SRRs/CSRRs are integrated into a waveguide, they can produce passband below the cutoff frequency of the waveguide or stopband above the cutoff frequency due to the negative permeability/permittivity introduced in the waveguide. Making use of this property, several miniaturized waveguide filters implemented with classic edge-coupled SRRs (EC-SRRs) and edge-coupled CSRRs (EC-CSRRs) have been developed. For example, in [31, 32], wide-band SIW bandpass filters were proposed by combining the stopband of periodical CSSRs with the high-pass band of the SIW. In [48, 52], novel compact SIW bandpass filters loaded by CSRRs were proposed by using the passband below the cutoff frequency of the SIW. However, as has been described in Chapter 2, since the size reduction of these filters is mainly through the decrease of the spacing between the rings of the EC-SRR/EC-CSRR, these filters are limited in compactness as a very small spacing in the EC-SRR/EC-CSRR may cause inconvenience in fabrication as well as potential high losses and dielectric break [49].

In this chapter, two types of modified CSRRs are proposed to improve the compactness and performance of SIW filters: the broadside coupled complementary split ring resonator (BC-CSRR) and the capacitance-loaded complementary single split ring resonator (CSSRR). The BC-CSRR is proposed based on the broadside-coupled SRR (BC-SRR) [50] by using the duality concept. It is shown that the proposed BC-CSRR is capable of achieving a more compact size conveniently by just using a thin dielectric

substrate. Moreover, since the capacitance between the broadside-coupled rings of the BC-CSRR can be made considerably higher than that between the edge-coupled rings (such as using a very thin dielectric substrate), the proposed BC-CSRR allows for a much smaller physical size in comparison to conventional EC-CSRRs. Based on the configuration of the BC-CSRR, four distinct types of SIW resonators are proposed by changing the orientations of the BC-CSRRs and the effect of the orientation of the BC-CSRRs on the frequency response is investigated (see section 5.2); a modified form of BC-CSRRs with improved stopband performance is developed by altering the configuration of BC-CSRR pairs, and a SIW filter with a wide rejection band is realised using the proposed modified BC-CSRRs (see section 5.3). Furthermore, a new capacitively-loaded CSSRR is proposed to reduce the physical size of the CSSRR by adding an overlap region between the inner metal disk and the ground plane of the CSSRR. A miniaturized HMSIW filters is realised by employing the proposed capacitively-loaded CSSRR (see section 5.4).

5.2 SIW Filters with Side-by-Side Oriented Broadside-Coupled Complementary Split Ring Resonator (BC-CSRR) Pairs

In this section, the configuration of the BC-CSRR is proposed and four designs of SIW filters employing integrated BC-CSRR pairs are compared. By changing the orientation rings, four types of SIW unit cell are proposed and investigated and it is shown that, for one particular topology, two poles and two zeroes can be realised with a single unit cell. Bandpass filters based on the proposed resonators coupled by evanescent-mode SIW sections have been fabricated and tested.

5.2.1 Type I Structure

5.2.1.1 Configuration of the BC-CSRR

The broadside-coupled split-ring resonator (BC-SRR) was first proposed in [50]. Figure 5.1(a) shows the structure of the BC-SRR, which can be derived from the EC-SRR by replacing one of the rings by another ring located just at the opposite side of the dielectric substrate, with the slits still placed at opposite sides. The electromagnetic behaviour of the BC-SRR is similar to that of the SRR in many essential aspects. It behaves as a *LC* resonant tank that can be driven by proper magnetic fields. However, the BC-SRR is capable of achieving an even smaller physical size in comparison to

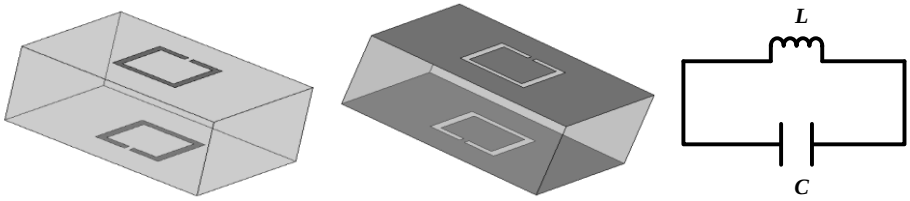

(a) (b) (c)

Figure 5.1 (a) Topology of the BC-SRR. (b) Topology of BC-CSRR. (c) Equivalent-circuit model of the BC-CSRR. Grey shading represents the metallization

conventional EC-SRRs, due to a higher capacitance that can be obtained between the broadside-coupled metallic strips of the BC-CSRR than that between the edge-coupled split rings [50].

From the duality condition, the negative image of the BC-SRR is proposed here and referred to as the broadside-coupled complementary split-ring resonator (BC-CSRR). The new element and its equivalent circuit are illustrated in Figure 5.1(b)-(c). Similar to the EC-CSRR, the BC-CSRR can be considered as a *LC* resonant tank driven by external electric fields.

5.2.1.2 SIW with a Side-by-Side Aligned BC-CSRR Pair

The layout of the SIW structure with a pair of BC-CSRRs, hereafter referred to as the Type I structure, is shown in Figure 5.2(a)-(c). A pair of identical BC-CSRRs is etched on the SIW top and bottom broadwalls, with the resonators aligned side by side but at 180º to one another. A microstrip feed line is used to excite the SIW, with an inset transition employed to get a better match. Since the electric field of the dominant mode within the SIW is orthogonal to the top and bottom surfaces, the CSRRs are properly excited [52].

The equivalent circuit of the SIW with EC-CSRR pairs has been investigated in [31]. Here, through similar analysis, the proposed unit cell can be modelled with a simplified equivalent circuit within a limited frequency range. As shown in Figure 5.2(d), the metallic vias of the SIW are modelled as L_v; the BC-CSRR pair is modelled by means of the shunt-connected resonator composed of the capacitance C_b and the inductance L_b; L_c denotes the inductive coupling which is mainly through the split of the ring between the SIW and the BC- CSRRs; C_c represents the capacitive coupling which is mainly realised by the slot coupling between the SIW and the BC-CSRRs.

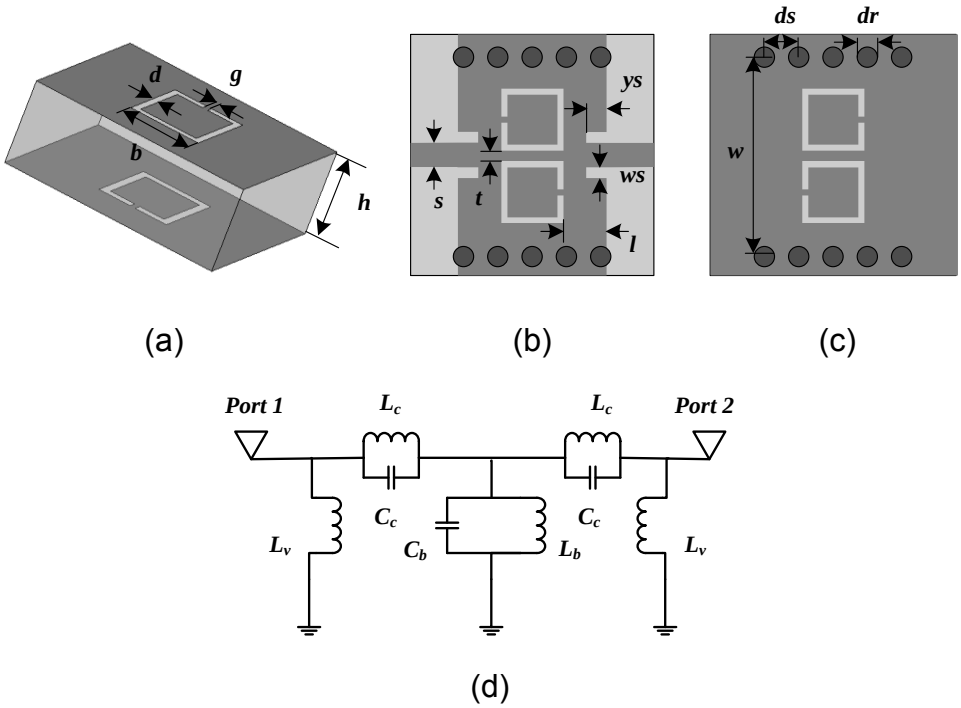

Figure 5.2 (a) Configuration of the BC-CSRR. (b) Top view of the configuration of the type I unit cell of the BC-CSRR pair. (c) Bottom view. (d) Equivalent circuit model. Gray shading represents the metallization

To get the values of the equivalent circuit model of the proposed unit cell, the values of the equivalent capacitance (C) and inductance (L) of the corresponding BC-SRR can be obtained with the method shown in [115] firstly; since the BC-CSRR can be viewed as the negative image of the BC-SRR, the parameters of the LC circuit model of the BC-CSRR can then be approximated from the duality by $C_b = 4(\varepsilon/\mu)L$ and $L_b = C/(4(\varepsilon/\mu))$, where ε and μ are the permittivity and permeability of the dielectric substrate, respectively. The values of other electric parameters, L_v, L_c and C_c, can be approximated by using the method presented in ref. [124]. After determining the initial parameters of the BC-CSRR, the accurate values of the equivalent circuit model of the SIW BC-CSRR unit cell can then be achieved by carrying out the simulation and optimization with the Ansoft Designer software.

An example of the unit cell of the SIW with the BC-CSRR pair was designed and investigated, with the dielectric constant of the substrate $\varepsilon_r = 2.65$ and the width of the waveguide, w, set to 12.5 mm to achieve a nominal waveguide cutoff frequency of 8.15 GHz. The HFSS^{TM} and circuit model simulated frequency responses of the SIW BC-CSRR unit cell are depicted

in Figure 5.3(a) (with the dimensions of the unit cell and lumped-element values of the circuit model shown in the caption). Good agreement has been achieved between the HFSS™ and circuit model simulations. A passband with a centre frequency of 5.61 GHz is observed. It is shown that the resonant frequency of the SIW BC-CSRR unit cell is clearly well below the cutoff frequency of the original SIW.

To better understand the response of the proposed unit cell, we derive the dispersion relation of the equivalent circuit (see Figure 5.2(d)) from classical circuit theory [5]. For simplicity, the vias, denoted by L_s, are not taken into consideration. The series impedances Z_s and shunt impedances Z_p are then given by:

$$Z_s = \frac{j\omega L_c}{1-\omega^2/\omega_1^2} \tag{5-1}$$

$$Z_p = \frac{j\omega L_b}{1-\omega^2/\omega_0^2} \tag{5-2}$$

where $\omega_1^2 = 1/(L_cC_c)$, $\omega_0^2 = 1/(L_bC_b)$. The dispersion relation can then be calculated by:

$$\cos\phi = \cos(\beta l) = 1+\frac{Z_s}{Z_p} = 1+\frac{L_c\left(1-\omega^2/\omega_0^2\right)}{L_b\left(1-\omega^2/\omega_1^2\right)} \tag{5-3}$$

Wave propagation is expected in the region where β is real. By inserting the values of the lumped elements in the caption of Figure 5.3 into (5-1)-(5-3), the relation between β and ω is obtained. As shown in Figure 5.3(b), wave propagation is allowed between 5.03 GHz to 5.78 GHz, which agrees well with the simulated passband in Figure 5.3(a). On the other hand, it is noted that, in the region between 5.03 GHz to 5.78 GHz, β increases with frequency, which means forward wave propagation. This can also be explained from the perspective of an effective medium filling the SIW. A waveguide filled with electric dipoles, namely metallic rods, has been investigated using an anisotropic electric plasma approach in [125]. Through a similar analysis, the SIW with BC-CSRRs can also be considered as an equivalent rectangular waveguide filled with an anisotropic electric plasma with the relative permeability $\mu_r = 1$. From [125], the dispersion relation for the fundamental mode can then be approximated by:

$$\beta^2 = -\gamma^2 = k^2 \frac{\varepsilon}{\varepsilon_0} - k_x^2 = k^2 \frac{\varepsilon}{\varepsilon_0} - \left(\frac{\pi}{W_{eff}}\right)^2 \tag{5-4}$$

where $k^2 = \omega^2\mu_0\varepsilon_0$, W_{eff} is the equivalent width of the SIW. The wave propagates at the frequencies where $\varepsilon > \varepsilon_0(\pi/(k\, W_{eff}))^2$. On the other hand, it can be seen that it is a forward wave, i.e., $d\beta/d\omega > 0$, which follows from Foster's theorem $d\varepsilon/d\omega > 0$ [116, 117].

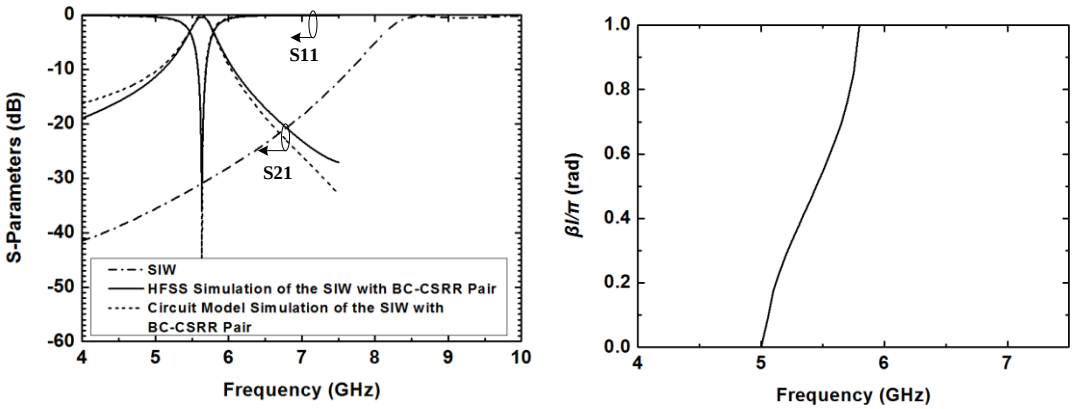

(a) (b)

Figure 5.3 (a) HFSS^{TM} and circuit model simulated frequency responses of the standard SIW and the type I unit cell (with parameters h = 1 mm, b = 3.9 mm, g = 0.3 mm, d = 0.34 mm, t = 0.5 mm, w = 12 mm, s = 2.65 mm, ws= 0.5 mm, ys = 1.5 mm, l = 2.5 mm, dr = 1.2 mm, ds = 2.2 mm, L_v = 2.5 nH, L_c = 1.88 nH, C_c = 0.16 pF, L_b = 0.5 nH, C_b = 2 pF). (b) Theoretical dispersion relation for the type I unit cell

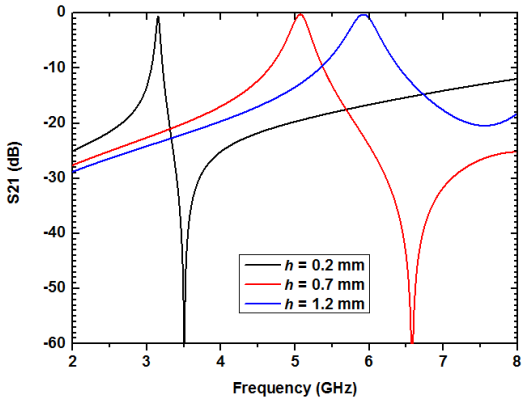

Figure 5.4 Simulated frequency response for different substrate thicknesses, h

Since the capacitance between the broadside coupled metallic strips of the BC-SRR can be made high, resulting in a smaller overall physical size of the element [50], it is expected that the proposed SIW BC-CSRR resonator has similar properties. Figure 5.4 presents the results by changing the thickness of the substrate, *h*. It can be seen that the resonant frequency is significantly reduced when *h* is smaller, with the total size of the resonator remaining unchanged. In this case, the capacitance between the broadside-coupled rings of the BC-CSRRs is significantly increased with the reduction of *h*, as a result a lower resonant frequency is obtained. On the other hand, a transmission zero is also introduced when *h* is small. These properties indicate that quite a compact size as well as improved performance could be achieved for the proposed resonator just by using a very thin substrate.

5.2.2 Type II, III and IV Unit Cells

CSRRs exhibit different transmission responses when the orientation is altered [126]. This has been illustrated in [31], where the SIW with EC-CSRRs are investigated and the effect of changing the orientation of the EC-CSRRs on the frequency responses is analysed. With a similar method, the proposed SIW BC-CSRR resonator structure is further investigated by varying the orientation of the BC-CSRRs. However, it should be noted that, since the coupling and the distribution of the electromagnetic fields of BC-CSRRs are different from EC-CSRRs, the influence of the orientation of the BC-CSRR on the frequency response may be also quite different from that of the EC-CSRR shown in [31].

Figure 5.5 shows the configuration of three types of SIW BC-CSRR resonator pairs with different orientations for the top layer rings compared to the type I unit cell (see Figure 5.2). Figure 5.5(a) presents the Type II unit cell, where the rings on the top are now aligned face-to-face, while the rings on the lower broadwall have not changed orientation but are now united along one edge to enhance the capacitive coupling. In the Type III structure, as shown in Figure 5.5(b), the rings on the top surface have been flipped so that the slits now align with the corresponding ring on the bottom. Finally, the Type IV structure, as shown in Figure 5.5(c), uses top-side rings that are back-to-back. Again, the rings on the bottom are unified along a common side.

The transmission responses of the three types of unit cells simulated using HFSS™ are plotted in Figure 5.6. It can be seen that, compared with the Type I element (see Figure 5.3(a)), good filtering responses with broader

bandwidth have been achieved for the last three types, which indicates stronger effective coupling between the two modified BC-CSRRs. On the other hand, compared with the second and third structures which have transmission zeros only in the upper stopband (see Figure 5.6(a), (b)), the Type IV exhibits a transmission zero in both the upper and lower stopband (see Figure 5.6(c)), thus showing it has excellent potential for realising miniature filters with good selectivity.

To further investigate the transmission characteristics of the Type II, III and IV unit cells, the equivalent circuit model has been derived and investigated through analysis similar to that employed in the equivalent circuit model of the type I unit cell (see Figure 5.2(d)). As shown in Figure 5.5(d), the metallic vias of the SIW are again modelled as L_v. L_c denotes the inductive coupling that is mainly through the split of the ring between the SIW and the CSRRs. C_c represents the capacitive coupling that is mainly realised by the slot coupling between the SIW and the CSRRs. The modified BC-CSRR is

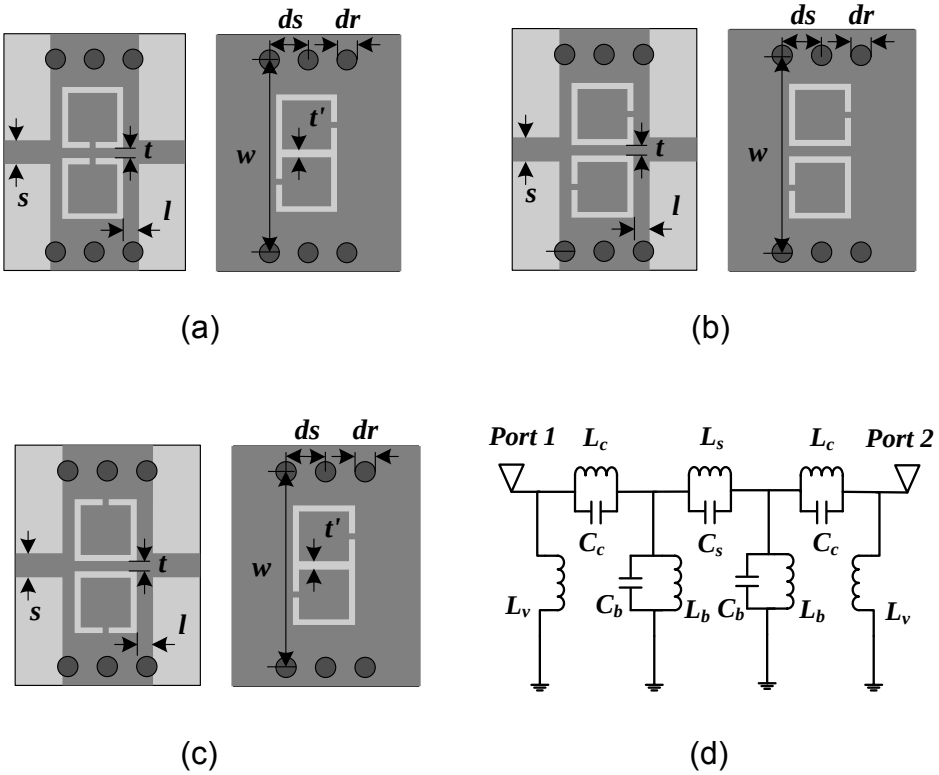

Figure 5.5 (a) Layout of the type II unit cell of the BC-CSRR resonator pair. (b) Layout of the type III unit cell. (c) Layout of the type IV unit cell. (d) Equivalent circuit model for type II, type III and type IV unit cells

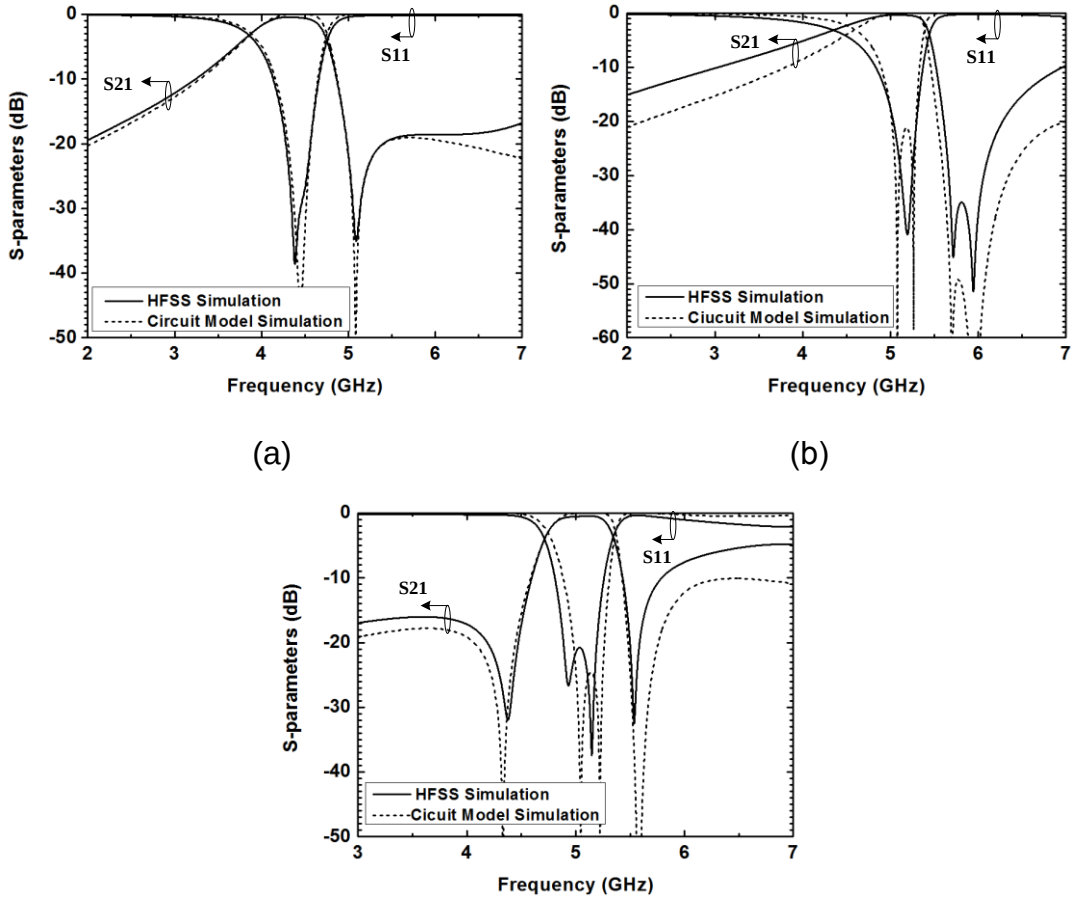

Figure 5.6 HFSS^{TM} and circuit model simulated frequency responses of the: (a) type II unit cell, (b) type III unit cell and (c) type IV unit cell. The parameters for the type II unit cell are: ε_r = 3.48, h = 0.762 mm, b = 3.9 mm, g = 0.3 mm, d = 0.34 mm, w = 12.5 mm, s = 1.68 mm, l = 0.5 mm, dr = 1.2 mm, ds = 2.2 mm, t = 0.75 mm, and t' = 0.33 mm; for type III,part of the parameters are revised as t = 1.3 mm, others are the same; for type IV,part of the parameters are revised as t = 1.1 mm and t' = 0.38 mm, others are the same

Table 5.1 Lumped-element values of the circuit model of the Type II, III and IV unit cells

	L_v (nH)	L_c (nH)	C_c (pF)	L_s (nH)	C_s (pF)	L_b (nH)	C_b (pF)
Type II	3.6	0.35	0.65	0.49	2	0.595	2.9
Type III	4.2	0.3	2.38	0.668	1.147	0.597	2.15
Type IV	4	0.18	4. 52	1	1.35	0.6	1.81

modelled by means of the shunt-connected resonator with the capacitance C_b and the inductance L_b. However, compared with the equivalent circuit model of the first type, in terms of the last three types, the mutual coupling between resonators should be taken into account. The coupling mechanisms for the SRRs have been investigated in [127]. Here, the coupling between modified BC-CSRRs is considered as a combination of electric and magnetic types, described by C_s and L_s, respectively. The values of the equivalent circuit model of these three new unit cells can be obtained following similar procedures to the type I unit cell.

The simulated frequency responses of the three new unit cells from the equivalent circuit model and the HFSS™ are presented in Figure 5.6 (with the values of the lumped elements depicted in Table 5.1). As shown in Figure 5.6(a), for the type II unit cell, a transmission zero is introduced above the passband. This is due to the mutual coupling between the modified BC-CSRRs, denoted by C_s and L_s in the circuit model. At the frequency where the admittance of the branch is null, the branch opens and the signal propagation is suppressed, leading to a transmission zero at:

$$f_{z1} = \frac{1}{2\pi\sqrt{L_s C_s}} \tag{5-5}$$

The type III unit cell introduces an additional transmission zero which is above the first transmission zero. This additional transmission zero is created by the coupling between the SIW and the modified BC-CSRRs, represented by L_c and C_c in the equivalent circuit model, which gives a transmission zero located at:

$$f_{z2} = \frac{1}{2\pi\sqrt{L_c C_c}} \tag{5-6}$$

In addition, as the rings on the bottom are not united along the common side, the type III structure has a weaker mutual capacitive coupling (C_s) and the frequency of the corresponding transmission zero, f_{z1}, is slightly higher than that of the type II.

For the type IV structure, like the type III there are two transmission zeros. However, whereas that has both transmission zeros in the upper stopband, type IV has one each in the upper and lower stopband, as shown in Figure 5.6(c). This is due to the increase of the inductance L_s and the capacitance C_s in the circuit model (see the values of the lumped elements in Table 5.1). When the rings on the top are aligned back-to-back, the mutual inductive

coupling is reduced as they can only receive limited energy though the split. The corresponding inductance L_s thus increases. In the meanwhile, since the two rings on the bottom of type IV structure are united along the common side, the mutual capacitive coupling is enhanced and thus the corresponding capacitance (C_s) increases. Therefore, the corresponding transmission zero frequency described by (5-5) also shifts down.

The variation of the orientation of the top rings of the BC-CSRR pairs changes not only the mutual coupling between the BC-CSRR pairs but also the coupling between the SIW and the BC-CSRR. As shown in Table 5.1, the value of C_c increases from type-II to type-IV unit cells by a most significant factor of 7. This is due to the increase of capacitive coupling between the SIW and the BC-CSRR. As is well known, the electric field of the CSRR is mainly distributed around the ring and reaches its maximum in the vicinity of the slot opposite to the split of the ring. When the orientation of the top layer rings of the BC-CSRR pair change from face-to-face to back-to-back (i.e., from type-II to type-IV unit cells), the capacitive coupling between the SIW and the BC-CSRR becomes easier as the slot opposite to the split of the top ring, where the electric field is maximum, is close to the centre. Therefore, the corresponding capacitance (C_c) increases.

5.2.3 Bandpass Filters with the Proposed Resonator Structures

In this section, bandpass filters using the Type I, II, III, IV cells are designed and optimized using HFSS™. They are based on resonators coupled by an evanescent-mode waveguide section. The filters were fabricated using a standard PCB etching process and measured with an Agilent E8363A network analyzer.

5.2.3.1 Type I Bandpass Filter

A second-order bandpass filter based on the type I unit cell (see Figure 5.2) was designed and optimised with HFSS™. The layout of the filter is presented in Figure 5.7(a), where two identical BC-CSRR pairs are employed and coupled with an evanescent-mode waveguide section. The centre frequency of the filter can be tuned by changing the length of the BC-CSRR (*b*), the width of the slot (*d*) and the width of the gap (*g*). The decrease of *d* and *g*, or the increase of *b* could lead to a lower centre frequency (see Figure 5.9(a)). The bandwidth of the filter can be adjusted by varying the length of the evanescent-mode SIW section (*ld*). As illustrated in Figure 5.9(b), a larger *ld* could lead to a weaker coupling and a narrower

bandwidth. In addition, the parameters of the transition, namely, the length (*ys*) and width (*ws*) of the slot of the transition, can be adjusted to achieve a better match between the BC-CSRR and the input microstrip. However, it should be noted that the variation of the width of the SIW (*w*) can also influence the filter response. As shown in Figure 5.9(c), the bandwidth of the filter is widened with the increase of *w*. This is due to the increase of coupling between resonators with increase of *w*. When *w* increases, the cutoff wavelength of the waveguide (λ_c) is increased, therefore, the evanescent-mode coupling between resonators is enhanced and hence the bandwidth is widened [128].

A prototype of the filter based on the type I unit cell was fabricated. The filter was fabricated on the dielectric substrate F_4B-1/2 with ε_r = 2.65 and thickness of 1 mm. Figure 5.8(a) shows a photograph of the fabricated filter. The size of the filter, excluding feed-lines, is 20 mm × 13 mm. Detailed dimensions of the filter are given in Table 5.2.

Figure 5.10(a) shows the simulated and measured frequency responses of the filter over the 4.5 to 7.5 GHz band. The measured centre frequency and 3 dB bandwidth are 5.75 and 0.3 GHz, respectively. The in-band return loss is better than 12 dB and the insertion loss is 4 dB including the microstrip feed lines and SMA connectors.

5.2.3.2 Bandpass Filters with Type II, III and IV Unit Cells

Second-order SIW bandpass filters with the type II (as per Figure 5.5(a)), type III (see Figure 5.5(b)) and type IV (see Figure 5.5(c)) unit cells were designed and optimized with HFSS™ following similar procedures to the design and optimization of the filter with type I unit cells. These filters were fabricated on Rogers 4350 substrate with ε_r = 3.48 and thickness of 0.762 mm. Figure 5.7(b)-(d) and Figure 5.8(b)-(d) show the layouts and the photographs of the filters based on these three new types of unit cell, with detailed dimensions provided in Table 5.2. The simulated and measured transmission responses of the SIW filters are presented in Figure 5.10(b)-(d).

Figure 5.10(b) presents the simulated and measured transmission responses of the SIW filters based on the type II unit cell. The measured centre frequency and 3 dB bandwidth of the fabricated filter are 4.43 and 0.69 GHz, respectively. The measured insertion loss is approximately 1.4 dB including the feed lines and SMA connectors. A transmission zero located in the upper band is observed. Due to the existence of the transmission zero,

the measured stopband rejection is better than 25 dB from 5.06 GHz to 7.5 GHz.

Figure 5.10(c) shows the simulated and measured transmission responses of the filter based on the type III unit cell over the 3 to 9.25 GHz band. It can be seen that the measured centre frequency and 3 dB bandwidth are 5.15 and 0.85 GHz, respectively. The measured insertion loss is approximately 1.1 dB including the feed lines and SMA connectors. Moreover, two transmission zeros located in the upper band are obtained. The measured stopband rejection from 5.73 GHz to 9 GHz is better than 20 dB.

The simulated and measured transmission responses of the filter with the type IV unit cell over the 3 to 6.5 GHz band are depicted in Figure 5.10(d). The measured centre frequency and 3 dB bandwidth are 5.1 and 0.37 GHz, respectively. The measured insertion loss is approximately 4 dB including the feed lines and SMA connectors. It can be seen that the measured loss of type IV filter is higher than that of the type II and type III filters. This might result from the narrow bandwidth of the filter. Since the bandwidth of the type IV filter is much narrower than that of the type II and type III filters, the length of the evanescent-mode SIW section (*ld*) of type IV filters needs to be much longer than that of the type II and type III filters in order to achieve a weaker coupling. From Table 5.2, it can be seen that the value of *ld* for the type IV filters is indeed much larger than that of the type II and type III filters. The increase of *ld* could lead to a higher dielectric loss and conductor loss, therefore, the type IV filter shows a higher insertion loss than that of the type II and type III filters. However, for the type IV filter, transmission zeros located both in the upper and lower stopband have been achieved. Therefore, compared with the previous three types of filters, it shows improved selectivity.

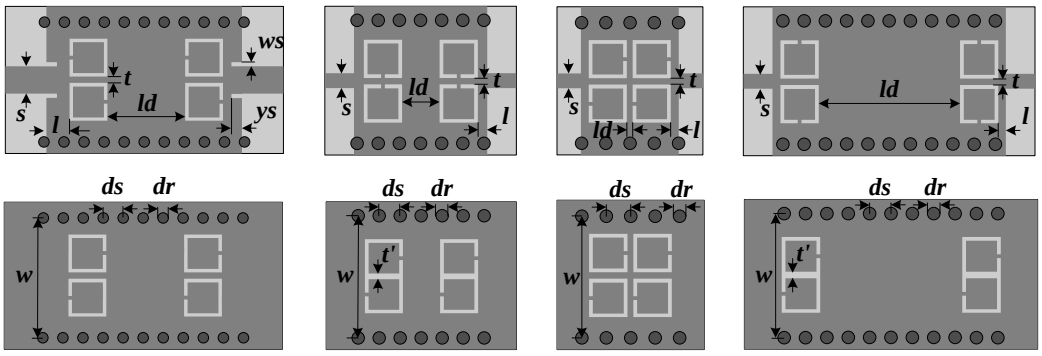

(a) (b) (c) (d)

Figure 5.7 Layout of the filters base on: (a) type I unit cells, (b) type II unit cells, (c) type III unit cells and (d) type IV unit cells

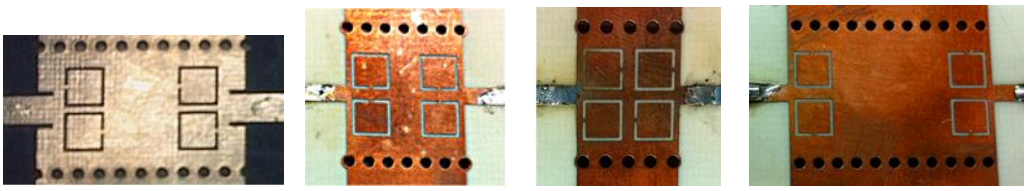

(a) (b) (c) (d)

Figure 5.8 Top view of the photograph of the fabricated filters base on: (a) type I unit cells, (b) type II unit cells, (c) type III unit cells and (d) type IV unit cells

Table 5.2 Parameters of the filters based on the type I, type II, type III and type IV unit cells (unit: mm)

	b	*g*	*d*	*t*	*w*	*s*	*l*	*dr*	*ds*	*ld*	*t'*	*ws*	*ys*
Type I	3.9	0.3	0.34	0.5	12.5	2.65	2.5	1.1	2	7	-	0.5	1.5
Type II	3.9	0.3	0.34	1.1	14.5	1.68	0.5	1.1	1.9	3	0.43	-	-
Type III	3.9	0.3	0.34	0.8	12.5	1.68	0.5	1.2	2.2	1.1	-	-	-
Type IV	3.9	0.3	0.34	1.1	14.5	1.68	0.5	1.1	1.9	12	0.33	-	-

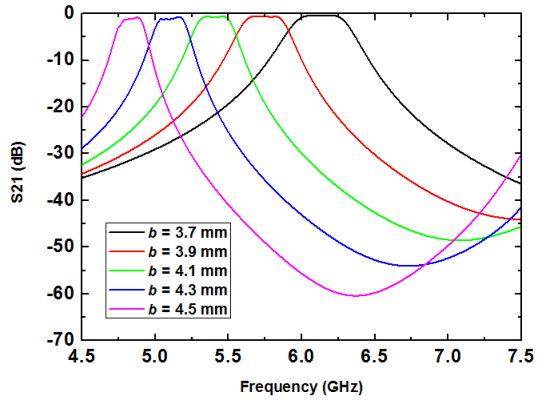

(a)

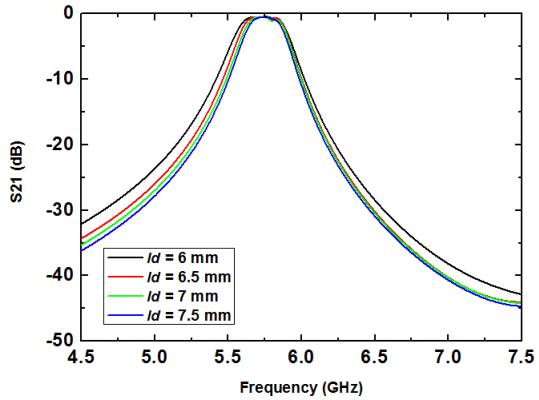

(b)

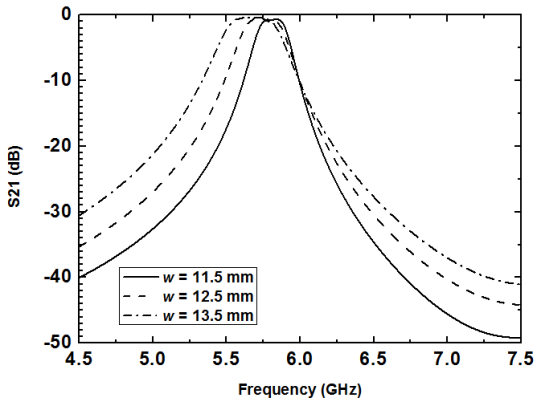

(c)

Figure 5.9 Simulated S_{21} of the filter with the type I unit cell with different: (a) length of the BC-CSRR (*b*), (b) length of the evanescent-mode SIW (*ld*), and (c) width of the SIW (*w*)

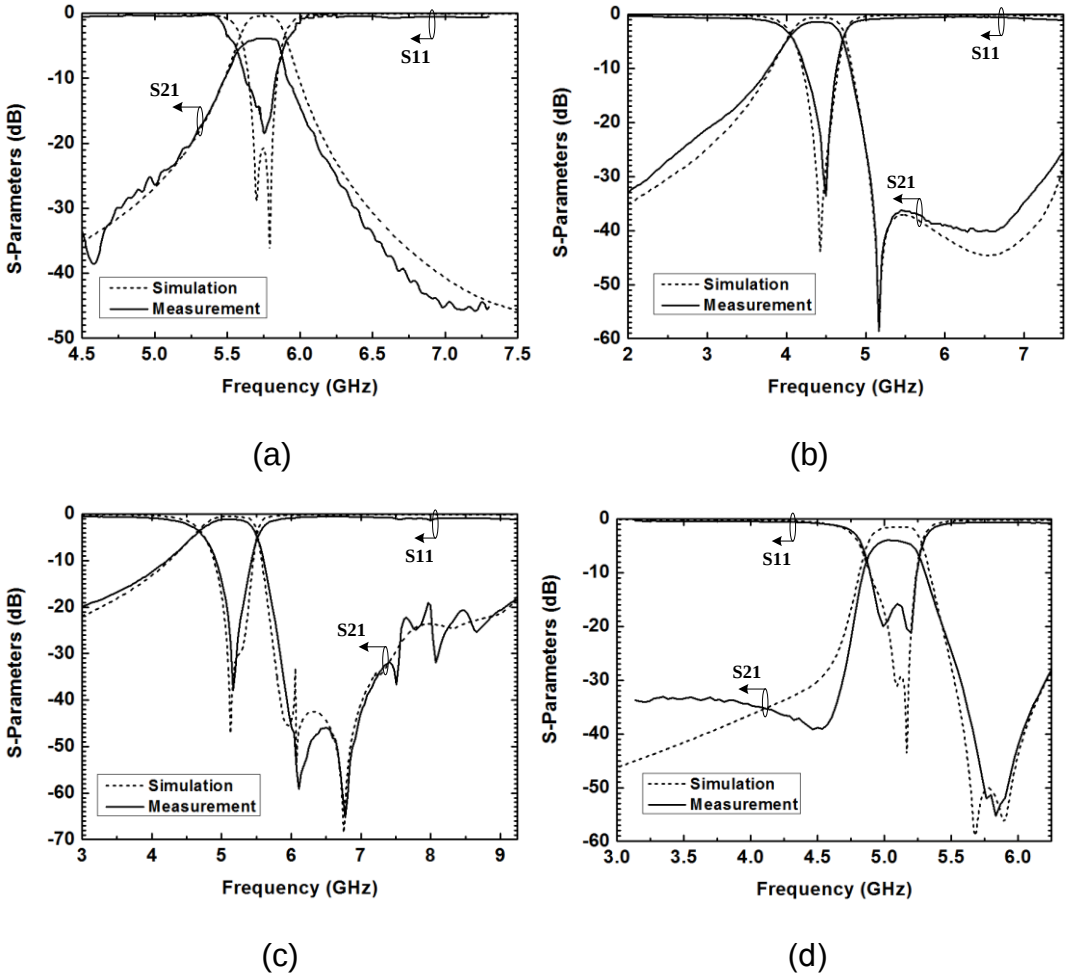

Figure 5.10 Simulated and measured frequency responses of the filters base on: (a) type I unit cells, (b) type II unit cells, (c) type III unit cells and (d) type IV unit cells

5.3 SIW Filters with Face-to-Face Oriented BC-CSRR Pairs

In this section, an improved form of the face-to-face oriented BC-CSRR pair is proposed and investigated to form a SIW bandpass filter with enhanced stopband performance. The unit cell of the SIW with the conventional face-to-face aligned BC-CSRR resonator pair is first investigated. It is shown that, by removing the metal strip between the two back-to-back rings of the BC-CSRR pair, the spurious passband might be inhibited and a very substantial improvement in stop-band rejection can be achieved. Based on this analysis, a novel unit cell of the SIW with a modified BC-CSRR pair is then proposed to improve the stopband performance. SIW bandpass filters with the resonator pairs are designed and the measured results are compared. It is shown that the SIW filter with modified BC-CSRR pairs shows improved stopband performance in comparison to that with conventional BC-CSRR pairs.

5.3.1 The Face-to-Face Oriented SIW BC-CSRR Resonator Pair

The unit cell of SIW combined with face-to-face oriented BC-CSRRs is shown in Figure 5.11. As depicted in Figure 5.11(b)-(c), a pair of BC-CSRRs aligned face to face is employed and etched on the SIW top and bottom metal planes; a microstrip feed line is adopted to excite the SIW cavity and an inset transition is used to better match the microstrip line and the SIW.

The transmission response of the proposed SIW BC-CSRR unit cell simulated by the HFSS^{TM} is shown in Figure 5.11(d), compared with that of the initial SIW. It can be seen that the resonant frequency is located at 4.03 GHz and it is below the cutoff frequency of the original SIW. However, in the upper stopband, a spurious passband appears at around 9.37 GHz, which eliminates the out-of-band suppression and limits the usefulness of the structure.

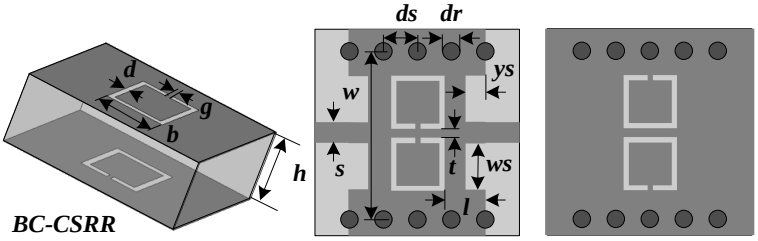

(a) (b) (c)

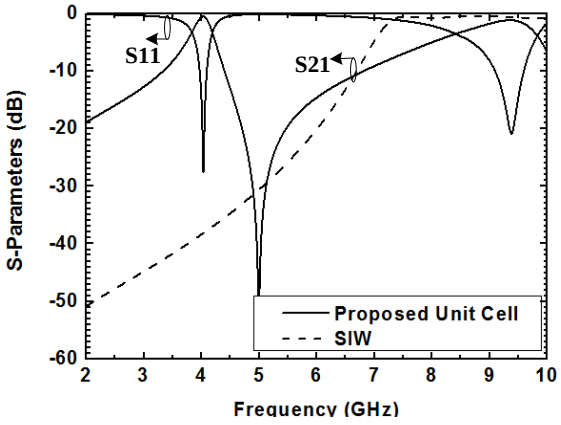

(d)

Figure 5.11 (a) Configuration of the BC-CSRR. (b) Top view of the unit cell of the SIW with face-to-face oriented BC-CSRRs. (c) Bottom view of the unit cell. (d) Simulated frequency responses of the original SIW and the proposed unit cell (with parameters ε_r = 3.48, h = 0.762 mm, b = 3.9 mm, g = 0.3 mm, d = 0.34 mm, t = 0.5 mm, w = 12.5 mm, s = 1.68 mm, ws= 3 mm, ys = 2 mm, l = 0.5 mm, dr = 1.2 mm, ds = 2.2 mm)

To better understand the spurious response, the electromagnetic field distribution of the unit cell at 9.37 GHz has been investigated. As shown in Figure 5.12, both of the electric and magnetic field are mainly distributed on the bottom rings and especially on the middle metal strip line between these two bottom rings. This indicates that the field propagation at 9.37 GHz strongly depends on the middle metal strip line on the bottom. On the contrary, for the fundamental passband at 4.03 GHz as depicted in Figure 5.13, the electromagnetic field of the top rings is much stronger than that of the bottom rings and only a weak electromagnetic field is distributed on the bottom middle metal strip. This means that the rings on the top play an important role in the field propagation at 4.03 GHz, while the middle metal strip line between the two bottom rings, which is critical for the field propagation of the spurious passband at 9.37 GHz, has only a small effect on the primary passband. Therefore, it is expected that the spurious passband might be suppressed by removing the middle metal strip line between the two bottom rings, with the primary passband only receiving a limited effect.

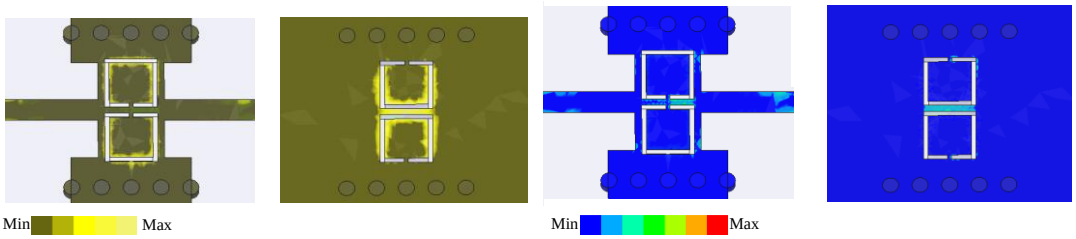

(a) (b) (c) (d)

Figure 5.12 Field distribution of the proposed unit cell at 9.37 GHz: (a) top view of the electric field distribution; (b) bottom view of the electric field distribution; (c) top view of the magnetic field distribution, and (d) bottom view of the magnetic field distribution

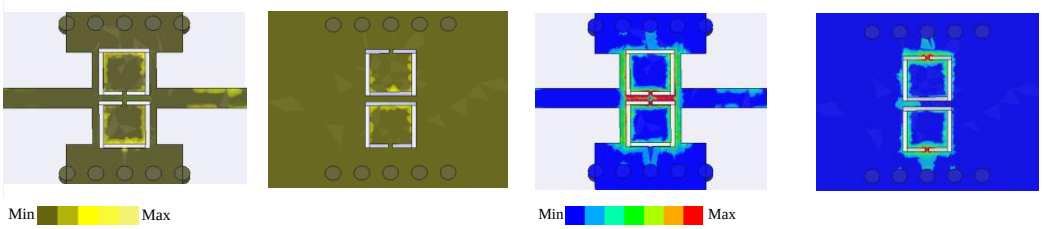

(a) (b) (c) (d)

Figure 5.13 Field distribution of the proposed unit cell at 4.03 GHz: (a) top view of the electric field distribution; (b) bottom view of the electric field distribution; (c) top view of the magnetic field distribution, and (d) bottom view of the magnetic field distribution

5.3.2 Modified SIW BC-CSRR Resonator Pairs with Improved Spurious Suppression

Based on the discussion above, a modified SIW BC-CSRR resonator pair is proposed to improve the spurious suppression by removing the middle metal strip line between the two rings of the BC-CSRR on the bottom broadwall of the SIW. Figure 5.14 shows the configuration of the new unit cell, where the middle metal strip line between the two rings on the bottom of the SIW is removed and these two rings are united along the common side. The simulated transmission response of the modified unit cell is shown in Figure 5.14(c). Like the frequency response of the original unit cell, a passband is observed, now with the centre frequency at 4.2 GHz. As expected, the spurious passband of the original unit cell at 9.37 GHz is suppressed and a broad stopband with an enhanced out-of-band rejection is achieved for the modified unit cell.

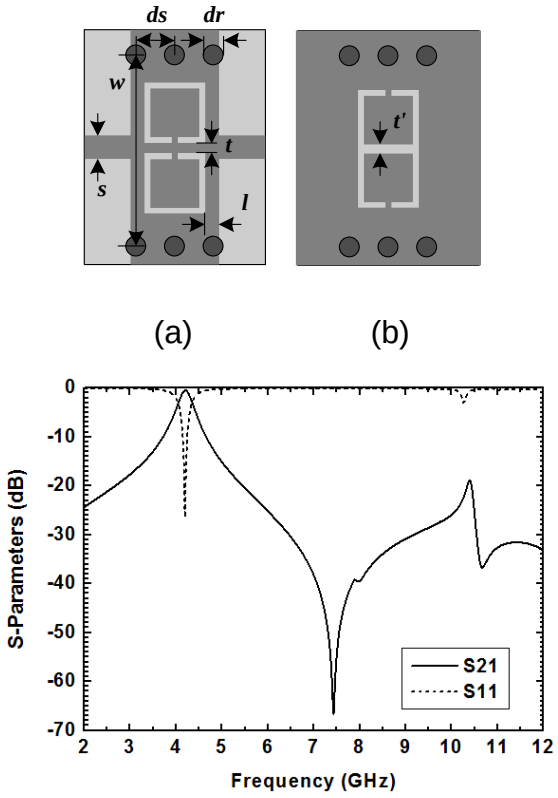

Figure 5.14 Configuration of the modified unit cell: (a) top view; (b) bottom view; and (c) simulated transmission responses (with parameters: ε_r = 3.48, h = 0.762 mm, b = 3.9 mm, g = 0.3 mm, d = 0.34 mm, t = 0.5 mm, t' = 0.34 mm, w = 12.5 mm, s = 1.68 mm, l = 0.5 mm, dr = 1.2 mm, ds = 2.2 mm)

5.3.3 SIW Bandpass Filters with the Face-to-Face Oriented BC-CSRR Pairs

Based on the initial face-to-face oriented BC-CSRR resonator pair (see Figure 5.11) and the modified resonators (see Figure 5.14), bandpass filters were designed and optimized with HFSS™ following a similar procedure to that used in the design of SIW filters with side-by-side oriented BC-CSRR pairs in section 5.2.3. Rogers RO 4350 substrate with ε_r = 3.48 and a thickness of 0.762 mm was used to fabricate all of the filters. The filters were fabricated using a standard PCB etching process. They were measured with an Agilent E8363A network analyzer.

Figure 5.15 shows the layout and photograph of a two-section SIW bandpass filter based on the original unit cell. Two completely identical unit cells coupled by an evanescent-mode SIW section are employed. The distance between two resonators can be tuned to obtain the required coupling. Figure 5.16(a) shows the simulated and measured transmission response of the filter over the 3 to 6 GHz band. The measured centre frequency is 4.15 GHz. The measured 3 dB bandwidth is 0.25 GHz. The insertion loss is approximately 2.8 dB including the feed lines and SMA connectors. Figure 5.16(b) shows the measured frequency response over a wide band. It can be seen that the measured stopband rejection is better than 20 dB from 4.46 GHz to 6.88 GHz. Unfortunately, a wide band of unwanted transmission appears between 7.5 GHz to 10 GHz, which severely limits the usefulness of the structure.

Figure 5.17 shows the photograph and the layout of a second-order filter based on the new unit cell. Here, the two united back-to-back rings are etched on the top broadwall to better protect the integrity of the ground plane. The simulated and measured transmission responses of the filter over the 3 to 6 GHz band are plotted in Figure 5.18(a). The measured centre frequency and 3 dB bandwidth are 4.46 and 0.25 GHz, respectively. The measured insertion loss is approximately 1.1 dB including the feed lines and SMA connectors. Figure 5.18(b) shows the measured frequency response over a wide band. It can be seen that the measured stopband extends from 5.05 GHz to 15 GHz with better than 20 dB rejection. By comparing the results shown in Figure 5.16(b) and Figure 5.18(b), it can be seen that the filter with modified BC-CSRR pairs shows enhanced spurious suppression and wider rejection bandwidth.

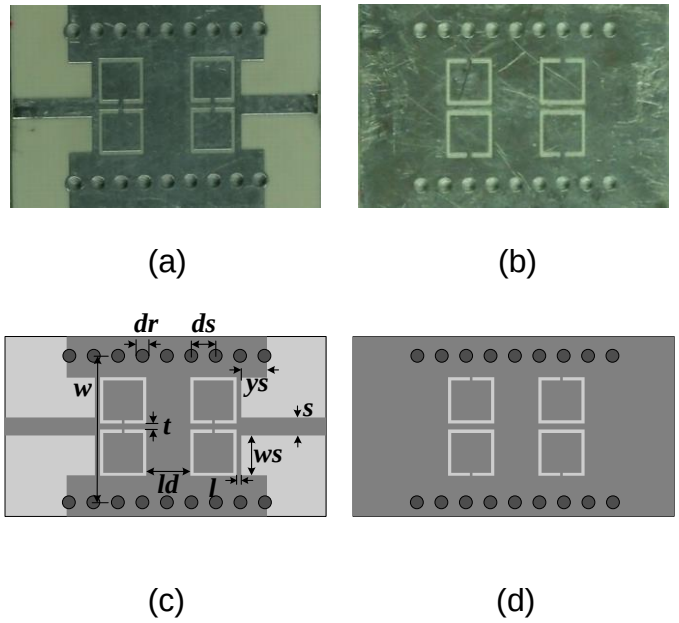

(a) (b)

(c) (d)

Figure 5.15 (a) Photograph of the top of the filter base on the face-to-face aligned SIW BC-CSRR resonator pair. (b) Photograph of the bottom of the filter. (c) Top view of the layout. (d) Bottom view of the layout (with parameters *b* = 3.9 mm, *g* = 0.3mm, *d* = 0.34 mm, *t* = 0.5 mm, *w* = 13 mm, *s* =1.68 mm, *ys* = 2 mm, *ws* = 3 mm, *l* = 0.5 mm, *dr* = 1.1 mm, *ds* = 2 mm, *ld* = 4 mm)

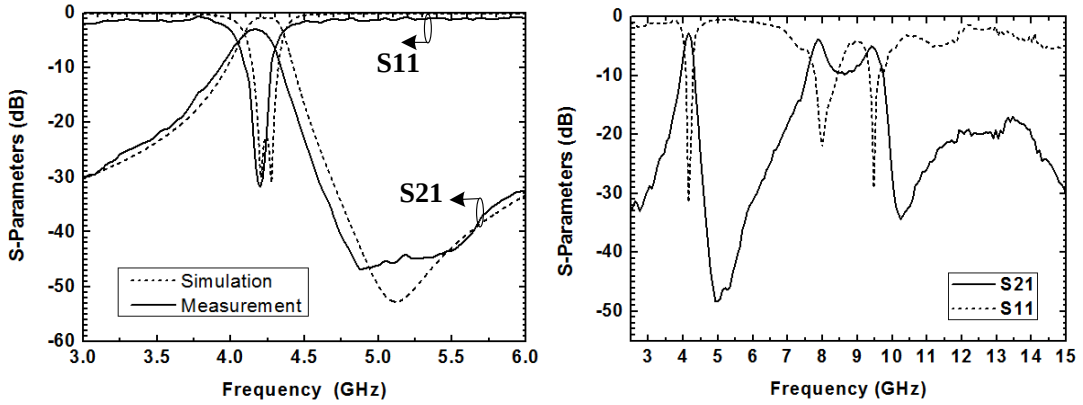

(a) (b)

Figure 5.16 Simulated and measured results in the 3 to 6 GHz band. (b) Wideband measurement result

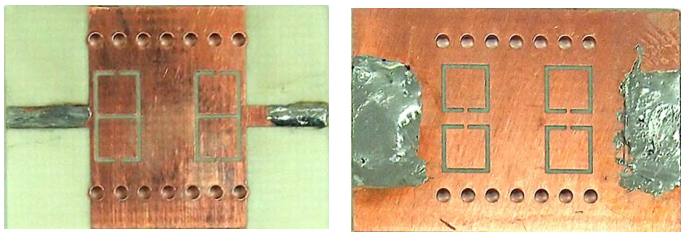

(a) (b)

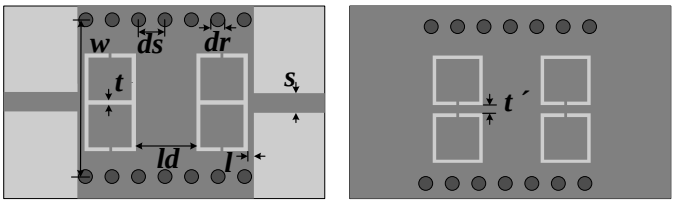

(c) (d)

Figure 5.17 (a) Photograph of the top of the filter base on the modified unit cell. (b) Photograph of the bottom of the filter. (c) Top view of the layout. (d) Bottom view of the layout (with parameters h = 0.762 mm, b = 3.9 mm, g = 0.3mm, d = 0.34 mm, t = 0.34 mm, t' = 1 mm, w = 12.5 mm, s =1.68 mm, l = 0.5 mm, dr = 1.1 mm, ds = 2 mm, ld = 4.5 mm)

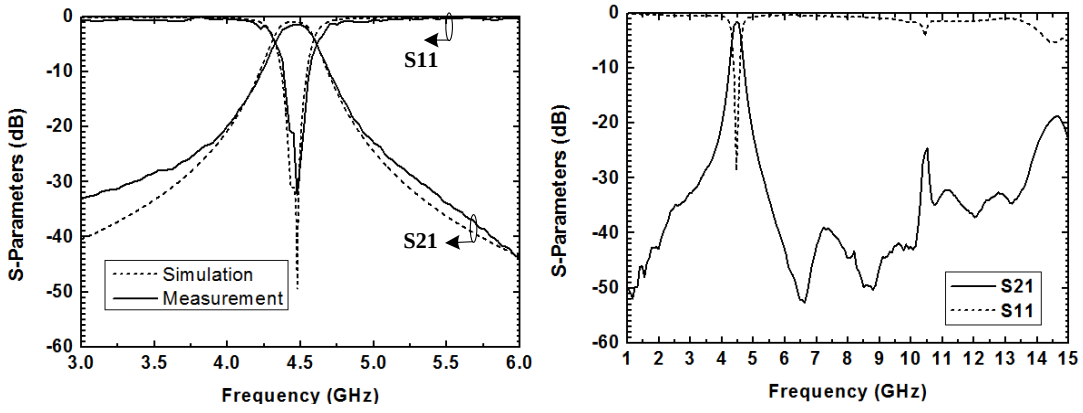

(a) (b)

Figure 5.18 (a) Simulated and measured results in the 3 to 6 GHz band. (b) Wideband measurement result

5.4 HMSIW Filters with Capacitively-Loaded Complementary Single Split Ring Resonators (CSSRRs)

In this section, novel compact half-mode substrate integrated waveguide (HMSIW) filter with capacitively loaded complementary single split ring resonators (CSSRRs) are presented. The configuration of the HMSIW with the capacitively loaded CSSRR is proposed. It is shown that the proposed structure demonstrates lower resonant frequency and improved miniaturiztion performance compared to the HMSIW with conventional CSSRRs due to the additional capacitance generated by the foil between the inner metal disk and the ground plane of the CSSRR. Even lower resonant frequency and better miniaturization effect can be achieved conveniently by increasing the dimensions of the foil properly or using thin dielectric substrate. The equivalent circuit model for the proposed element is derived. A prototype of the second-order bandpass filter with the proposed element, operating at 4.92 GHz, is designed and fabricated. Excellent agreement is achieved between the simulation and the measurement.

5.4.1 Configuration of the Capacitively-Loaded CSSRR

The configuration of the conventional CSSRR and its equivalent circuit model are shown in Figure 5.19(a). Similar to the classic EC-CSRR, the CSSRR can be modeled as a *LC* resonant tank driven by external electric fields [51]. As shown in Figure 5.19(a), *L* represents the total inductance of the CSSRR, and *C* is the total capacitance. The configuration of the capacitively-loaded CSSRR is depicted in Figure 5.19(b). It consists of two layers. The lower layer is the conventional CSSRR. On the top surface, a conductor layer which overlaps the ground plane of the CSSRR is connected to the centre of the inner metal disk of the CSSRR through a metalized via. The overlap region between the ground plane and the top conductor layer introduces an additional capacitance, therefore, compared to the conventional CSSRR, the capacitively-loaded CSSRR is capable of achieving a lower resonant frequency but with no in-plane size increment. The simplified equivalent circuit model for the capacitively-loaded structure is shown in Figure 5.19(b), where *L* stands for the total inductance; *C* represents the slot capacitance between the inner metal disk and the ground plane of the CSSRR, and C_1 represents the additional capacitance between the conductor on the upper layer and the ground plane of the CSSRR.

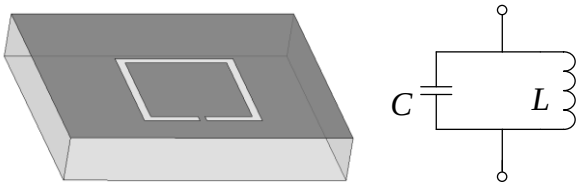

(a)

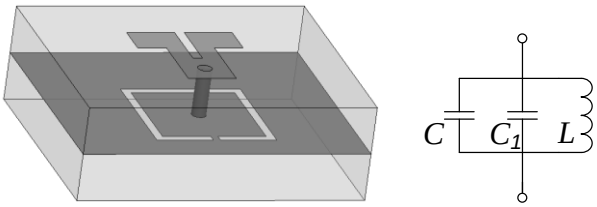

(b)

Figure 5.19 (a) Configuration of the conventional CSSRR and the equivalent circuit model. (b) Configuration of the modified CSSRR and the equivalent circuit model. Grey shading represents the metallization

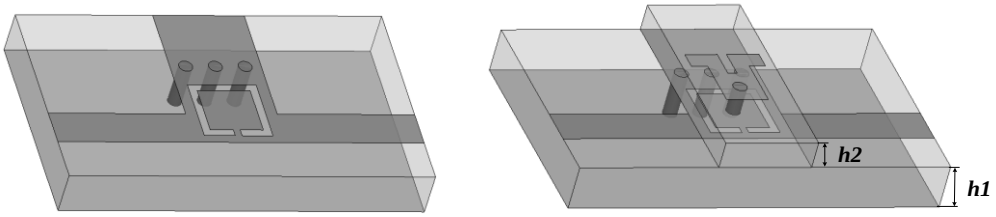

(a) (b)

Figure 5.20 (a) Configuration of the element of the HMSIW with the conventional CSSRR. (b) Configuration of the element of the HMSIW with the capacitively-loaded CSSRR

5.4.2 Configuration of the HMSIW with the Capacitively-Loaded CSSRR

Figure 5.20(a) shows the configuration of the HMSIW with the conventional CSSRR. The CSSRR is etched on the top broadwall of the HMSIW. The microstrip feed line is employed to excite the HMSIW with the CSSRR. Since the electric field of the main mode of the HMSIW is perpendicular to the top and bottom broadwalls, it guarantees that the CSSRR which requires axial electric excitation is properly excited. Based on this configuration, the element of the HMSIW with the capacitively-loaded CSSRR is proposed. As shown in Figure 5.20(b), an extra layer is added which is used to enhance the total capacitance of the CSSRR by having a conductor that is connected

to the centre of the inner metal disk of the CSSRR through a metal via and overlaps the ground plane.

A prototype of the proposed element has been designed with the HFSS™ and fabricated on Rogers RO 4350 with dielectric constant ε_r = 3.48. Figure 5.21 shows the photograph and layout of the proposed element. The parameters are as follows: *h1* = 0.8 mm, *h2* = 0.3 mm, *b* = 3 mm, *g* = 0.3mm, *d* = 0.34 mm, *t* = 0.4 mm, *w* = 4.5 mm, *s* =1.68 mm, *l* = 0.4 mm, *dr* = 1.1 mm, *ds* = 1.9 mm, *wt* = 0.4 mm, *ws* = 0.8 mm, *wc* = 1.4 mm, *wy* = 1.8 mm, *wx* = 2.3 mm. The simulated and measured frequency responses are shown in Figure 5.22. It can be seen that measured resonant frequency is 4.87 GHz, with a transmission zero introduced at 6.09 GHz. Good agreement has been achieved between the simulation and the measurement. For comparison, the element of the HMSIW with the conventional CSSRR (see Figure 5.20(a)) with the dimensions identical to the lower layer of the HMSIW with the capacitively-loaded CSSRR was also investigated. The simulated frequency responses are plotted in Figure 5.22, compared with that of the proposed element. It can be seen that the resonant frequency of the HMSIW with the conventional CSSRR is 7.23 GHz, which is much higher than that with the capacitively-loaded CSSRR.

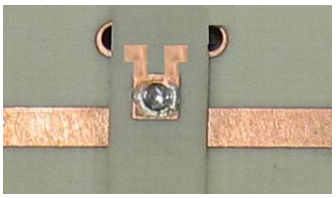

(a)

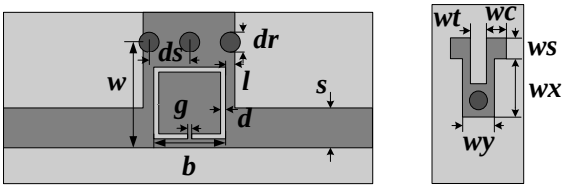

(b) (c)

Figure 5.21 (a) Photograph of the fabricated element of the HMSIW with the capacitively-loaded CSSRR. (b) Layout of the lower layer of the element. (c) Layout of the upper layer of the element. Grey shading represents the metallization

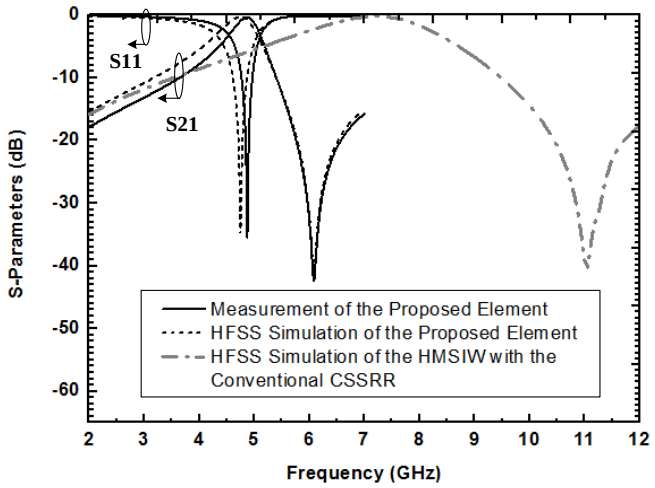

Figure 5.22 Simulated and measured results of the element of the HMSIW with the capacitively-loaded CSSRR, compared with the HMSIW with the conventional CSSRR

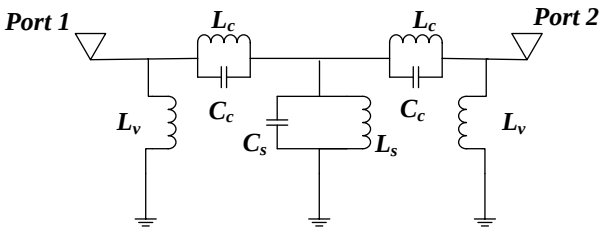

Figure 5.23 Equivalent circuit model of the element of the HMSIW with the capacitively-loaded CSSRR

To better understand the response of the proposed element, the simplified equivalent circuit model has been derived. As shown in Figure 5.23, the metallic vias forming the HMSIW is modelled as L_v; the capacitively-loaded CSSRR is modeled as a resonant tank with the inductance L_s and the capacitance C_s; the magnetic coupling between the HMSIW and the capacitively-loaded CSSRR is represented by L_c. It is mainly through the split of the ring between the HMSIW and the CSSRR. The capacitive coupling is denoted by C_c, and it is mainly through the slot coupling between the HMSIW and the CSSRR. Moreover, this equivalent circuit model can also be applied to the element of the HMSIW with the conventional CSSRR (see Figure 5.20(a)). In this case, L_v represents the metal vias forming the HMSIW; L_s and C_s stand for the total inductance and capacitance of the conventional CSSRR, respectively; L_c and C_c represent the inductive and capacitive coupling between the HMSIW and the CSSRR, respectively. From the circuit model, it can be seen that a transmission zero is generated:

$$f_Z = \frac{1}{2\pi\sqrt{L_S C_S}} \tag{5-7}$$

The simulated frequency responses of the proposed element and the HMSIW with the conventional CSSRR from the equivalent circuit model are shown in Figure 5.24(a) and Figure 5.24(b), respectively, compared with that from the HFSS™. Excellent agreement has been achieved. For the proposed element, the parameters of the circuit model are: L_v = 2.5 nH, L_c = 0.91 nH, C_c = 0.75 pF, L_s = 1.68 nH, C_s = 1.3 pF; for the case of the HMSIW with conventional CSRRs, the parameters are: L_v = 2.4 nH, L_c = 0.6 nH, C_c = 0.35 pF, L_s = 1.755 nH, C_s = 0.753 pF. By comparing the value of the lumped element of the circuit model, it can be seen that the proposed element has a larger capacitance, C_s, which further verifies that enhanced capacitance is obtained for the element with the capacitively-loaded CSSRR.

The loading capacitance between the conductor on the upper layer and the ground plane of the CSSRR can be tuned conveniently by changing the layout of the conductor and the dielectric substrate parameters. Figure 5.25 presents the simulated results with different thickness of the upper layer, *h2*. It can be seen that the resonant frequency reduces significantly when *h2* becomes smaller, due to the increase of the capacitance between the

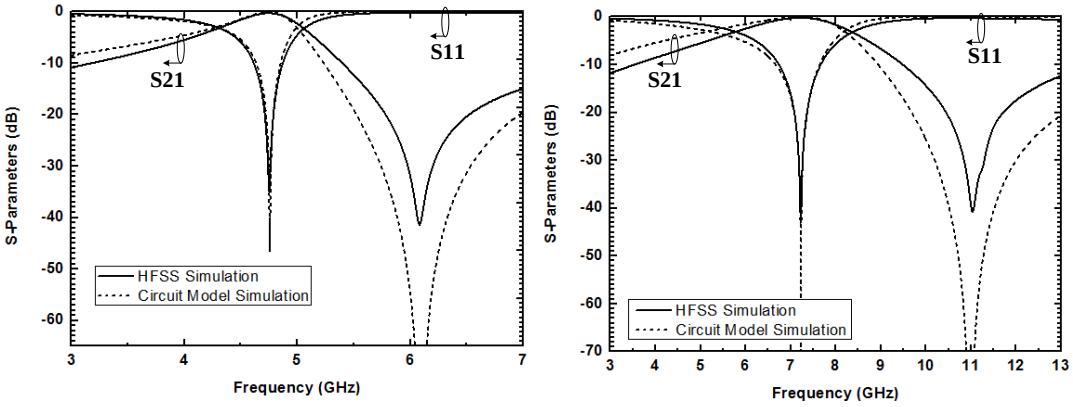

Figure 5.24 (a) Circuit model simulation of the HMSIW with the capacitively-loaded CSSRR. (b) Circuit model simulation of the HMSIW with the conventional CSSRR

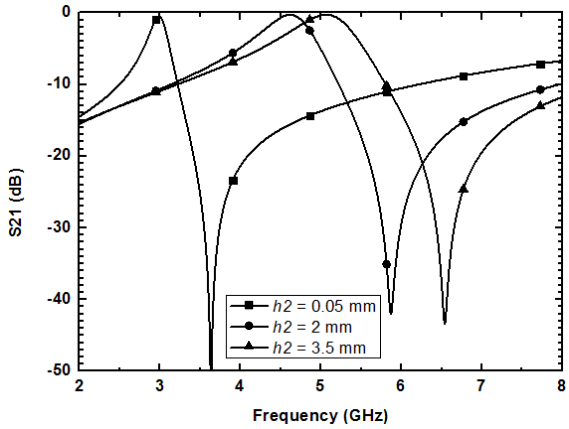

Figure 5.25 Simulated frequency responses with different thickness of the dielectric substrate of the upper layer, *h2*

conductor and the ground plane of the CSSRR. This indicates that even more compact sizes could be achieved conveniently by using thin dielectric substrate for the upper layer. Moreover, a smaller physical size can also be achieved by increasing the length and the width of the conductor overlap appropriately.

5.4.3 HMSIW Bandpass Filter with the Capacitively-Loaded CSSRR

Based on the element of the HMSIW with the capacitively-loaded CSSRR shown in Figure 5.20(b), a second-order bandpass filter has been designed and fabricated. Figure 5.26 shows the configuration, the photograph and the layout of the proposed filter. Two identical capacitively-loaded CSSRRs are employed in the design. The distance between adjacent resonators can be changed to tune the coupling. The parameters are as follows: *h1* = 0.8 mm, *h2* = 0.3 mm, *b* = 3 mm, *g* = 0.3mm, *d* = 0.34 mm, *t* = 0.5 mm, *w* = 4.5 mm, *s* =1.68 mm, *l* = 0.4 mm, *dr* = 1.1 mm, *ds* = 2 mm, *ld* = 2.6 mm, *wt* = 0.4 mm, *ws* = 0.8 mm, *wc* = 2.2 mm, *wy* = 1.8 mm, *wd* = 5.6 mm, *wx* = 2.4 mm. The simulated results with HFSS^{TM} and the measured transmission responses are shown in Figure 5.27. It can be seen that the measurement agrees well with the simulation. The measured centre frequency and 3 dB bandwidth are 4.92 and 0.6 GHz, respectively. The measured insertion loss is 0.8 dB including the feed lines and SMA connectors. The measured in-band return loss is better than 20 dB. The total size of the filter is only 9.8 mm × 7mm (0.17 λ_0 × 0.115 λ_0, where λ_0 is the free-space wavelength of the centre frequency) without the feed line, which is very compact.

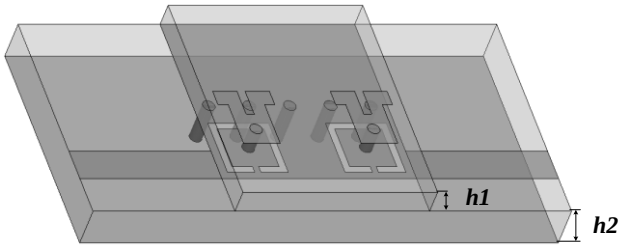

(a)

(b)

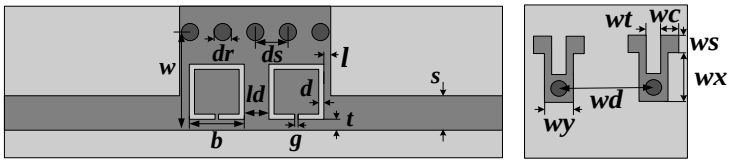

(c) (d)

Figure 5.26 (a) Configuration of the proposed HMSIW filter with capacitively-loaded CSSRRs. (b) Photograph of the fabricated filter. (c) Layout of the upper layer of the filter. (d) Layout of the lower layer of the filter. Grey shading represents the metallization

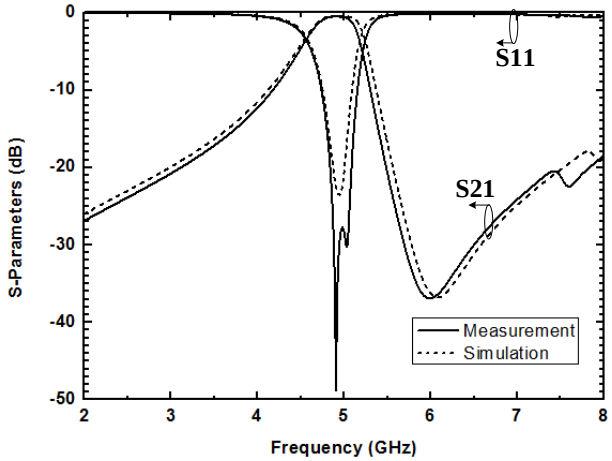

Figure 5.27 Simulated and measured transmission responses of the HMSIW bandpass filter with capacitively-loaded CSSRRs

5.5 Summary

In this chapter the design of SIW and HMSIW filters with the broadside-coupled complementary split ring resonator and the capacitively loaded complementary single split ring resonator have been presented.

In section 5.2 and 5.3, novel bandpass SIW filters based on the BC-CSRR resonator pairs have been presented. Four distinct types of SIW BC-CSRR resonator structures have been introduced and compared by changing the orientation of the rings on the upper broadwall; a modified unit cell of SIW with face-to-face oriented BC-CSRR pairs has been proposed to improve the stopband performance. Bandpass filters have been designed and fabricated based on these proposed resonators. It is shown that these filters operate below the cutoff frequency of the SIW and are therefore compact in size. They are also easy to fabricate and integrate with other electric circuits, giving great potential for use in low-cost microwave circuits.

In section 5.4, a compact HMSIW filter with a capacitively-loaded CSSRR is presented. The element of the HMSIW with the capacitively-loaded CSSRR is investigated. It is shown that the proposed element demonstrates a lower resonant frequency and greater miniaturization compared to the HMSIW with conventional CSSRR, due to the additional capacitance introduced by the extra conductor layer overlapping the inner metal disk and the ground plane of the CSSRR. Furthermore, by increasing the overlap area or decreasing the thickness of the dielectric substrate appropriately, even larger capacitance and lower frequency can be achieved. The equivalent circuit model is derived. A prototype of bandpass filters with the proposed element operating at 4.92 GHz is designed and fabricated. It is shown that the proposed filter has the advantages of compact size, low losses and good selectivity. The total size of the filter without the feed line is only 9.8 mm × 7mm ($0.17\ \lambda_0 \times 0.115\ \lambda_0$).

Chapter 6
SIW Bandpass Filter with Cascaded Complementary Electric-LC (CCELC) Resonators

6.1 Introduction

As have been discussed in Chapter 2, when a CSRR is etched on the top or bottom broadwalls of the SIW, a narrow stopband could be generated in the SIW passband as the CSRR introduces negative effective permittivity around its resonant frequency [48, 129]. This stopband response of the CSRR has been applied to the design of SIW bandpass filters by combing the high-pass band of the SIW with the stopband of the CSRR [48]. However, due to the narrow bandwidth of the CSRR, this type of filters is found to have a relatively narrow spurious-free band, and the out-of-band suppression of these filters still needs to improve.

Recently, a new structure termed the "*complementary electric LC (CELC) resonator*" has been proposed and applied to the design of microstrip filters with enhanced stopband performance [42, 118, 130]. It is shown that a broad stopband can be generated when the CELC resonator is etched on the ground plane of the microstrip [42]. Therefore, the CELC resonator has great potential to realise bandpass filters with excellent out-of-band performance.

In this chapter, by etching the CELC resonator on the top broadwall of the SIW, the unit cell of the SIW with the CELC resonator is proposed and investigated. It is demonstrated that the SIW with the CELC resonator exhibits a better filtering response and a deeper stopband rejection compared to SIW with the conventional CSRR. Based on the configuration of the CELC resonator, a cascaded CELC (CCELC) resonator is proposed to further improve the stopband suppression by combining two CELC resonators together. In comparison to the CELC resonator, the proposed CCELC resonator exhibits an enhanced stopband performance with two transmission zeroes. A SIW bandpass filter based on the CCELC resonator is designed and fabricated by using the high-pass response of the SIW and the stopband of the CCELC resonator. The proposed filter shows a good out-of-band performance with a wide stopband range and a sharp upper transition between the passband and stopband.

6.2 SIW with the Cascaded CELC Resonator

6.2.1 SIW with the CELC Resonator

The configuration of the CELC resonator is shown in Figure 6.1(a), where two identical back-to-back complementary single split ring resonators comprise the CELC resonator. The CELC resonator is capable of generating negative effective permeability and it can be modelled as a *LC* resonant tank driven by the in-plane magnetic fields normal to the split [118, 130].

The configuration of the unit cell of the SIW with the CELC resonator is shown in Figure 6.1(b), where the CELC resonator is etched on the SIW top broadwalls. A microstrip feed line is used to excite the SIW cavity with the CELC resonator. Since the magnetic field of the main mode in the SIW is parallel to the SIW top and bottom broadwalls and it has the *z*-component, which is orthogonal to the splits of the CELC resonators, the CELC resonator could be driven properly (see Figure 6.1(b)). For comparison, the unit cell of the SIW with the conventional CSRR is also presented in Figure 6.1(c).

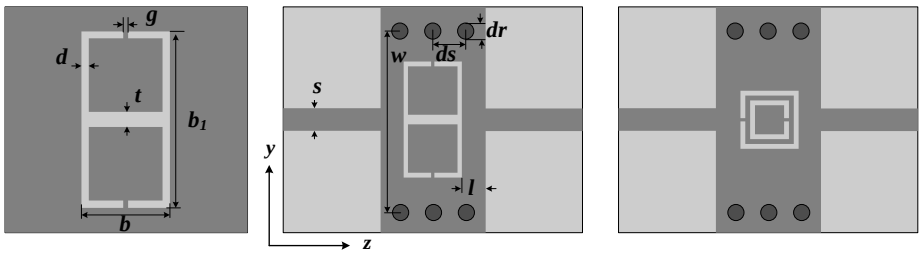

(a) (b) (c)

Figure 6.1 (a) Configuration of the CELC resonator. (b) Configuration of the SIW with the CELC resonator. (c) Configuration of the SIW with the conventional CSRR. Gray shading represents the metallization

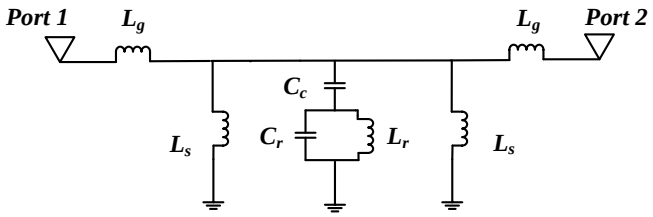

Figure 6.2 Equivalent circuit model for the unit cell of the SIW with the CELC resonator

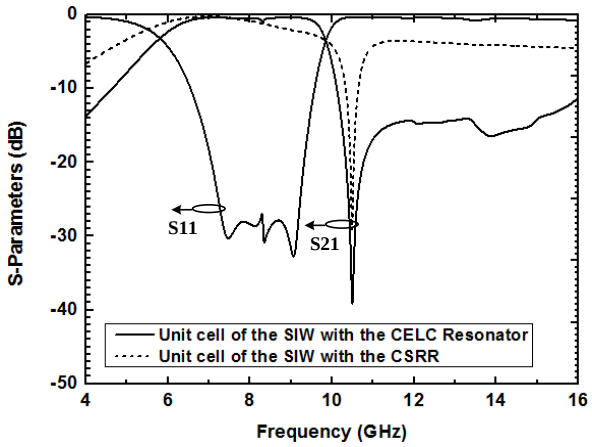

Figure 6.3 HFSS™ simulation of the unit cell of the SIW with the CELC resonator, compared with the unit cell of the SIW with the CSRR (with parameters ε_r = 3.48, h = 0.762 mm, b = 2.05 mm, b_1 = 7.68 mm, g = 0.3 mm, d = 0.34 mm, t = 0.45 mm, w = 14.6 mm, s = 1.68 mm, l = 2.1 mm, dr = 1.1 mm, ds = 2 mm)

The equivalent circuit model for the unit cell of the SIW with the CELC resonator is depicted in Figure 6.2, where L_g indicates the line inductance of the SIW; L_s represents the vias of the SIW; the CELC resonator is modelled as a parallel circuit with the inductance L_r and capacitance C_r; C_c indicates the capacitive coupling between the SIW and the CELC resonator. From the circuit model, it can be seen that a transmission zero is introduced at a frequency given as:

$$f_z = \frac{1}{2\pi\sqrt{L_r\left(C_r + C_c\right)}} \tag{6-1}$$

Figure 6.3 shows the frequency response of the unit cell of the SIW with the CELC resonator simulated with the HFSS™. It can be seen that a good passband response with a transmission zero at 10.25 GHz is achieved. This passband is generated by the combination of the high-pass band of the SIW and the stopband of the CELC resonator. In addition, a broad stopband ranging from 10 GHz to 16 GHz is also obtained. The simulated S_{21} of the unit cell of the SIW with the conventional CSRR (see Figure 6.1(c)), with the parameters of the SIW identical to that of the unit cell of the SIW with the CELC resonator, is also plotted in Figure 6.3 for comparison. It is easy to see that the unit cell of the SIW with the CELC resonator demonstrates a better filtering response with enhanced out-of-band rejection in comparison to that with the CSRR.

6.2.2 SIW with the CCELC Resonator

Based on the configuration of the CELC resonator, a cascaded CELC (CCELC) resonator is proposed to further improve the out-of-band rejection. As depicted in Figure 6.4(a), the CCELC resonator is formed by two identical smaller CELC resonators which are united by a central slot. The configuration of the unit cell of the SIW with the CCELC resonator is presented in Figure 6.4(b), where the CCELC resonator is etched on the SIW top broadwalls.

Based on the equivalent circuit model of the SIW with the CELC resonator in Figure 6.2, the simplified equivalent circuit model for the unit cell of the SIW with the CCELC resonator is derived. As shown in Figure 6.5, L_g represents the line inductance of the SIW, the vias of the SIW is modelled as L_s; considering the symmetric effect of the CCELC resonator, two identical shunt branches with the inductance L_r and capacitance C_r are used to model the two smaller CELC resonators which form the CCELC resonator; the capacitive coupling between the SIW and the smaller CELC resonator is modelled as C_c; the mutual coupling between the two smaller CELC resonators is modelled as a shunt branch denoted by L_m and C_m, where L_m represents the inductive coupling which is mainly through the splits of the two CELC resonators, and C_m indicates the capacitive coupling which is mainly though the central slot. From this circuit model, it is found that two transmission zeroes exist at the frequencies expressed as:

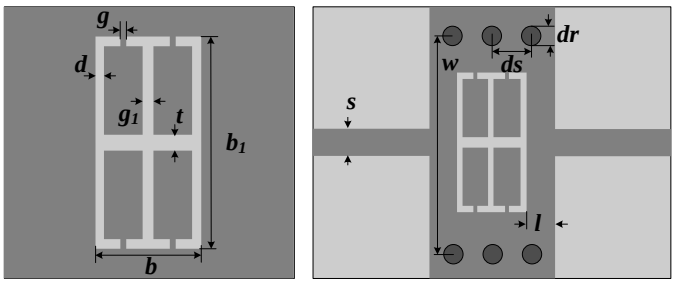

(a) (b)

Figure 6.4 (a) Configuration of the CCELC resonator. (b) Configuration of the SIW with the CCELC resonator. Gray shading represents the metallization

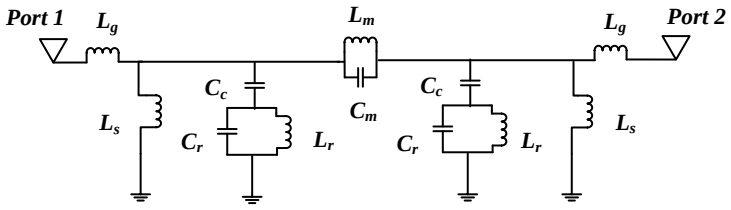

Figure 6.5 Equivalent circuit model for the unit cell of the SIW with the CCELC resonator

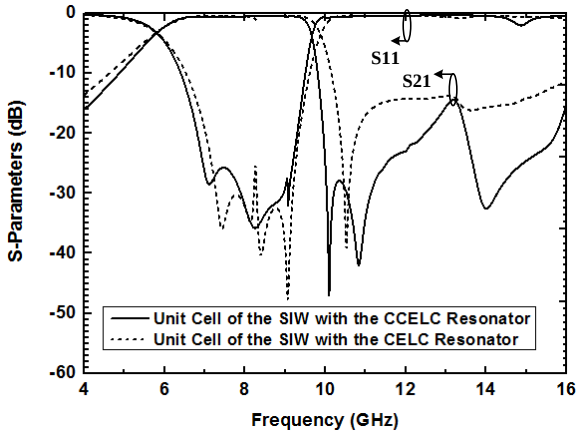

Figure 6.6 HFSS™ simulation of the unit cell of the SIW with the CCELC resonator, compared with the SIW with the CELC shown in Figure 6.1 (with parameters ε_r = 3.48, h = 0.762 mm, b = 3.72 mm, b_1 = 7.75 mm, g = 0.3 mm, g_1 = 0.35 mm, d = 0.34 mm, t = 0.45 mm, w = 14.6 mm, s = 1.68 mm, l = 1.8 mm, dr = 1.1 mm, ds = 2 mm)

$$f_{z1} = \frac{1}{2\pi\sqrt{L_r\left(C_r + C_c\right)}} \tag{6-2}$$

$$f_{z2} = \frac{1}{2\pi\sqrt{L_m C_m}} \tag{6-3}$$

Figure 6.6 shows the transmission response of the unit cell of the SIW with the CCELC resonator simulated with the HFSS™. A good filtering response with a sharp rejection skirt is observed. As expected, two transmission zeroes are also obtained with the zero-transmission frequencies at 10 GHz and 10.95 GHz, respectively. For comparison, the simulated results of the unit cell of the SIW with the CELC resonator (see Figure 6.3) is also plotted in Figure 6.6. It can be seen that the unit cell of the SIW with the CCELC resonator demonstrates an improved stopband performance with two

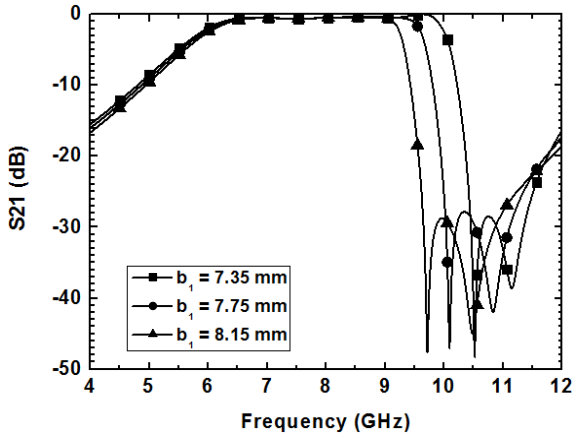

Figure 6.7 Simulated frequency responses with different b_1

transmission zeroes and a sharper rejection skirt compared to the unit cell of the SIW with the CELC resonator.

The passband of the unit cell of the SIW with the CCELC resonator, which is generated by the combination of the high-pass band of the SIW and the stopband of the CCELC resonator, can be tuned conveniently of changing the dimensions of the CCELC resonator, namely, the length (b) and the width (b_1) of the CCELC resonator (see Figure 6.4). Figure 6.7 presents the results by changing the width of the CCELC resonator, b_1. It can be seen that the passband becomes wider with the decrease of b_1. When b_1 reduces, the total capacitance of the CCELC resonator (C_r) and the mutual capacitive coupling that is mainly through the central slot (C_m) become smaller; the corresponding zero-transmission frequencies described by (6-2) and (6-3) are shifted up. The stopband is thus shifted up and the passband is widened.

6.3 SIW Filter with the CCELC Resonator

Based on the unit cell shown in Figure 6.4, a second-order SIW bandpass filter with the CCELC resonator has been designed with the HFSS^{TM}. Rogers 4350 with dielectric constant ε_r = 3.48 and the thickness 0.8 mm was used to fabricate the filter. The layout and the photograph of the fabricated filter are shown in Figure 6.8, where two identical CCELC resonators can be seen etched on the top broadwall of the SIW. The simulated and measured frequency responses are shown in Figure 6.9. Good agreement has been achieved between the simulation and the measurement. The measured centre frequency and the 3 dB bandwidth are 8.46 and 3.43 GHz, respectively. The measured insertion loss is 1.5 dB including the feed lines

and SMA connectors. The measured upper stopband from 9.96 to 15GHz is better than 20 dB. At the falling edge of upper stopband, a very sharp rejection skirt is achieved with the insertion loss decreasing 45 dB between 9.85 to 10.13 GHz.

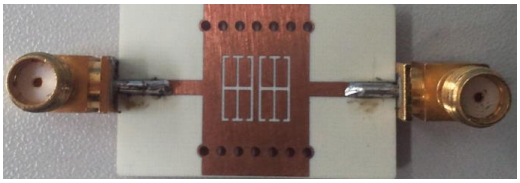

(a)

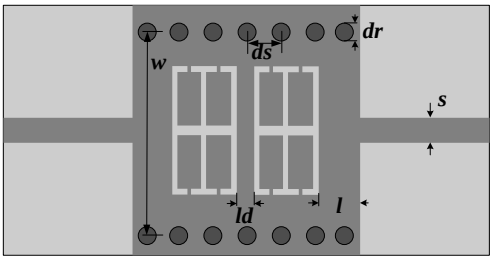

(b)

Figure 6.8 (a) Layout of the second-order SIW bandpass filter with the CCELC resonator. (b) Photograph of the fabricated filter

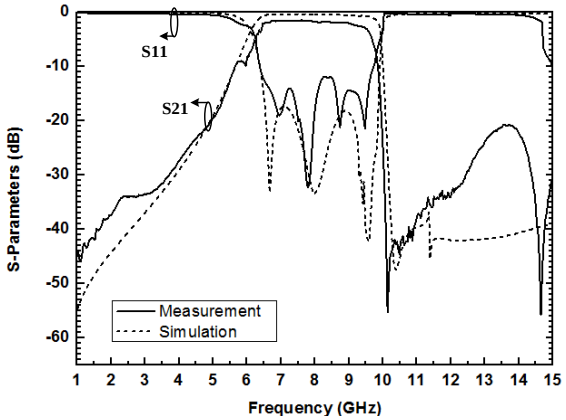

Figure 6.9 Simulated and measured frequency responses of the SIW bandpass filter with the CCELC resonator (with parameters ε_r = 3.48, h = 0.762 mm, b = 3.72 mm, b_1 = 7.7 mm, g = 0.3 mm, g_1 = 0.3 mm, d = 0.34 mm, t = 0.4 mm, w = 14.6 mm, s = 1.68 mm, l = 2.2 mm, ld = 0.6 mm, dr = 1.1 mm, ds = 2 mm)

6.4 Summary

This chapter presents the application of the cascaded complementary electric-LC resonator to the design of a SIW bandpass filter with improved stopband performance. The unit cell of the SIW with the CELC resonator, which shows a better filtering response with enhanced stopband suppression and a wider stopband compared to the SIW with the conventional CSRR, is investigated firstly; a novel CCELC resonator composed of two identical CELC resonators is then proposed to further improve the out-of-band rejection. The unit cell of the SIW with the CCELC resonator exhibits two transmission zeroes and a sharper rejection skirt compared to the SIW with the CELC resonator. Based on the unit cell of the SIW with the CCELC resonator, a second-order bandpass filter has been designed and fabricated. The measurement agrees well with the simulation. The proposed SIW bandpass filter with the CCELC resonator shows a broad stopband with a sharp upper transition between the passband and stopband, and it has the advantages of low loss, low cost, easy fabrication and integration with other electronic circuits.

Chapter 7
Conclusions and Future Work

7.1 Summary

In this work, the design and implementation of SIW filters with improved compactness and performance have been studied. The main body of the work is divided into 4 parts:

1. Development of a design method to convert from a conventional metallic ridge waveguide configuration to the SIW counterpart and design of an evanescent-mode coupled ridge SIW filter with the proposed method.

2. Development of a ridge HMSIW configuration with more compact size than conventional HMSIW and implementation of a compact wideband filter with the modified structure.

3. Development of modified CSRRs (broadside-coupled CSRRs and capacitively loaded CSRRs) with enhanced compactness and performance, and application of the modified structures in the design of improved SIW and HMSIW filters.

4. Application of the CELC resonators in the design of SIW filters with enhanced stopband performance.

7.1.1 Ridge SIW Filters

A bandpass filter employing ridged substrate integrated waveguide resonators is presented in Chapter 3. Instead of assuming the via-fence walls are equivalent to the ideal case, the filter physical dimensions are modified to compensate for their effect. The design and physical realization of an individual ridged SIW resonator is first investigated; the filter is then realised using cascaded resonators coupled through evanescent-mode SIW sections. The design methodology, starting with a ridged waveguide bandpass filter configuration with ideal solid walls and then converting it to the via-hole sidewall SIW counterpart, is described. A multilayer PCB prototype has been fabricated and tested. Good agreement is achieved between the measured results and the simulations.

7.1.2 Ridge Half-Mode SIW Filters

A compact wideband bandpass filter employing a ridged half-mode substrate integrated waveguide (RHMSIW) is presented in Chapter 4. The RHMSIW is proposed by integrating a ridge into the half-mode substrate integrated waveguide. Similar to the ridge SIW, the main effect of the ridge is to introduce a larger capacitance which leads to a lower cutoff frequency and a more compact size compared to the conventional HMSIW. A compact wideband filter based on the RHMSIW is designed, fabricated and tested. Good agreement is achieved between the measured results and the simulations. The proposed RHMSIW bandpass filter shows favourable properties of low loss, good selectivity and compact size, combined with the well-known advantages that SIWs offer for highly integrated circuits and subsystems.

7.1.3 SIW and HMSIW Filters with BC- CSRRs and Capacitively-Loaded CSSRRs

Bandpass SIW filters with the broadside-coupled complementary split ring (BC-CSRR) resonator and modified BC-CSRR resonator pairs have been presented in Chapter 5. Four SIW BC-CSRR resonator structures have been introduced and compared by changing the orientation of the rings on the upper broadwall, and it is shown that, for one particular topology, two poles and two zeroes can be realised with a single unit cell. The equivalent circuits of the four types of resonators have been derived. It is shown that the variation of the orientation of the BC-CSRRs will influence the coupling between BC-CSRRs and thus lead to different frequency responses. Based on these resonators, bandpass filters have been designed and fabricated. These filters operate below the cutoff frequency of the SIW and they are compact and easy to fabricate and integrate with other electric circuits. Furthermore, by analysing the electromagnetic field distribution of the face-to-face oriented BC-CSRR pair and altering the resonator configuration properly, a modified form of BC-CSRRs with improved stopband performance is proposed. A miniaturized SIW bandpass filter is realised with the modified BC-CSRR pair and it is shown that a wider stopband as well as a deeper out-of-band rejection has been achieved for the proposed filter in comparison to its counterpart with conventional BC-CSRR pairs.

Besides the BC-CSRR, a capacitively loaded complementary sing split ring resonator (CSSRR) is proposed and a compact HMSIW bandpass filter is designed with the proposed modified CSSRR. The capacitively loaded

CSSRR is proposed by adding an extra foil between the inner metal disk and the ground plane of the CSSRR. It exhibits a lower resonant frequency and improved miniaturization effect compared to the HMSIW with the conventional CSSRR, due to the additional capacitance introduced by the foil between the inner metal disk and the ground plane of the CSSRR. Even larger capacitance and lower frequency can be achieved conveniently by increasing the dimensions of the foil or decreasing the thickness of the dielectric substrate appropriately. The equivalent circuit model of the proposed element has been derived. A second order bandpass filter with the proposed element, with the centre frequency at 4.92 GHz, has been designed and fabricated. The measurement agrees well with the simulation. The proposed filter has the advantages of compact size, low losses and good selectivity. The total size of the filter without the feed line is only 9.8 mm × 7mm (0.17 λ_0 × 0.115 λ_0). Therefore, it has greatly potential in the design of microwave systems where a small size is critical.

7.1.4 SIW Filters with Complementary Electric-LC Resonators

A SIW bandpass filter based on the cascaded complementary electric-LC (CCELC) resonator is presented in Chapter 6. The unit cell of the SIW with the complementary electric-LC (CELC) resonator is investigated first. It is shown that the SIW with the CELC resonator exhibits a better filtering response and an improved out-of-band performance in comparison to the SIW with the conventional CSRR. By combining two CELC resonators together, a cascaded CELC (CCELC) resonator is proposed to further improve the stopband rejection. A second order SIW bandpass filter with the CCELC resonator is designed by using the high-pass response of the SIW and the stopband of the CCELC resonator. Good agreement is achieved between the measurement and the simulation. The proposed SIW bandpass filter with the CCELC resonator shows a broad rejection band and a very sharp upper transition between the passband and stopband. Moreover, it is low loss, low cost, easy to fabricate and integrate with other microwave circuits.

7.2 Future Work

The outcomes of the work in this thesis highlight the opportunities for novel design and implementation of microwave filters with compact size and high performance using the SIW technology. To achieve further reduction of filter size and improving performance, future work is recommended as described briefly below.

1. Cross-coupled RHMSIW filters with the LTCC technology

Chapter 4 presents compact RHMSIW filters that are physically realised with the multilayer PCB technology. However, it should be noted that this filter configuration can also be implemented with the LTCC (low-temperature co-fired ceramic) technology. The LTCC permits the fabrication of 3-D SIW components, which could add further design flexibility and lead to novel solutions with more compactness and better performance. Therefore, it would be meaningful to further investigate advanced RHMSIW filters with smaller sizes and higher performance by taking advantage of the LTCC technology.

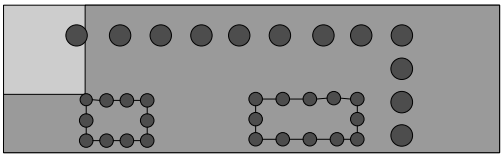

(a)

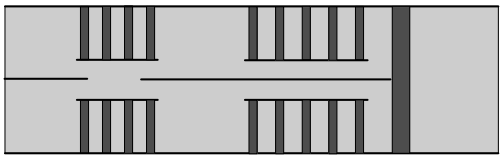

(b)

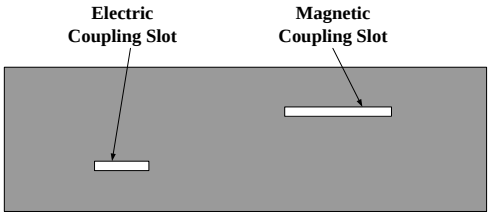

(c)

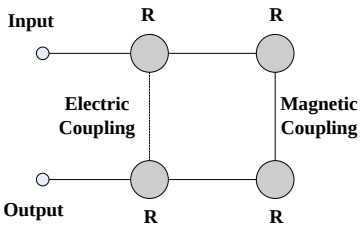

(d)

Figure 7.1 (a) Top view of the cross-coupled RHMSIW filter. (b) Cross-sectional view. (c) Layout of the coupling slot. (d) Topology of the cross coupling

An interesting point that is worth a serious investigation is a type of selectivity filter using cross-coupled RHMSIW structures. As shown in Figure 7.1, the cavities in the same layer are coupled by evanescent mode RHMSIW sections, while the cavities between different layers are coupled by irises placed in the intermediate wall. These coupling windows are opened in the centre, where the electric field is maximum, to provide the electric coupling, or in the side to provide the magnetic coupling through the tangential magnetic field with respect to the iris. Consequently, this filter configuration may be possible to provide a pair of transmission zeros in the rejection band, but with the physical size only half that of conventional cross-coupled ridge SIW filters. For the physical realisation of the filter, it could be implemented with a four-layer LTCC process quite conveniently.

2. Tuneable HMSIW-CSSRR filter

Chapter 5 presents compact HMSIW filters with capacitively loaded CSSRRs. Based on this filter configuration, it may be possible to achieve a tuneable HMSIW CSSRR filter by using the MEMS technology. As shown in Figure 7.2, similar to the capacitively loaded CSSRR, the lower layer of the filter is the HMSIW with the CSSRR; for the upper layer, a conductor layer which contains movable cantilever switches is connected to the centre of the inner metal disk of the CSSRR by laser welding [131]. The position of the switch cantilevers can be adjusted by local thermal laser heating. As a consequence, the frequency response of the filter can be shifted by electrostatic actuation of the switches.

Besides the tuneable CSSRR filter shown in Figure 7.1, in the area of SIW filters with the CSRRs, especially in regards to the application of the new BC-CSRRs and capacitively loaded CSSRRs that were presented in Chapter 5 in this thesis, other designs with SIW CSRR filters integrated into other electronic components such as antennas should provide an interesting research topic. Also, new SIW CSRR filter structures in different technologies to implement negative and positive coupling elements that are required in advanced cross-coupled filters are worth a serious investigation.

3. SIW with low loss for mm-wave systems

The study in this thesis presents the design and implementation of SIW filters with improved compactness and performance. However, it should be noted that these filters work in a relatively low frequency range (lower than 10 GHz). The implementation of SIW components in the mm-wave

frequency range presents a more complex challenge, and there is a clear need to develop novel mm-wave structures with reduced size, improved bandwidth and minimized losses. An interesting point that needs further study is a new type of SIW, which may reduce the dielectric loss of SIWs by embedding an air cavity in SIWs. As shown in Figure 7.3, this SIW is implemented on a three-layer dielectric substrate, with an air cavity embedded in the second layer (Layer 2). Since the dielectric constant of the air (ε_0) is less than that of the substrate (ε_r), the effective dielectric constant of the SIW with air cavity will be reduced and the total dielectric losses might be smaller in comparison to conventional SIWs.

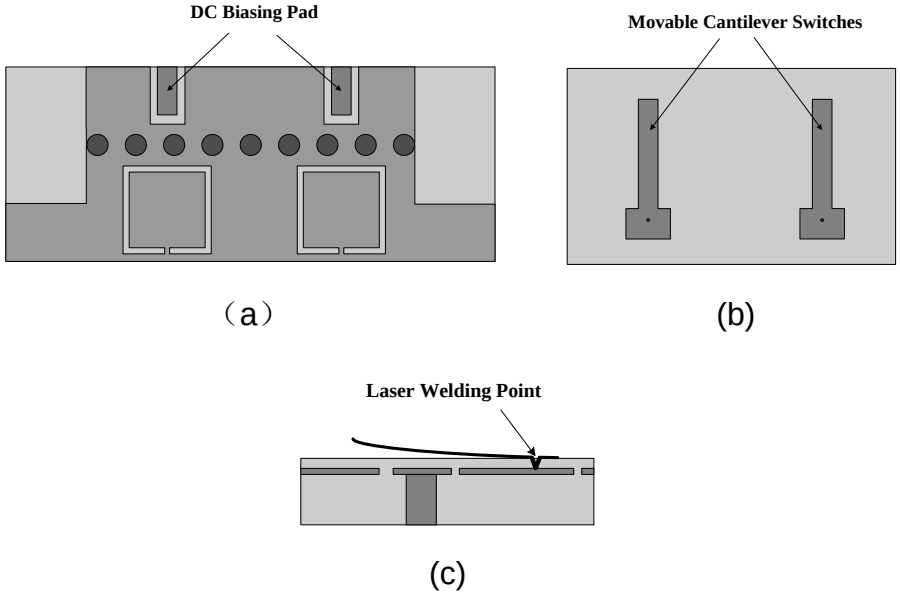

Figure 7.2 (a) Top view of the lower layer of the tuneable HMSIW filter with CSSRR. (b) Top view of the movable cantilever switches. (c) Side view of the filter

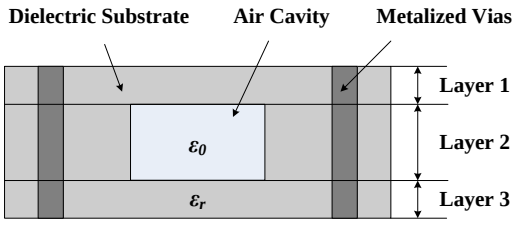

Figure 7.3 Configuration of the SIW with air cavity

List of Publications

Journal Publications

1. Liwen Huang, Ian. D. Robertson and Naichang Yuang, "Compact half-mode substrate integrated waveguide bandpass filter with capacitively loaded complementary single split ring resonators", Microwave and Optical Technology Letters, vol. 55, no. 7, July 2013, pp. 1602-1606

2. Liwen Huang, Ian. D. Robertson, Weiwei Wu and Naichang Yuan, “Substrate integrated waveguide filters with broadside-coupled complementary split ring resonators”, IET Microwaves, Antennas & Propagation, 2013, accepted

Conference Publications

1. Liwen Huang, Ian. D. Robertson, Naichang Yuang and Jinjian Huang, "Novel substrate integrated waveguide filter with broadside-coupled complementary split ring resonators", 2012 IEEE MTT-S International Microwave Symposium Digest, Montreal, Canada, June 2012, pp. 1-3

2. Liwen Huang, Ian. D. Robertson and Naichang Yuang, "Substrate integrated waveguide filter with face-to-face broadside-coupled complementary split ring resonators", 2013 European Microwave Conference, Nuremberg, Germany, Oct. 2013

3. Liwen Huang, Ian. D. Robertson and Naichang Yuang, "Substrate integrated waveguide bandpass filter with novel cascaded complementary electric-LC resonators", 2013 European Microwave Conference, Nuremberg, Germany, Oct. 2013

In Preparation at the Time of Submission:

1. Liwen Huang, Ian. D. Robertson and Naichang Yuang, "Compact wideband halfmode ridge substrate integrated waveguide filter", IEEE Microwave and Wireless Component Letters, 2013, to be submitted

2. Liwen Huang, Ian. D. Robertson and Naichang Yuang, "Modeling and design of a ridge substrate integrated waveguide filter with compensation for the effect of via-fence walls”, IET Microwaves, Antennas & Propagation, 2013, to be submitted

List of References

[1] G. L. Matthaei, L. Young, and E. M. T. Jones, "Microwave filters, impedance matching networks, and coupling structures," *Dedham, MA: Artech House,* 1964.

[2] J. G. Hong, and M. J. Lancaster, "Microstrip filters for RF/microwave applications," *New York: John Wiley & Sons,* 2001.

[3] I. C. Hunter, "Theory and design of microwave filters," *London, Institution of Electrical Engineers,* 2001.

[4] R. J. Cameron, C. M. Kudsia, and R. R. Mansour, "Microwave filters for communication systems: fundamentals, design ,and applications," *Hovoken, New Jersey: John Wiley & Sons,* 2007.

[5] D. M. Pozar, "Microwave engineering," *Reading, MA: Addison-Wesley,* 1990.

[6] D. Deslandes, and K. Wu, "Integrated microstrip and rectangular waveguide in planar form," *IEEE Microw. Wireless. Compon. Lett.,* vol. 11, pp. 68-70, Feb. 2001.

[7] J. Hirokawa, and M. Ando, "Single-layer feed waveguide consisting of posts for plane TEM wave excitation in parallel plates," *IEEE Trans. Antennas Propag.,* vol. 46, pp. 625-630, May 1998.

[8] H. Uchimura, T. Takenoshita, and M. Fujii, "Development of a "laminated waveguide"," *IEEE Trans. Microw. Theory Tech.,* vol. 46, pp. 2438-2443, Dec. 1998.

[9] L. Yan, W. Hong, G. Hua, J. X. Chen, K. Wu, and T. J. Cui, "Simulation and experiment on SIW slot array antennas," *IEEE Microw. Wireless. Compon. Lett.,* vol. 14, pp. 446-448, Sep. 2004.

[10] Y. D. Dong, W. Hong, Z. Q. Kuai, C. Yu, Y. Zhang, J. Y. Zhou, and J.-X. Chen, "Development of ultrawideband antenna with multiple band-notched characteristics using half mode substrate integrated waveguide cavity technology," *IEEE Trans Antennas Propag.,* vol. 56, pp. 2894-2902, Sep. 2008.

[11] G. Q. Luo, Z. F. Hu, L. X. Dong, and L. L. Sun, "Planar slot antenna backed by substrate integrated waveguide cavity," *IEEE Antennas Wirel. Propag. Lett.,* vol. 7, pp. 236-239, 2008.

[12] Z.-Y. Zhang, and K. Wu, "Broadband half-mode substrate integrated waveguide (HMSIW) wilkinson power divider," *Proc. IEEE MTT-S Int. Microwave Symp.,* pp. 1141-1144, Jun. 2008.

[13] K. Song, Y. Fan, and Y. Zhang, "Eight-way substrate integrated waveguide power divider with low insertion loss," *IEEE Trans. Microw. Theory Tech.,* vol. 56, pp. 1473-1477, Jun 2008.

[14] K. Song, Y. Fan, and Y. Zhang, "Radial cavity power divider based on substrate integrated waveguide technology," *Electron. Lett.,* vol. 42, pp. 1100-1101, Sep. 2006.

[15] G. H. Zhai, W. Hong, K. Wu, J. X. Chen, P. Chen, J. Wei, and H. J. Tang, "Folded half mode substrate integrated waveguide 3 dB coupler," *IEEE Microw. Wireless. Compon. Lett.,* vol. 18, pp. 512-514, Aug. 2008.

[16] B. Liu, W. Hong, Y.-Q. Wang, Q.-H. Lai, and K. Wu, "Half mode substrate integrated waveguide (HMSIW) 3-dB coupler," *IEEE Microw. Wireless. Compon. Lett.,* vol. 17, pp. 22-24, Jan. 2007.

[17] Z. C. Hao, W. Hong, X. P. Chen, J. X. Chen, K. Wu, and T. J. Cui, "Multilayered substrate integrated waveguid (MSIW) elliptic filter," *IEEE Microw. Wireless. Compon. Lett.,* vol. 15, pp. 95-97, Feb. 2005.

[18] H. J. Tang, W. Hong, J.-X. Chen, G. Q. Luo, and K. Wu, "Development of millimeter-wave planar diplexers based on complementary characters of dual-mode substrate integrated waveguide filters with circular and elliptic cavities," *IEEE Trans. Microw. Theory Tech.,* vol. 55, pp. 776-782, Apr. 2007.

[19] N. Grigoropoulos, B. Sanz-Izquierdo, and P. R. Young, "Substrate integrated folded waveguides (SIFW) and filters," *IEEE Microw. Wireless. Compon. Lett.,* vol. 15, no. 12, pp. 829-831, Dec. 2005.

[20] X. Chen, W. Hong, T. Cui, and K. Wu, "Substrate integrated waveguide (SIW) asymmetric dual-mode filter and diplexer," *Int. J. Electron.,* vol. 92, pp. 743-753, Dec. 2005.

[21] X. P. Chen, K. Wu, and Z. L. Li, "Dual-band and triple-band substrate integrated waveguide filters with Chebyshev and quasi-elliptic responses," *IEEE Trans. Microw. Theory Tech.,* vol. 55, pp. 2569-2578, Dec. 2007.

[22] Y. Cheng, W. Hong, and K. Wu, "Half mode substrate integrated waveguide (HMSIW) directional filter," *IEEE Microw. Wireless. Compon. Lett.,* vol. 17, pp. 504-506, Jul. 2007.

[23] S. T. Choi, K. S. Yang, K. Tokuda, and Y. H. Kim, "A V-band planar narrow bandpass filter using a new type integrated waveguide transition," *IEEE Microw. Wireless. Compon. Lett.,* vol. 14, pp. 545-547, Dec. 2004.

[24] H. J. Tang, W. Hong, Z. C. Hao, J. X. Chen, and K. Wu, "Optimal design of compact millimetre-wave SIW circular cavity filters," *Electron. Lett.,* vol. 41, pp. 1068-1069, Sep. 2005.

[25] X. P. Chen, and K. Wu, "Substrate integrated waveguide cross-coupled filter with negative coupling structure," *IEEE Trans. Microw. Theory Tech.,* vol. 56, pp. 142-149, Jan. 2008.

[26] Z. C. Hao, W. Hong, J. X. Chen, X. P. Chen, and K. Wu, "Compact super-wide bandpass substrate integrated waveguide (SIW) filters," *IEEE Trans. Microw. Theory Tech.,* vol. 53, pp. 2968-2977, Sep. 2005.

[27] M. Bozzi, L. Perregrini, K. Wu, and P. Arcioni, "Current and future research trends in substrate integrated waveguide technology," *Radioengineering,* vol. 18, pp. 201-209, Jun. 2009.

[28] W. Che, C. Li, P. Russer, and Y. L. Chow, "Propagation and band broadening effect of planar integrated ridged waveguide in multilayer dielectric substrates," *IEEE MTT-S Int. Microw. Symp. Dig.,* pp. 217-220, 2008.

[29] M. Bozzi, S. A. Winkler, and K. Wu, "Novel compact and broadband interconnects based on ridge substrate integrated waveguide," *IEEE MTT-S Int. Microw. Symp. Dig.,* pp. 121-124, 2009.

[30] W. Hong, Y. Wang, Q. H. Lai, and B. Liu, "Half mode substrate integrated waveguide: a new guided wave structure for microwave and millimeter wave application," *Proc. Joint 31st Int. Conf. Infrared Millimeter Waves 14th Int. Conf. Terahertz Electronics,* pp. 18-22, Sep. 2006.

[31] Y. D. Dong, T. Yang, and T. Itoh, "Substrate integrated waveguide loaded by complementary split-ring resonators and its applications to miniaturized waveguide filters," *IEEE Trans. Microw. Theory Tech.,* vol. 57, no. 9, pp. 2211-2223, Sep. 2009.

[32] Y. Dong, C. T. M. Wu, and T. Itoh, "Miniaturised multi-band substrate integrated waveguide filters using complementary split-ring resonators," *IET Microw. Antennas Propag.,* vol. 6, pp. 611-620, Apr. 2012.

[33] S. Hopfer, "The design of ridged waveguides," *IRE Trans. Microw. Theory Tech.,* vol. 3, pp. 20-29, 1955.

[34] Y. Rong, K. A. Zaki, M. Hageman, D. Stevens, and J. Gipprich, "Low-temperature cofired ceramic (LTCC) ridge waveguide bandpass chip filters," *IEEE Trans. Microw. Theory Tech.,* vol. 47, pp. 2317-2324, Dec. 1999.

[35] J. A. Ruiz-Cruz, Y. C. Zhang, K. A. Zaki, A. J. Piloto, and J. Tallo, "Ultra-wideband LTCC ridge waveguide filters," *IEEE Microw. Wireless. Compon. Lett.,* vol. 17, pp. 115-117, Feb. 2007.

[36] F. Yang, R. Liu, and Y. H, "Canonical ridged SIW fiters in LTCC," *IEEE Int. Conference on ICMTCE,* pp. 190 -192, 2011.

[37] Y. Q. Wang, W. Hong, Y. D. Dong, B. Liu, H. J. Tang, J. X. Chen, X. X. Yin, and K. Wu, "Half mode substrate integrated waveguide (HMSIW) bandpass filter," *IEEE Microw. Wireless. Compon. Lett.,* vol. 17, pp. 265-267, Apr. 2007.

[38] X. Zhang, J. Xu, Z. Yu, and Y. Dong, "C-band half mode substrate integrated waveguide (HMSIW) filter," *Microw. Opt. Technol. Lett.,* vol. 50, no, 2, pp. 275-277, Feb. 2008.

[39] J. B. Pendry, A. J. Holden, D. J. Robbins, and W. J. Stewart, "Magnetism from conductors and enhanced nonlinear phenomena," *IEEE Trans. Microw. Theory Tech. ,* vol. 47, no. 11, pp. 2075-2084, Nov. 1999.

[40] D. Schurig, J. J. Mock, and D. R. Smith, "Elctric-field-coupled resonators for negative permittivity metamaterials," *Appl. Phys. Lett.,* vol. 88, 2006.

[41] F. Falcone, T. Lopetegi, J. D.Baena, R. Marqués, F. Martín, and M. Sorolla, "Effective negative-ε stopband microstrip lines based on complementary split ring resonators," *IEEE Microw. Wireless Compon. Lett.,* vol. 14, no. 6, pp. 280-282, Jun. 2004.

[42] H.-X. Xu, G.-M. Wang, and Q. Peng, "Fractal-shaped complementary electric-LC resonator for bandstop filter," *Progr. Electromagn. Res.,* vol. 23, pp. 205-217, Aug. 2011.

[43] S. Hrabar, J. Bartolic, and Z. Sipus, "Waveguide miniaturization using uniaxial negative permeability metamaterial," *IEEE Trans. Antennas Propag.,* vol. 53, no. 1, pp. 110-119, Jan. 2005.

[44] J. Esteban, C. C. Penalosa, J. E. Page, T. M. Martin-Guerrero, and E. Marquez-Segura, "Simulation of negative permittivity and negative permeability by means of evanescent waveguide modes-theory and experiment," *IEEE Trans. Microw. Theory and Tech.,* vol. 53, no. 4, pp. 1506-1514, Apr. 2005.

[45] R. Marques, J. Martel, F. Mesa, and F. Medina, "Left-handed-media simulation and transmission of EM waves in subwavelength split ring resonator-loaded metallic waveguides," *Phys. Rev. Lett.,* vol. 19, no. 18, pp. 183 901-183 904, Oct. 2002.

[46] Q. L. Zhang, W. Y. Yin, S. He, and L. S. Wu, "Evanescent-mode substrate integrated waveguide (SIW) filters implemented with complementary split ring resonators," *Prog. Electromagn. Res.,* vol. 111, pp. 419-432, 2011.

[47] K. Deng, Z. X. Guo, C. Li, and W. Q. Che, "A compact planar bandpass filter with wide out-of-band rejection implemented by substrate-integrated waveguide and complementary split-ring resonator," *Microw. Opt. Technol. Lett.,* vol. 53, pp. 1483-1487, Jul. 2011.

[48] X. Zhang, Z. Yu, and J. Xu, "Novel band-pass substrate integrated waveguide filter based on complementary split ring resonators," *Progr. Electromagn. Res.,* vol. 72, pp. 39-46, 2007.

[49] R. Marqués, F. Mesa, J. Martel, and F. Medina, "Comparative analysis of edge-and broadside-coupled split ring resonators for

metamaterial design—theory and experiments," *IEEE Trans. Antennas Propag.,* vol. 51, no.10, pp. 2572-2581, Oct. 2003.

[50] R. Marque´s, F. Medina, and R. Rafii-El-Idrissi, "Role of bianisotropy in negative permeability and left-handed metamaterials," *Phys. Rev. B,* vol. 65, 144440, Apr. 2002.

[51] H.-X. Xu, G.-M. Wang, C.-X. Zhang, and Q. Peng, "Hilbert-shaped complementary single split ring resonator and low-pass filter with ultra-wide stopband, excellent selectivity and low insertion-loss,," *AEU-Int. J. Electron. C,* vol. 65, pp. 901-905, 2011.

[52] W. Che, C. Li, K. Deng, and L. Yang, "A novel bandpass filter based on complementary split rings resonators and substrate integrated waveguide," *Microw. Opt. Technol. Lett.,* vol. 50, no. 3, pp. 699-701, Nov. 2008.

[53] V. E. Boria, and B. Gimeno, "Waveguide filters for satellites," *IEEE Microw. Mag.,* vol. 8, pp. 60-70, Oct. 2007.

[54] G. Lastoria, G. Gerini, M. Guglielmi, and F. Emma, "CAD of triple-mode cavities in rectangular waveguide," *IEEE Microw. Guided W.,* vol. 8, pp. 339-341, Oct. 1998.

[55] H. Hu, and K.-L. Wu, "A deterministic EM design technique for general waveguide dual-mode bandpass filters," *IEEE Trans. Microw. Theory Tech.,* vol. 61, pp. 800-807, Feb. 2013.

[56] M. Guglielmi, P. Jarry, E. Kerherve, O. Roquebrun, and D. Schmitt, "A new family of all-inductive dual-mode filters," *IEEE Trans. Microw. Theory Tech.,* vol. 49, pp. 1764-1769, Oct. 2001.

[57] K. L. Wu, "An optimal circular-waveguide dual-mode filter without tuning screws," *IEEE Trans. Microw. Theory Tech.,* vol. 47, pp. 271-276, Mar. 1999.

[58] W. Steyn, and P. Meyer, "Shorted waveguide-stub coupling mechanism for narrow-band multimode coupled resonator filters," *IEEE Trans. Microw. Theory Tech.,* vol. 52, pp. 1622-1625, Jun. 2004.

[59] R. Zhang, and R. R. Mansour, "Dual-band dielectric-resonator filters," *IEEE Trans. Microw. Theory Tech.,* vol. 57, pp. 1760-1766, Jul. 2009.

[60] A. Panariello, M. Yu, and C. Ernst, "Ku-band high power dielectric resonator filters," *IEEE Trans. Microw. Theory Tech.,* vol. 61, pp. 382-392, Jan. 2013.

[61] R. Zhang, and R. R. Mansour, "Low-cost dielectlic resonator filters with improved spurious performance," *IEEE Trans. Microw. Theory Tech.,* vol. 55, pp. 2168-2175, Oct. 2007.

[62] L. K. Hady, D. Kajfez, and A. A. Kishk, "Triple mode use of a single dielectric resonator," *IEEE Trans Antennas Propag.,* vol. 57, pp. 1328-1335, May 2009.

[63] I. B. Vendik, V. V. Kondratiev, D. V. Kholodniak, S. A. Gal'chenko, A. N. Deleniv, M. N. Goubina, A. A. Svishchev, S. Leppavuori, J. Hagberg, and E. Jakku, "High-temperature superconductor filters: modeling and experimental investigations," *IEEE Trans. Appl. Supercon.,* vol. 9, pp. 3577-3580, Jun. 1999.

[64] M. F. Sitnikova, I. B. Vendik, O. G. Vendik, D. V. Kholodnyak, P. A. Tural'chuk, I. V. Kolmakova, P. Y. Belyavskii, and A. A. Semenov, "Modeling and experimental investigation of microstrip resonators and filters based on High-Temperature Superconductor films," *Tech. Phys. Lett.,* vol. 36, pp. 862-864, Sep. 2010.

[65] E. G. Cristal, and S. Frankel, "Hairpin-line and hybird hairpin-line half-wave parallel-coupled-line filters," *IEEE Trans. Microw. Theory Tech.,* vol. 20, pp. 719-728, Nov. 1972.

[66] I. Wolff, "Microstrip bandpass filter using degenerate modes of a microstrip ring resonator," *Electron. Lett.,* vol. 8, pp. 302-303, Jun. 1972.

[67] J. S. Hong, and S. H. Li, "Theory and experiment of dual-mode microstrip triangular patch resonators and filters," *IEEE Trans. Microw. Theory Tech.,* vol. 52, pp. 1237-1243, Apr. 2004.

[68] S. B. Cohn, "Microwave bandpass filters containing high-Q dielectric resonators," *IEEE Trans. Microw. Theory Tech.,* vol. 16, pp. 218-227, 1968.

[69] A. M. Model, "Design of waveguide and coaxial bandpass filters with directly-coupled cavities," *Telecommun. Radio Eng.,* 1967.

[70] A. E. Atia, and A. E. Williams, "Narrow-bandpass waveguide filters," *IEEE Trans. Microw. Theory Tech.,* vol. 20, pp. 258-265, Apr. 1972.

[71] D. Deslandes, and K. Wu, "Single-substrate integration technique of planar circuits and waveguide filters," *IEEE Trans. Microw. Theory Tech.,* vol. 51, pp. 593-596, Feb. 2003.

[72] F. Xu, and K. Wu, "Guided-wave and leakage characteristics of substrate integrated waveguide," *IEEE Trans. Microw. Theory Tech.,* vol. 53, pp. 66-73, Jan. 2005.

[73] D. Deslandes, and K. Wu, "Accurate modeling, wave mechanisms, and design considerations of a substrate integrated waveguide," *IEEE Trans. Microw. Theory Tech.,* vol. 54, pp. 2516-2526, Jun. 2006.

[74] Y. Cassivi, L. Perregrini, P. Arcioni, M. Bressan, K. Wu, and G. Conciauro, "Dispersion characteristics of substrate integrated rectangular waveguide," *IEEE Microw. Wireless. Compon. Lett.,* vol. 12, pp. 333-335, Sep. 2002.

[75] S. Pal, C. J. Stevens, and D. J. Edwards, "Compact parallel coupled HTS microstrip bandpass filters for wireless communications," *IEEE Trans. Microw. Theory Tech.,* vol. 54, pp. 768-775, Feb. 2006.

[76] C. F. Chang, and S. J. Chung, "Bandpass filter of serial configuration with two finite transmission zeros using LTCC technology," *IEEE Trans. Microw. Theory Tech.,* vol. 53, pp. 2383-2388, Jul. 2005.

[77] L. K. Yeung, and K. L. Wu, "A compact second-order LTCC bandpass filter with two finite transmission zeros," *IEEE Trans. Microw. Theory Tech.,* vol. 51, pp. 337-341, Feb. 2003.

[78] C. W. Tang, "Harmonic-suppression LTCC filter with the step-impedance quarter-wavelength open stub," *IEEE Trans. Microw. Theory Tech.,* vol. 52, pp. 617-624, Feb. 2004.

[79] N. C. Karmakar, and M. N. Mollah, "Investigations into nonuniform photonic-bandgap microstripline low-pass filters," *IEEE Trans. Microw. Theory Tech.,* vol. 51, pp. 564-572, Feb. 2003.

[80] T. Y. Yun, and K. Chang, "Uniplanar one-dimensional photonic-bandgap structures and resonators," *IEEE Trans. Microw. Theory Tech.,* vol. 49, pp. 549-553, Mar. 2001.

[81] Y. J. Lee, J. Yeo, R. Mittra, and W. S. Park, "Application of electromagnetic bandgap (EBG) superstrates with controllable defects for a class of patch antennas as spatial angular filters," *IEEE Trans. Antennas Propag.,* vol. 53, pp. 224-235, Jan. 2005.

[82] S. W. Wong, and L. Zhu, "EBG-embedded multiple-mode resonator for UWB bandpass filter with improved upper-stopband performance," *IEEE Microw. Wireless. Compon. Lett.,* vol. 17, pp. 421-423, Jun. 2007.

[83] P. de Maagt, R. Gonzalo, Y. C. Vardaxoglou, and J. M. Baracco, "Electromagnetic bandgap antennas and components for microwave

and (sub)millimeter wave applications," *IEEE Trans Antennas Propag.,* vol. 51, pp. 2667-2677, Oct. 2003.

[84] H. J. Chen, T. H. Huang, C. S. Chang, L. S. Chen, N. F. Wang, Y. H. Wang, and M. P. Houng, "A novel cross-shape DGS applied to design ultra-wide stopband low-pass filters," *IEEE Microw. Wireless. Compon. Lett.,* vol. 16, pp. 252-254, May 2006.

[85] V. Aparin, and P. Katzin, "Active GAAS MMIC band-pass filters with automatic frequency tuning and insertion loss control," *IEEE J. Solid-St. Circ. ,* vol. 30, pp. 1068-1073, Oct. 1995.

[86] M. J. Schindler, and Y. Tajima, "A novel MMIC active-filter with lumped and transversal elements," *IEEE Trans. Microw. Theory Tech.,* vol. 37, pp. 2148-2153, Dec. 1989.

[87] K. Entesari, and G. M. Rebeiz, "A 12-18-GHz three-pole RF MEMS tunable filter," *IEEE Trans. Microw. Theory Tech.,* vol. 53, pp. 2566-2571, Aug. 2005.

[88] L. Dussopt, and G. M. Rebeiz, "Intermodulation distortion and power handling in RF MEMS switches, varactors, and tunable filters," *IEEE Trans. Microw. Theory Tech.,* vol. 51, pp. 1247-1256, Apr. 2003.

[89] A. Abbaspour-Tamijani, L. Dussopt, and G. M. Rebeiz, "Miniature and tunable filters using MEMS capacitors," *IEEE Trans. Microw. Theory Tech.,* vol. 51, pp. 1878-1885, Jul. 2003.

[90] R. Levy, "Direct synthesis of cascaded quadruplet (CQ) filters," *IEEE MTT-S Int. Microwave Symp.* vol. 1-3, pp. 497-590, 1995.

[91] R. Levy, "Direct synthesis of cascaded quadruplet (CQ) filters " *IEEE Trans. Microw. Theory Tech.,* vol. 44, pp. 1517, Aug. 1996.

[92] R. Levy, and P. Petre, "Design of CT and CQ filters using approximation and optimization," *IEEE Trans. Microw. Theory Tech.,* vol. 49, pp. 2350-2356, Dec. 2001.

[93] J.-C. Lu, C.-K. Liao, and C.-Y. Chang, "Microstrip parallel-coupled filters with cascade trisection and quadruplet responses," *IEEE Trans. Microw. Theory Tech.,* vol. 56, pp. 2101-2110, Sep. 2008.

[94] J. S. Hong, and M. J. Lancaster, "Cross-coupled microstrip hairpin-resonator filters," *IEEE Trans. Microw. Theory Tech.,* vol. 46, pp. 118-122, Jan. 1998.

[95] S. Amari, "Synthesis of cross-coupled resonator filters using an analytical gradient-based optimization technique," *IEEE Trans. Microw. Theory Tech.,* vol. 48, pp. 1559-1564, Sep. 2000.

[96] R. J. Cameron, "Advanced coupling matrix synthesis techniques for microwave filters," *IEEE Trans. Microw. Theory Tech.,* vol. 51, pp. 1-10, Jan. 2003.

[97] J. S. Hong, and M. J. Lancaster, "Couplings of microstrip square open-loop resonators for cross-coupled planar microwave filters," *IEEE Trans. Microw. Theory Tech.,* vol. 44, pp. 2099-2109, Nov. 1996.

[98] M. Bozzi, M. Pasian, L. Perregrini, and K. Wu, "On the losses in substrate integrated waveguides," *Proc. Eur. Microw. Conf.,* Oct. 2007.

[99] M. Bozzi, L. Perregrini, and K. Wu, "Modeling of conductor, dielectric, and radiation losses in substrate integrated waveguide by the boundary integral-resonant mode expansion method," *IEEE Trans. Microw. Theory Tech.,* vol. 56, pp. 3153-3161, Dec. 2008.

[100] D. Deslandes, and K. Wu, "Design consideration and performance analysis of substrate integrated waveguide components," *Proc. Eur. Microw. Conf.,* pp. 881-884, Sep. 2002.

[101] Y. Lou, C. H. Chan, and Q. Xue, "An in-line waveguide-to-microstrip transition using radial-shaped probe," *IEEE Microw. Wireless. Compon. Lett.,* vol. 18, no. 5, pp. 311-313, May 2008.

[102] W. Grabherr, B. Huder, and W. Menzel, "Microstrip to waveguide transition compatible with mm-wave integrated circuits," *IEEE Trans. Microw. Theory Tech.,* vol. 42, pp. 1842-1843, Sep. 1994.

[103] F. J. Villegas, D. I. Stones, and H. A. Hung, "A novel waveguide-to-microstrip transition for millimeter-wave module applications," *IEEE Trans. Microw. Theory Tech.,* vol. 47, no. 1, pp. 48-55, Jan. 1999.

[104] N. Kaneda, Y. Qian, and T. Itoh, "A broadband microstrip-to-waveguide transition using quasi-Yagi antenna " *IEEE MTT-S Int. Microwave Symp.,* vol. 4, pp. 1431 - 1434, 1999.

[105] T. Y. Huang, T. M. Shen, and R. B. Wu, "Design and modeling of microstrip line to substrate integrated waveguide transitions," *Passive Microwave Components and Antennas,* pp. 225-246.

[106] K. Wu, D. Deslandes, and Y. cassivi, "The substrate integrated circuits - a new concept for high-frequency electronics and optoelectronics," *Microw. Rev.,* pp. 2-9, Dec. 2003.

[107] D. Deslandes, and K. Wu, "Integrated transition of coplanar to rectangular waveguides," *IEEE MTT-S Intl. Microw. Symp. Dig.,* vol. 2, pp. 619-622, May 2001.

[108] S. Lee, S. Jung, and H. Y. Lee, "Ultra-wideband CPW-to-substrate integrated waveguide transition using an elevated-CPW section," *IEEE Microw. Wireless. Compon. Lett.,* vol. 18, pp. 746-748, Nov. 2008.

[109] S. B. Cohn, "Properties of ridge wave guide," *Proc. IRE,* pp. 783-788, 1947.

[110] R. E. Collin, "Foundations for microwave engineering," *Wiley-IEEE Press,* Dec. 2000.

[111] C. Li, W. Che, P. Russer, and Y. L. Chow, "Progagation and band broadening effect of planar ridged substrate-integrated waveguide (RSIW)," *IEEE Int. Conference on ICMMT,* vol. 2, pp. 467-470, 2008.

[112] W. Che, C. Li, D. Zhang, and Y. L. Chow, "Investigations on propagation and the band broadening effect of ridged rectangular waveguide integrated in a multilayer dielectric substrate," *IET Microw. Antennas Propag.,* vol. 4, pp. 674-684, Jun. 2010.

[113] S. A. W. M.Bozzi, K .Wu, "Broadband and compact ridge substrateintegrated waveguides," *IET Microw.Antennas Propag.,* vol. 14, pp. 1965-1973, 2010.

[114] Q. H. Lai, C. Fumeaux, W. Hong, and R. Vahldieck, "Characterization of the propagation properties of the half-mode substrate integrated waveguide," *IEEE Trans. Microw. Theory Tech.,* vol. 57, pp. 1996-2004, Aug. 2009.

[115] J. D. Baena, J. Bonache, F. Martin, R. Marques, F. Falcone, T. Lopetegi, M. A. G. Laso, J. Garcia, I. Gil, and M. Sorolla, "Equivalent-circuit models for split-ring resonators and complementary split-ring resonators coupled to planar transmission lines," *IEEE Trans. Microw. Theory Tech. ,* vol. 53, no. 4, pp. 1451-1461, Apr. 2005.

[116] G. Lubkowski, C. Damm, B. Bandlow, R. Schuhmann, M. Schubler, and T. Weiland, "Broadband transmission below the cutoff frequency of a waveguide loaded with resonant scatterer arrays," *IET Microw. Antennas Propag.,* vol. 1, no. 1, pp. 165-169, 2007.

[117] P. Belov, and C. Simovski, "Subwavelength metallic waveguides loaded by uniaxial resonant scatterers," *Phys. Rev. E, Stat. Phys. Plasmas Fluids Relat. Interdiscip. Top.,* vol. 72, pp. 0366181-03661811, Sep. 2005.

[118] H.-T. Chen, J. F. O'Hara, A. J. Taylor, and R. D. Averitt, "Complementary planar terahertz metamaterials," *Opt. Express* vol. 15, pp. 1084-1095, Feb. 2007.

[119] Y. Cassivi, L. Perregrini, P. Arcioni, M. Bressan, K. Wu, and G. Conciauro, "Dispersion characteristics of substrate integrated rectangular waveguide," *IEEE Microw. Wireless Compon. Lett.,* vol. 12, pp. 333-335, Sep. 2002.

[120] W. Che, D. Wang, K. Deng, and Y. L. Chow, "Leakage and ohmic losses investigation in substrate-integrated waveguide," *Radio Sci.,* vol. 42, Oct. 2007.

[121] M. A. E. Sabbagh, and R. R. Mansour, "Integration of ridge waveguide filter in printed circuit board " *IEEE Radio and Wireless Symposium,* pp. 460 - 463 2010

[122] J. R. Pyle, "The cutoff wavelength of the TE10 mode in ridged rectangular waveguide of any aspect ratio " *IEEE Trans. Microw. Theory Tech.,* vol. 14, pp. 175-183, 1966.

[123] D. Deslandes, and K. Wu, "Accurate modeling, wave mechanisms, and design considerations of a substrate integrated waveguide," *IEEE Trans. Microw. Theory Tech.,* vol. 54, pp. 2516-2526, Jun. 2006.

[124] J. Bonache, M. Gil, I. Gil, J. Garcia-Garcia, and F. Martin, "On the electrical characteristics of complementary metamaterial resonators," *IEEE Microw. Wireless. Compon. Lett.,* vol. 16, pp. 543-545, Oct. 2006.

[125] J. Esteban, C. Camacho-Peñalosa, J. E. Page, T. M. Martín-Guerrero, and E. Márquez-Segura, "Simulation of negative permittivity and negative permeability by means of evanescent waveguide modes—theory and experiment," *IEEE Trans. Microw. Theory Tech.,* vol. 53, no. 4, pp. 1506-1514, Apr. 2005.

[126] V. Radonić, V. Crnojević-Bengin, and B. Jokanović, "On the orientation of split-ring resonators in metamaterial media," *8th International Conference on Telecommunications in Modern Satellite, Cable and Broadcasting Services,* pp. 645-648, 2007

[127] F. Hesmer, "Coupling mechanisms for split ring resonators: theory and experiment," *Phy. Stat. Sol. (b),* vol. 224, no. 4, pp. 1170-1175, Mar. 2007.

[128] G. F. Craven, and C. K. Mok, "The design of evanescent mode waveguide bandpass filters for a prescribed insertion loss characteristic," *IEEE Trans. Microw. Theory Tech. ,* vol. 19, pp. 295-308, 1971.

[129] A. Shelkovnikov, and D. Budimir, "Left-handed rectangular waveguide bandstop filters," *Microw. Opt. Technol. Lett.,* vol. 48, no. 5, pp. 846-848, May 2006.

[130] T. H. Hand, J. Gollub, S. Sajuyigbe, D. R. Smith, and S. A. Cummer, "Characterization of complementary electric field coupled resonant srufaces," *Appl. Phys. Lett.,* vol. 93, Nov. 2008.

[131] D. Robben, S. F. Peik, T. Henning, M. Becker, "Laser machined microsystems for active frequency selective surfaces," *IEEE MTT-S Intl. Microw. Symp. Dig.,* pp. 1-3, Jun. 2012.